



Codes And Methods Improvements
for VVER comprehensive safety assessment

Grant Agreement Number: 945081

Start date: 01/09/2020 - Duration: 36 Months

WP6 - Task 6.3

D6.3 – Uncertainties propagation on Kozloduy-6 CFD simulation through Deterministic Sampling method

V. Sanchez, M. Böttcher (KIT)
V. Khayiguian, A. Mas, O. Bernard (FRA),
R. Nop (CEA),
D. Ruban, A. Hashymov, O. Sevbo (ER),
N. Forgione, O. Halim, A. Pucciarelli (UNIFI)

Version 1 – 28/09/2023

CAMIVVER – Grant Agreement Number: 945081



This project has received funding from the Euratom research and training programme 2019-2020 under grant agreement No 945081.

Document title	Uncertainties propagation on Kozloduy-6 CFD simulation through Deterministic Sampling method
Author(s)	Viken KHAYIGUIAN
Document type	Deliverable
Work Package	WP6
Document number	D6.3
Issued by	FRAMATOME
Date of completion	28/09/2023
Dissemination level	Public

Summary

This deliverable describes the analysis of the uncertainty propagation performed with deterministic sampling through the computation of the Coolant Mixing Test at the Kozloduy Unit 6 Nuclear Power plant. The computations were performed using different CFD-models built by different partners with different softwares which are described in deliverables D6.1 and D6.2.

In the first part, the objectives and context are introduced. In the second part, deterministic sampling (DS) used to propagate uncertainty and the Proper Orthogonal Decomposition (POD) are introduced. In the third part the quantities of interest described in this document and the data processing are described. Then in the fourth part, the results of the uncertainty quantification are detailed.

The objective of this study is to perform an uncertainty propagation to verify the consistency and sensitivity of CFD results to the software, model and propagation method chosen. This has been done by testing different turbulence models, with different softwares and by using different deterministic ensembles for propagating uncertainties. For this, four input parameters were set as uncertain and their statistical moments were propagated through CFD computations with different DS ensembles. In conclusion of this study, the assessment of the sensitivity and uncertainty statistical moments with DS and POD enabled to illustrate the effect of inputs on computations of the mixing coefficients and temperature in the core.

Deterministic sampling was found to yield consistent results between partners and ensembles with amplitudes that were found to stay moderate. The importance of evaluating simultaneous variations of parameters and the effect of evaluating the CFD responses on ensembles with increasing complexity was highlighted, thus, ensembles that should be preferred to evaluate the CFD response statistical moments were put forward. In terms of model sensitivity, two kinds of behaviour were observed: models which tend to smoothen the time fluctuations of signals, and models which do not which presented higher variance. On these latter ones, the combined effect of meshing, numerical scheme and turbulence modelling should be investigated further to increase our understanding of their impact on the unsteadiness of the resulting simulations.

In conclusion, the important result of this study is the consistency of the results between the partners regarding the quantities of interest and their uncertainty which are very close one model from another, increasing the confidence in the modelling of a VVER vessel for mixing simulations with CFD codes.

Approval




Version	First Author	WP leader	Project Coordinator
1	Viken KHAYIGUIAN	Olivier BERNARD	Denis VERRIER
			

Table of contents

Summary	2
1. Introduction	9
2. Numerical methods for uncertainty quantification	10
2.1. Covariance propagation using deterministic sampling	10
2.2. Proper Orthogonal decomposition	13
3. Data processing	14
3.1. Quantities of interest	14
3.2. Filtering of the signal	15
3.3. Determination of quantiles	17
3.4. Sensitivity analysis	18
3.5. List of performed computations	19
4. Results	20
4.1. Mixing coefficients	20
4.2. Hot leg 1 temperature <i>THL, 1</i>	28
4.3. FA Temperature average	41
5. Conclusion	61
6. References	62
A. Building ensemble	65
B. CEA results	69
a. Mixing coefficient	69
b. FA temperature average	70
c. Hot leg 1 temperature <i>THL, 1</i>	72

List of Figures

FIGURE 1 : EXAMPLES OF POSTPROCESSED FIELDS FROM A CFD SIMULATION	14
FIGURE 2 : EXAMPLES OF EVOLUTION OF $THL, 1$ ON THE LAST 200S OF THE TRANSIENT SIMULATION WITH TWO MODELS. THE RED LINE CORRESPONDS TO THE REFERENCE CALCULATION WHILE BLUE AND BLACK CURVES CORRESPOND TO SIMULATION EVALUATED WITH DIFFERENT DS ENSEMBLES.	15
FIGURE 3 : ILLUSTRATION OF THE QUANTITY OF INTEREST DURING THE FILTERING PROCESS. A) SUPERPOSITION OF THE RAW SIGNALS AND B) SUPERPOSITION OF THE FILTERED SIGNAL WITH $r = 1$. ON C) THE RED PART CORRESPONDS TO A RECONSTRUCTION OF THE FLUCTUATIONS WITH 1 MODE. THE ASSOCIATED TRUNCATION ERROR IS GIVEN ON D): MEAN VALUE OVER TIME IN RED, BLACK LINES CORRESPONDS TO AN INTERVAL $\mu \pm 1.65\sigma$ WHILE THE GREY LINES CORRESPOND TO REALIZATIONS OF THE TRUNCATION ERROR ON THE DIFFERENT SNAPSHOTS. .	16
FIGURE 4: ILLUSTRATION OF DIFFERENT CORRELATION DEGREES BETWEEN PARAMETER Y AND INPUTS $X1, X2, X3$ AND $X4$	18
FIGURE 5: ILLUSTRATION OF THE POD APPLIED TO TFA, oi WITH A TRUNCATION OF ORDER $r = 2$	19
FIGURE 6 : MEAN VALUE OF THE MIXING COEFFICIENT $c1$ EVALUATED FOR DIFFERENT CFD MODELS AND DS ENSEMBLES.....	21
FIGURE 7 : STANDARD DEVIATION OF THE MIXING COEFFICIENT $c1$ EVALUATED FOR DIFFERENT CFD MODELS AND DS ENSEMBLES.....	22
FIGURE 8 : MODE 1 OF THE POD APPLIED TO THE SNAPSHOTS OF $c1i$ OBTAINED ON DIFFERENT ENSEMBLES WITH DIFFERENT CFD MODELS AND MODE 2 FOR UNIPI ΣGHM SNAPSHOTS.....	24
FIGURE 9 : EVOLUTION OF $a1$ WITH THE INPUT PARAMETERS FOR POD PERFORMED ON THE RESULTS OF THE DIFFERENT CFD MODELS/DS ENSEMBLES	25
FIGURE 10 : QUANTILES 2.5%, 50% AND 97.5% ON THE MIXING COEFFICIENT $c1i$ FOR DIFFERENT ENSEMBLES AND MODELS. FA ARE WHITE WHEN THE FITTED METALOG DISTRIBUTION WAS INFEASIBLE.....	26
FIGURE 11 : 2.5% (LEFT) AND 97.5% (RIGHT) QUANTILES CALCULATED WITH A METALOG DISTRIBUTION WITH ENERGORISK CFD MODEL ON ΣKRT . FA ARE WHITE WHEN THE FITTED METALOG DISTRIBUTION WAS INFEASIBLE.	27
FIGURE 12: TIME EVOLUTION OF $THL, 1$ OBTAINED FROM THE DIFFERENT ENSEMBLES AND PARTNERS. EVALUATION OF CFD FOR THE MEAN SET OF INPUTS (BLACK) AND FOR INDIVIDUAL (RED) AND COMBINED (BLUE) VARIATIONS OF INPUTS.	28
FIGURE 13: COMPARISON OF THE TIME EVOLUTION OF INCREASE OF HOT LEG 1 TEMPERATURE. ALL COMPUTATIONS (A) AND MEAN VALUES (B).....	29
FIGURE 14: EVOLUTION OF THE RATIO BETWEEN TIME FLUCTUATIONS AND SIGNAL VARIABILITY R WITH THE TRUNCATION ORDER OF THE FILTERING r	30
FIGURE 15: QUANTILE FUNCTIONS ASSOCIATED TO THE FITTED METALOG DISTRIBUTION FOR THE DIFFERENT ENSEMBLES AND PARTNERS.....	32
FIGURE 16 : NON NORMALIZED PDF ASSOCIATED TO THE FITTED METALOG DISTRIBUTION FOR THE DIFFERENT ENSEMBLES AND PARTNERS	33
FIGURE 17 : TIME EVOLUTION OF $THL, 1$ – MEAN VALUE (DOTTED BLACK), MEDIAN VALUE (SOLID WHITE), $Q5\%$, $Q95\%$ (FILLED RED), $Q2.5\%$, $Q97.5\%$ (FILLED SALMON) AND EXPERIMENTAL VALUE (SOLID BLUE).....	34

FIGURE 18: TIME EVOLUTION OF $THL, 1$ – MEAN VALUE (DOTTED BLACK), MEDIAN VALUE (SOLID WHITE), $Q5\%$, $Q95\%$ (FILLED RED), $Q2.5\%$, $Q97.5\%$ (FILLED SALMON) AND EXPERIMENTAL VALUE (SOLID BLUE)..... 35

FIGURE 19: INTERSECTION AND UNION OF THE INTERVAL $Q2.5\%$, $Q97.5\%$ OVER THE EVALUATIONS. UNION OF THE INTERVALS BETWEEN PARTNERS/ENSEMBLES (RED), INTERSECTION OF INTERVALS (BLACK), EXPERIMENTAL VALUES (BLUE) 36

FIGURE 20: SCATTER PLOT FOR $Y = \Delta THL, 1$ AS A FUNCTION OF $X1$ 37

FIGURE 21 : EVOLUTION OF $\Delta THL, 1$ ON SCATTER PLOTS X_i, X_j – ENERGORISK – AMPLITUDE OF Y IS GIVEN WITH A JET COLORMAP 37

FIGURE 22 : EVOLUTION OF $\Delta THL, 1$ ON SCATTER PLOTS X_i, X_j – FRAMATOME – AMPLITUDE OF Y IS GIVEN WITH A JET COLORMAP 38

FIGURE 23: EVOLUTION OF $\Delta THL, 1$ ON SCATTER PLOTS X_i, X_j – KIT – AMPLITUDE OF Y IS GIVEN WITH A JET COLORMAP 38

FIGURE 24 : EVOLUTION OF $\Delta THL, 1$ ON SCATTER PLOTS X_i, X_j – UNIPI – AMPLITUDE OF Y IS GIVEN WITH A JET COLORMAP 39

FIGURE 25: MEAN VALUE (POINT) AND STANDARD DEVIATION (ERROR BARS) EVALUATED FOR THE DIFFERENT PARTNERS AND ENSEMBLE 40

FIGURE 26 : TEMPERATURE TFA, oi (K) AT $t = t_0 + 800s$ – EXAMPLES FOR THE DIFFERENT PARTNERS 41

FIGURE 27 : MEAN VALUE OF TFA, oi (K) AT $t = t_0 + 800s$ – RESULTS FOR THE DIFFERENT PARTNERS/ENSEMBLES 42

FIGURE 28 : STANDARD DEVIATION OF TFA, oi (K) AT $t = t_0 + 800s$ – RESULTS FOR THE DIFFERENT PARTNERS/ENSEMBLES 43

FIGURE 29 : EXAMPLE OF 2D VARIATION FIELD $TFA, oi, X - TFA, oi, \mu X$ FOR DIFFERENT VARIATIONS OF INPUTS X 44

FIGURE 30 : RIC AS A FUNCTION OF THE NUMBER OF MODES FOR THE POD APPLIED TO THE SNAPSHOTS OF THE DIFFERENT ENSEMBLES EVALUATED BY ENERGORISK. ... 45

FIGURE 31 : 4 FIRST MODES CALCULATED FROM THE SNAPSHOTS OF ENSEMBLE ΣSTD 45

FIGURE 32 : 4 FIRST MODES CALCULATED FROM THE SNAPSHOTS OF ENSEMBLE ΣKRT 46

FIGURE 33 : ZOOM ON MODE 2 FROM THE TWO ENSEMBLES EVALUATED WITH ENERGORISK MODEL 47

FIGURE 34 : RIC AS A FUNCTION OF THE NUMBER OF MODES FOR THE POD APPLIED TO THE SNAPSHOTS OF THE DIFFERENT ENSEMBLES. 48

FIGURE 35: 4 FIRST MODES CALCULATED FROM THE SNAPSHOTS OF ENSEMBLE ΣSTD WITH FRAMATOME MODEL. 48

FIGURE 36 : 4 FIRST MODES CALCULATED FROM THE SNAPSHOTS OF ENSEMBLE ΣGHM WITH FRAMATOME MODEL. 49

FIGURE 37 : 4 FIRST MODES CALCULATED FROM THE SNAPSHOTS OF ENSEMBLE ΣKRT WITH FRAMATOME MODEL. 49

FIGURE 38 : RIC AS A FUNCTION OF THE NUMBER OF MODES FOR THE POD APPLIED TO THE SNAPSHOTS OF THE DIFFERENT ENSEMBLES EVALUATED BY KIT. 51

FIGURE 39 : 4 FIRST MODES CALCULATED FROM THE SNAPSHOTS OF ENSEMBLE ΣHAD WITH KIT MODEL. 51

FIGURE 40 : RIC AS A FUNCTION OF THE NUMBER OF MODES FOR THE POD APPLIED TO THE SNAPSHOTS OF THE DIFFERENT ENSEMBLES EVALUATED BY UNIPI. 52

FIGURE 41 : 4 FIRST MODES CALCULATED FROM THE SNAPSHOTS OF ENSEMBLE ΣHAD WITH UNIPI MODEL. 53

FIGURE 42: 4 FIRST MODES CALCULATED FROM THE SNAPSHOTS OF ENSEMBLE ΣGHM WITH UNIPI MODEL. 53

FIGURE 43 : RIC AS A FUNCTION OF THE NUMBER OF MODES 55

FIGURE 44: 6 FIRST MODES CALCULATED FROM ALL THE SNAPSHOTS EVALUATED WITH FRAMATOME, KIT AND UNIPI MODELS. 55

FIGURE 45: QUANTILES OF TFA, oi EVALUATED WITH FRAMATOME MODEL ON ΣKRT ENSEMBLE. 58

FIGURE 46 : MEDIAN TEMPERATURE TFA, oi EVALUATED WITH FRAMATOME MODEL ON ΣKRT ENSEMBLE (SOLID BLACK LINE). THE INTERVAL BETWEEN THE 5% QUANTILE AND 95% QUANTILE IS FILLED IN RED, AND THE 2.5% 97.5% QUANTILES IN SALMON. 58

FIGURE 47: EXAMPLES OF QUANTILES EVALUATED FOR DIFFERENT MODELS ON DIFFERENT ENSEMBLES. MEDIAN (SOLID BLACK LINE), [2.5,97.5%] INTERVAL FILLED IN SALMON AND [5,95%] INTERVAL FILLED IN RED 59

FIGURE 48 : MEAN VALUE OF THE MIXING COEFFICIENTS $C1, C2, C3$ AND $C4$ 69

FIGURE 49 : STANDARD DEVIATION OF THE MIXING COEFFICIENTS $C1, C2, C3$ AND $C4$... 70

FIGURE 50 : MEAN VALUE AND STANDARD DEVIATION OF THE FA TEMPERATURE EVALUATED WITH GHM ENSEMBLE FOR CEA COMPUTATIONS 70

FIGURE 51 : RIC AS A FUNCTION OF THE NUMBER OF MODES FOR THE POD APPLIED TO THE SNAPSHOTS OF THE DIFFERENT ENSEMBLES EVALUATED BY CEA WITH GHM ENSEMBLE. 71

FIGURE 52 : 4 FIRST MODES CALCULATED FROM THE SNAPSHOTS OF ENSEMBLE ΣGHM 71

FIGURE 53: INCREASE OF TEMPERATURE IN HOT LEG 1 $THL, 1$ FOR THE DIFFERENT INPUTS SCANNED. 72

FIGURE 54: TIME EVOLUTION OF $THL, 1$ – MEAN VALUE (DOTTED BLACK), MEDIAN VALUE (SOLID WHITE), $Q5\%$, $Q95\%$ (FILLED RED), $Q2.5\%$, $Q97.5\%$ (FILLED SALMON) 72

List of Tables

TABLE 1: LIST OF UNCERTAIN PARAMETERS FOR KOZLODUY-6 MIXING PARAMETERS	9
TABLE 2: LIST OF ENFORCED STATISTICAL MOMENT FOR A 4D GAUSSIAN RV WITH THE DIFFERENT ENSEMBLES	13
TABLE 3: LIST OF ENSEMBLES CHOSEN FOR THE DIFFERENT PARTNERS	19
TABLE 4 : RIC FOR ONE MODE AND NUMBER OF MODES <i>NPOD</i> REQUIRED FOR <i>RICNPOD</i> ≥ 0.99	23
TABLE 5: RATIO <i>R</i> CALCULATED BEFORE/AFTER FILTERING (TRUNCATION WITH <i>r</i> = 1) FOR THE DIFFERENT PARTNERS.	29
TABLE 6 :STATISTICAL MOMENTS ON THE OUTPUT $Y = \Delta THL, 1$	31
TABLE 7 :EVALUATION OF QUANTILES ON $Y = \Delta THL, 1$ WITH DIFFERENT ENSEMBLES....	32
TABLE 8 :CORRELATION OF THE INPUTS WITH THE OUTPUT $Y = \Delta THL, 1$	36
TABLE 9 :MEAN AND STANDARD DEVIATION OF <i>Uinputs</i> FOR THE CALCULATION OF $Y = \Delta THL, 1$	39
TABLE 10: FRAMATOME - CORRELATION OF THE COMPONENTS OF THE POD WITH THE INPUTS – IMPORTANCE OF THE CORRELATION GIVEN WITH SHADES OF ORANGE. .	50
TABLE 11: KIT - CORRELATION OF THE COMPONENTS OF THE POD WITH THE INPUTS – IMPORTANCE OF THE CORRELATION GIVEN WITH SHADES OF ORANGE.....	51
TABLE 12 : UNUPI - CORRELATION OF THE COMPONENTS OF THE POD WITH THE INPUTS – IMPORTANCE OF THE CORRELATION GIVEN WITH SHADES OF ORANGE.....	54
TABLE 13 : CORRELATION BETWEEN THE COMPONENTS OF THE POD AND THE INPUT PARAMETERS EVALUATED ON DIFFERENT CFD MODELS AND ENSEMBLES.....	56

Abbreviations

CFD	Computational fluid mechanics
CDF	Cumulative distribution function
DS	Deterministic sampling
FA	Fuel assembly
NPP	Nuclear power "plant
PDF	Probability density function
POD	Proper orthogonal decomposition
RIC	Relative information content
RS	Random sampling
RV	Random variable
UQ	Uncertainty quantification

1. Introduction

The purpose of deliverable D6.3 is to present the work performed by the partners involved in WP6.3 of the H2020 CAMIVVER project [1]. Previous work has been done by the different partners in tasks 6.1 and 6.2 to elaborate a CFD model of a Nuclear Power Plant (NPP) of VVER-design located in Kozloduy, Bulgaria. Steady state simulations at nominal power were performed followed by transient simulations reproducing the Kozloduy-6 Mixing Experiment. The results and conclusion of these two tasks can be found respectively in the deliverables D6.1 [2] and D6.2 [3]. The purpose of this task is to go a step further and assess the uncertainty on the CFD results. In fact, when performing CFD simulations, uncertainties on the results can arise at different steps of the case setup and have to be taken into account when compared to experimental data or when utilizing the results for safety and design. In the nuclear industry, guidelines provided by the ASME in reference [4] are used for the assessment of simulation errors and uncertainties. In this work, only one source of uncertainty is considered, namely, the uncertainty on the simulation inputs denoted U_{inputs} which is the uncertainty induced by taking into account the inputs uncertainty in the CFD computations. Thus, this task does not aim to make a comprehensive uncertainty quantification study but only to focus on the propagation of the inputs' uncertainty. The objectives of this study are at the same time the assessment of statistical moments and quantiles of U_{inputs} of different quantities of interest and providing a reliable methodology for it. A realization of the random variable (RV) U_{inputs} is denoted $\delta_{U_{inputs}}$ and can be written:

$$\delta_{U_{inputs}} = f_{CFD}(\boldsymbol{\mu}_X) - \delta_{f_{CFD}(\delta_X)}$$

Where $f_{CFD}(\boldsymbol{\mu}_X)$ is the output of CFD when considering determined inputs which are taken at their mean values $\boldsymbol{\mu}_X$ and $\delta_{f_{CFD}(\delta_X)}$ is a realization of f_{CFD} evaluated from a realization of the uncertain Random Variable (RV) X denoted δ_X . The assessment of this RV enables the evaluation of the bias and standard deviation of the CFD results when considering or not the inputs uncertainty. Different approaches to propagate inputs statistical moments or quantiles can be found in literature (Polynomial Chaos expansion, Monte-Carlo draws on surrogate model ...), and are reviewed for instance in [5] [6] [7]. The method used in this document to propagate the inputs uncertainty through CFD simulation is Deterministic Sampling (DS) which is detailed in references [8] and [9]. This method has been chosen for its significantly lower number of requested simulations for the assessment of the uncertainty. Once the statistical moments are propagated, different assumptions will be made on the output distribution using a distribution model, namely the Metalog distribution [10], to evaluate quantiles.

For this application on the Kozloduy 6 mixing experiment, four boundary conditions of the model indicated on Table 1 are set as uncertain. These parameters were chosen by the different partners because of their impact on the CFD outputs which have been deemed to be important in front of others.

Table 1: List of uncertain parameters for Kozloduy-6 mixing parameters

Inlet uncertain parameter	μ	σ
$X_1 = \Delta Q_1$: uncertainty of leg 1 inlet flowrate variation	0	91.32 kg/s
$X_2 = \Delta T_2$: uncertainty of leg 2 inlet temperature variations	0	1 °C
$X_3 = \Delta T_1$: uncertainty of leg 1 inlet temperature variations	0	1 °C
$X_4 = \Delta P_{core}$: uncertainty on core total power variations	0	60MW

The uncertain parameters are all set to a zero mean and are added to the baseline value of the transient. It should be noted that ΔQ_1 , ΔT_2 , ΔT_1 and ΔP_{core} are added as a constant on the time

evolving signals Q_1, T_2, T_1 and P_{core} as we assume that ΔX (X being the parameter of interest) is a systematic bias during the transient and does not evolve in time.

2. Numerical methods for uncertainty quantification

2.1. Covariance propagation using deterministic sampling

2.1.1. Principle of the method

The methodology used to propagate uncertainties with DS is based on references [8] and [9]. Propagating uncertainties with DS is similar to propagating uncertainties with Random Sampling (RS). In fact, both methods first rely on the representation of a random variable (RV) with a finite sample:

- RS: the sample is drawn randomly, the representativity of the sample regarding the real RV gets better as the size of the sample increases. The representation error is directly connected to the sampling which should include an important number of samples (at least 1000) to reach an acceptable representativity of the RV.
- DS: the sample is drawn by applying deterministic rule. The rule suggested in reference [8] is the conservation of statistical moments. As for RS, an increasing number of samples will allow the representation of an increasing number of statistical moments and thus enhance the representation of the RV.

Both RS and DS methods have their advantages, which are respectively an exact convergence toward a given probability density function insured by the Central Limit Theorem for RS and a quick but approximate convergence for DS. When the sample representing the random inputs is chosen, the propagation through CFD is done in a non-intrusive way by evaluating each set of inputs of the sample with a computation. The statistics of the outputs are then assessed from the output sample.

2.1.2. Encoding statistical moments with deterministic sampling

Throughout the rest of this document, the deterministic samples which form the design of experiment of the study will be named ensembles. DS ensembles are provided as a pair with a weight vector. The nomenclature is the following for a RV $\mathbf{X} = (X_1, X_2, \dots, X_p)$ of dimension p , encoded by an ensemble of size N :

$$\mathbf{W} = \begin{pmatrix} w_1 \\ \vdots \\ w_N \end{pmatrix} \text{ is the weight vector, } \underline{\Sigma} = (\tilde{\mathbf{X}}_i)_{i \leq p} = \begin{pmatrix} \tilde{X}_1^{(1)} & \dots & \tilde{X}_p^{(1)} \\ \vdots & \ddots & \vdots \\ \tilde{X}_1^{(N)} & \dots & \tilde{X}_p^{(N)} \end{pmatrix} \text{ is the ensemble.}$$

The number of columns of the ensemble is the number of parameters, and the number of lines is the number of chosen samples of the ensemble. Each line of the sample is called a sigma point. The weights are sought such as:

$$\sum_{k=1}^N w_k = 1 \tag{2-1}$$

This condition is sought to have an unbiased estimator of the statistical moments. The deterministic rule followed to choose an ensemble is the conservation of statistical moments. The first statistical moment is the mean value that can be calculated for all parameters X_i as follows from the ensemble and weights:

$$\langle X_i \rangle = \sum_{k=1}^N w_k \tilde{X}_i^{(k)} \quad (2-2)$$

The marginal moment of order m of parameter X_i is evaluated from a DS ensemble with the following formula:

$$\langle \delta X_i^m \rangle = \sum_{k=1}^N w_k (\tilde{X}_i^{(k)} - \langle X_i \rangle)^m \quad (2-3)$$

The four first moments are respectively the mean value, the variance, the skewness and the kurtosis. In addition, the mixed moment of order $m = m_i + m_j + \dots + m_l$ of the RV $\langle \delta X_i^{m_i} \delta X_j^{m_j} \dots \delta X_l^{m_l} \rangle$ is calculated as follows:

$$\langle \delta X_i^{m_i} \delta X_j^{m_j} \dots \delta X_l^{m_l} \rangle = \sum_{k=1}^N w_k (\tilde{X}_i^{(k)} - \langle X_i \rangle)^{m_i} (\tilde{X}_j^{(k)} - \langle X_j \rangle)^{m_j} \dots (\tilde{X}_l^{(k)} - \langle X_l \rangle)^{m_l} \quad (2-4)$$

If a DS ensemble which conserves chosen statistical moments is sought, a non-linear system of equation has to be formed from equations (2-1), (2-2), (2-3) and (2-4) for the chosen ensemble. This system can be written:

$${}^t \mathbf{W} \underline{\mathbf{S}} = \mathbf{M} \quad (2-5)$$

Where \mathbf{W} is the weights vector, $\underline{\mathbf{S}}$ is a matrix where are concatenated columns corresponding to the $\mathbf{1} = (1)_{1 \leq i \leq N}$ vector encoding (2-1) equation, and columns corresponding to the encryption of the different chosen statistical moment (mixed or marginal moment) obtained from equations (2-2), (2-3) and (2-4).

For instance, to encode only the mean value and the standard deviation for the p parameters X_i , the ensemble and weights $\underline{\mathbf{X}} = (\tilde{X}_i)_{i \leq N}$ and $\mathbf{W} = (w_1, \dots, w_N)$ must be solutions of the system (2-5) with $\underline{\mathbf{S}}$ written as following:

$$\underline{\mathbf{S}} = \begin{pmatrix} 1 & \tilde{X}_1^{(1)} & \tilde{X}_2^{(1)} & \dots & \tilde{X}_p^{(1)} & (\tilde{X}_1^{(1)} - \langle X_1 \rangle)^2 & \dots & (\tilde{X}_p^{(1)} - \langle X_p \rangle)^2 \\ 1 & \tilde{X}_1^{(2)} & \tilde{X}_2^{(2)} & \dots & \tilde{X}_p^{(2)} & (\tilde{X}_1^{(2)} - \langle X_1 \rangle)^2 & \dots & (\tilde{X}_p^{(2)} - \langle X_p \rangle)^2 \\ 1 & \tilde{X}_1^{(3)} & \tilde{X}_2^{(3)} & \dots & \tilde{X}_p^{(3)} & (\tilde{X}_1^{(3)} - \langle X_1 \rangle)^2 & \dots & (\tilde{X}_p^{(3)} - \langle X_p \rangle)^2 \\ \vdots & \vdots & \vdots & \dots & \vdots & \vdots & \dots & \vdots \\ 1 & \tilde{X}_1^{(N)} & \tilde{X}_2^{(N)} & \dots & \tilde{X}_p^{(N)} & (\tilde{X}_1^{(N)} - \langle X_1 \rangle)^2 & \dots & (\tilde{X}_p^{(N)} - \langle X_p \rangle)^2 \end{pmatrix}, \text{ and } \mathbf{M} = \begin{pmatrix} 1 \\ \langle X_1 \rangle \\ \langle X_2 \rangle \\ \vdots \\ \langle X_p \rangle \\ \langle \delta X_1^2 \rangle \\ \vdots \\ \langle \delta X_p^2 \rangle \end{pmatrix}$$

If marginal moments up to order m must be encoded, the number of equations that must be solved is $p \times m + 1$. This has an impact on the number of elements N of the sample that must be used to have a solution to the system. When mixed moments are added, the dimension of the system increases steeply. In the following section, the methodology used to choose an ensemble representing a given random variable will be detailed.

2.1.3. Propagation of statistical moments

The previous system (2-5) given to choose the ensemble $\underline{\mathbf{X}} = (\tilde{X}_i)_{i \leq N}$ and the weight vector $\mathbf{W} = (w_i)_{i \leq N}$ is non-linear which complicates its resolution and the exhibition of solutions. The approach used in this work and detailed in [9] to solve this system is to use a pertinent ensemble $\underline{\mathbf{X}}$ which is fixed as a constraint and the weights \mathbf{W} are chosen by solving the linear system for the weights w_i . The good representation of the RV relies on a good choice of the ensemble $\underline{\mathbf{X}}$ which should present a good structure in terms of combinations of parameters, and which should lead to acceptable

weights in term of values (low discrepancy between values and no negative values). The methodology to build ensembles relies on elementary bricks:

- activation matrices which present specific properties (symmetry, structure)
- elementary operations which are methods to combine the ensembles.

Elements on the methodology can be found with more details in Appendix A. For this application of the Kozloduy-6 mixing experiment, four parameters are set as uncertain. In addition, we assume that the 4D RV $\mathbf{X} = (X_1, X_2, X_3, X_4)$ follows a 4D gaussian distribution:

$$\mathbf{X} \hookrightarrow \mathcal{N}(\boldsymbol{\mu}_X, \underline{\mathbf{C}})$$

$$\boldsymbol{\mu}_X = (\mu_1, \mu_2, \mu_3, \mu_4), \quad \underline{\mathbf{C}} = \begin{pmatrix} \sigma_1^2 & 0 & 0 & 0 \\ 0 & \sigma_2^2 & 0 & 0 \\ 0 & 0 & \sigma_3^2 & 0 \\ 0 & 0 & 0 & \sigma_4^2 \end{pmatrix}$$

Where, $\boldsymbol{\mu}_X$ is the mean realization of the RV \mathbf{X} and $\underline{\mathbf{C}}$ is the covariance matrix. This specific covariance matrix implies that the different 1D random variables X_1, X_2, X_3 and X_4 are independent which is an assumption of this study. The terms $\sigma_1, \sigma_2, \sigma_3$ and σ_4 are the standard deviations assumed of the four parameters.

Two basic ensembles with equal weights are used for propagation in this document:

- The Standard matrix named Σ_{STD} which originates from the Unscented Kahlman Filtering context for covariance propagation (see [11]).
- The Hadamard matrix named Σ_{HAD} which shows some similarities to the binary matrix of reference [8].

$$\Sigma_{STD} = 2 \begin{pmatrix} \sigma_1 & 0 & 0 & 0 \\ -\sigma_1 & 0 & 0 & 0 \\ 0 & \sigma_2 & 0 & 0 \\ 0 & -\sigma_2 & 0 & 0 \\ 0 & 0 & \sigma_3 & 0 \\ 0 & 0 & -\sigma_3 & 0 \\ 0 & 0 & 0 & \sigma_4 \\ 0 & 0 & 0 & -\sigma_4 \end{pmatrix}, \quad \Sigma_{HAD} = \begin{pmatrix} \sigma_1 & \sigma_2 & \sigma_3 & \sigma_4 \\ -\sigma_1 & \sigma_2 & -\sigma_3 & \sigma_4 \\ \sigma_1 & -\sigma_2 & -\sigma_3 & \sigma_4 \\ -\sigma_1 & -\sigma_2 & \sigma_3 & \sigma_4 \\ \sigma_1 & \sigma_2 & \sigma_3 & -\sigma_4 \\ -\sigma_1 & \sigma_2 & -\sigma_3 & -\sigma_4 \\ \sigma_1 & -\sigma_2 & -\sigma_3 & -\sigma_4 \\ -\sigma_1 & -\sigma_2 & \sigma_3 & -\sigma_4 \end{pmatrix}$$

In addition, these ensembles were combined to enforce additional statistical moments:

- The Gauss Heavy Middle ensemble Σ_{GHM} which adds the mean central point into the Hadamard matrix to enforce a 4th marginal moment $\langle \delta^4 X_j \rangle = 3$. Elements on the addition of the $\mathbf{0}$ vector and the modification of the weights can be found in reference [9].
- A hybrid ensemble Σ_{KRT} which concatenates the Standard ensemble and Hadamard ensemble and enables to enforce additional mixed moments of order 4 ($\langle \delta X_i^2 \delta X_j^2 \rangle = 1$). This ensemble is declined in two versions.

$$\Sigma_{GHM} = \begin{pmatrix} 0 \\ \sqrt{3} \cdot \Sigma_{HAD} \end{pmatrix}, \quad \Sigma_{KRT,1} = \begin{pmatrix} \sqrt{2} \cdot \Sigma_{HAD} \\ 0 \\ \Sigma_{STD} \end{pmatrix}, \quad \Sigma_{KRT,2} = \begin{pmatrix} \sqrt{3} \cdot \Sigma_{HAD} \\ \sqrt{3} \cdot \Sigma_{STD} \end{pmatrix}$$

It should nevertheless be noted that these ensembles are based on Hadamard ensemble which does not induce a total independence between parameters. In fact, $\langle \delta X_1 \delta X_2 \delta X_3 \rangle \neq 0$ which is expected for totally independent variables.

A summary of the enforced moments for the different ensembles is given on Table 2. It should be noted that the residuals giving the aimed moment and the enforced moment should be indicated in order to quantify how far the DS ensemble chosen is from the aimed RV. In this document this has not been done.

Table 2: List of enforced statistical moment for a 4D gaussian RV with the different ensembles

Ensemble	N_Σ	Marginal moments			Mixed moments		
		$M_{marginal}^{(2)}$	$M_{marginal}^{(3)}$	$M_{marginal}^{(4)}$	$M_{mixed}^{(2)}$	$M_{mixed}^{(3)}$	$M_{mixed}^{(4)}$
Standard	8	4/4	4/4	0/4	6/6	16/16	25/31
Hadamard	8	4/4	4/4	0/4	6/6	15/16	31/31
Gauss Heavy middle	9	4/4	4/4	4/4	6/6	15/16	25/31
Hybrid "KRT" 1 and 2	17	4/4	4/4	4/4	6/6	15/16	31/31

2.2. Proper Orthogonal decomposition

POD (Proper Orthogonal Decomposition) aims to generate a modal decomposition of functions based on observations. This technique is used in a wide range of domains and is known under different names:

- Karhun-Loève Transform (KLT) in pattern recognition [12]
- Principal Components Analysis (PCA) in statistical literature (for example [13]).
- Proper Orthogonal Decomposition (POD) in mechanical engineering [14].

The use of POD in fluid mechanics answers to one problematic faced when studying the motion of turbulent flow, which is the reduction of the turbulent motion to a limited number of parameters. The use of POD in fluid mechanics for the study of turbulence is now widely spread and an early review can be found in [15] while the mathematical aspects of this decomposition can be found in an educational way in references [16] [17].

The use of POD in fluid mechanics is not restricted to the study of turbulence and has spread to other connected fields. For instance, in the uncertainty quantification of CFD codes context, methods based on POD are used for instance in [18] [19] for their ability to reduce the outputs dimension.

In this document, POD is used specifically for its ability to reduce the output dimension and to capture spatial correlations between fluctuations. The work presented in this document is based on the Snapshot method given in [12]. In this document, POD is used to study the variability of 2D fields $(f_{CFD}(x, y, \mathbf{X}_i))_{i \leq N_{SNAP}}$ where $\mathbf{X}_i = (X_1, X_2, X_3, X_4)_i$ is the set of inputs for a simulation i . In practice, N_{SNAP} realizations of f_{CFD} are available and enable the calculations of POD modes $(\phi_k)_{k \leq N_{POD}}$ and eigenvalues $(\lambda_k)_{k \leq N_{POD}}$ which are found by solving an eigenvalue problem. These modes can then be used to express the snapshots f_{CFD} as follows:

$$f_{CFD}(x, y, \mathbf{X}_i) = \sum_{k=1}^r a_k(\mathbf{X}_i) \phi_k(x, y) + \epsilon_r$$

With ϵ_r the truncation error of the POD of order r , and a_k components that can be calculated for each snapshot with the following formula:

$$a_k(\mathbf{X}_i) = \iint_S f_{CFD}(x, y) \phi(x, y) dx dy$$

In the present application, the spatial dimension is discretized which simplifies the calculation of the integral.

Regarding the truncation error ϵ_r , its amplitude converges to zero when the order r gets closer to N_{POD} . In addition, the POD base presents the advantage of classifying the different modes by order of importance. In fact, the POD is built by satisfying an optimality criterion, the POD provides a reduced dimension subspace of the input vectors on which the error between the projection and the original vector is minimized (see for instance reference [17]). The consequence is that most of the time, the number of modes that can be chosen is much smaller than the dimensionality of the original input as spatial correlations are detected between the fields. A way to choose the number of modes is to look the Relative Information Content (RIC) number which is defined as following from the eigenvalues of the POD base:

$$RIC(i) = \frac{(\sum_{k=1}^i \lambda_k)}{\sum_{k=1}^{N_{POD}} \lambda_k} \tag{2-6}$$

In practice, the truncation order r is chosen such as $RIC(r) > 0.99$. If this constraint is not sufficient to have a negligible truncation error ϵ_r additional modes can be kept.

3. Data processing

3.1. Quantities of interest

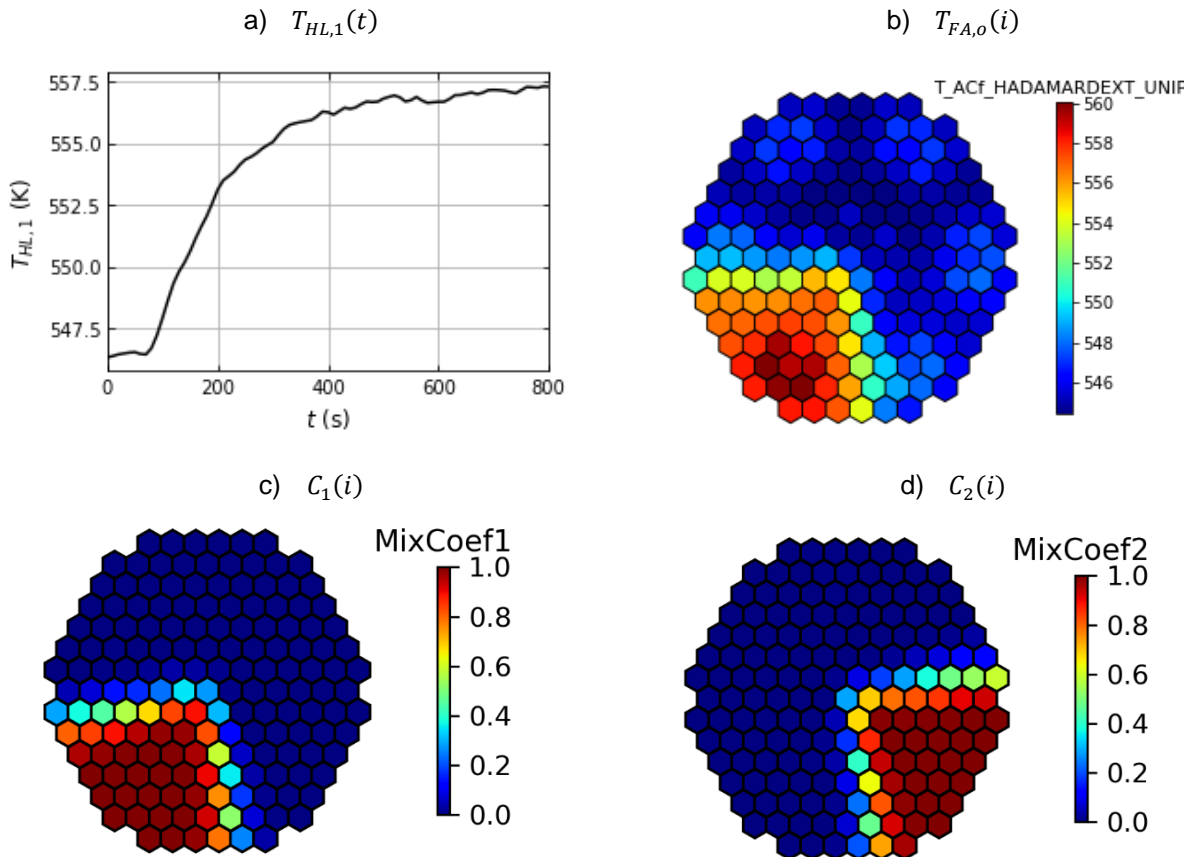


Figure 1 : examples of postprocessed fields from a CFD simulation

The quantities of interest for the uncertainty quantification study presented in this document are:

- The increase of temperature in the hot leg 1 during the transient $T_{HL,1}(t)$. An example is given on Figure 1a.
- The core outlet temperature: a map of the fuel assemblies' (FA) outlet temperature is extracted $T_{FA,o}(i)$ with i being the index of the FA. A view of $T_{FA,o}(i)$ is given on Figure 1b.
- The mixing map of the core constructed with 4 passive scalar fields injected respectively in the four cold legs of the circuit. The four mixing coefficient fields in the core are denoted with the symbol $C_{mix,j}(i)$ where j is the index of the cold leg of interest and i the index of the FA of interest. $C_1(i)$ and $C_2(i)$ are given respectively on Figure 1c and Figure 1d.

3.2. Filtering of the signal

The data presented in the previous paragraph is processed to highlight variations on the results of the different computations due to the variations of input parameters. Some of the data that are processed in this work are time evolving signals which can present some important time fluctuations. The combination of the variability between signals and of the time fluctuations can be of two types:

- Variability between signals with small time fluctuations.
- Variability between signals with large time fluctuations.

Examples of these two types of variability are depicted on Figure 2. These two kinds of variability are both important to make confidence intervals. If we look for instance to signals which show correlated time fluctuations as it can be seen Figure 2a, the amplitude of the time fluctuations will have small impact on the calculation of the discrepancy between signals. On the other side, if time fluctuations are uncorrelated, as it can be seen Figure 2b for some of the signals, the impact on the evaluated uncertainty can be important if the amplitudes are high. In fact, if the amplitude of the time fluctuations is bigger than the discrepancy between the signals, the resulting variance will be mostly due to the time fluctuations which will hide the correlation between the CFD output variation with respect to the inputs' variations. In this work, a filtering of the signal is performed with POD by truncating the signals with a limited number of modes to study whether it brings out correlation of the output to the inputs.

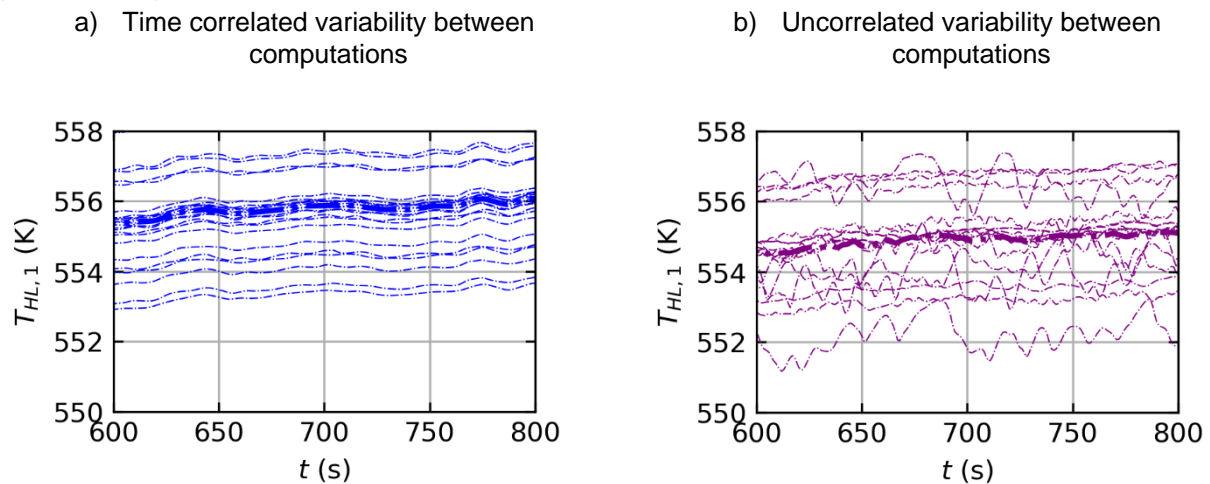


Figure 2 : examples of evolution of $T_{HL,1}$ on the last 200s of the transient simulation with two models. The red line corresponds to the reference calculation while blue and black curves correspond to simulation evaluated with different DS ensembles.

The filtering of the signals is illustrated on Figure 3. The filtering of the snapshots $(T_{HL,1}(t_i, \mathbf{X}_j))_{j \leq N_\Sigma}$ is obtained by applying the truncated POD of order r :

$$T_{HL,1,r}(t_i, \mathbf{X}_j) = \langle T_{HL,1} \rangle + \sum_{k=1}^r a_k(\mathbf{X}_j) \phi(t_i)$$

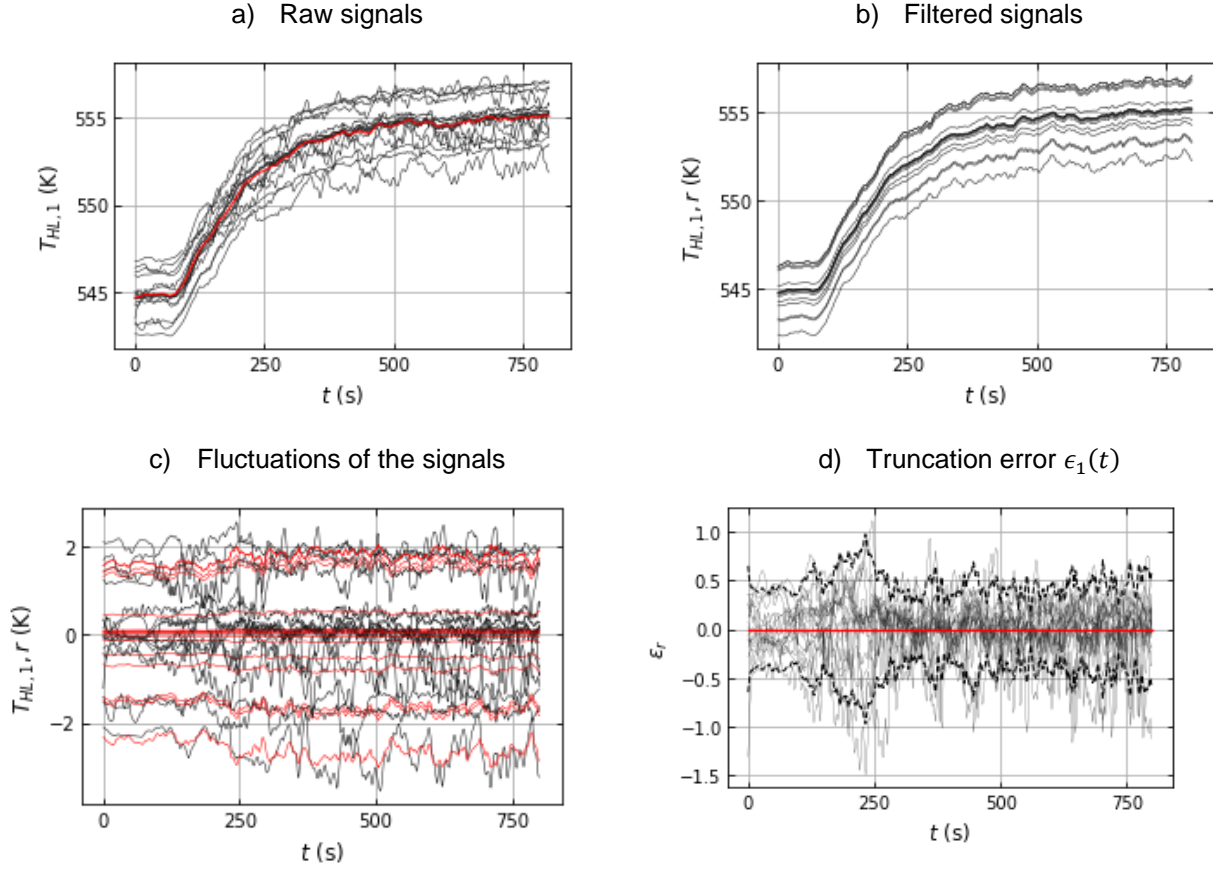


Figure 3 : Illustration of the quantity of interest during the filtering process. a) superposition of the raw signals and b) superposition of the filtered signal with $r = 1$. On c) the red part corresponds to a reconstruction of the fluctuations with 1 mode. The associated truncation error is given on d): mean value over time in red, black lines corresponds to an interval $\mu \pm 1.65\sigma$ while the grey lines correspond to realizations of the truncation error on the different snapshots.

The truncated fluctuations are denoted $T'_j(r, \mathbf{t})$:

$$T'_j(r, \mathbf{t}) = \sum_{k=1}^r a_k(\mathbf{X}_j) \phi(t_i)$$

A ratio can be calculated to compare the time fluctuations of the signals in front of the variability of the signals and see its impact on the assessment of correlations:

$$R = \frac{\langle \sigma_{T'(r,t)} \rangle_t}{\langle \sigma_{T'_j(r,t)} \rangle_{j \leq N_\Sigma}}$$

Where $\sigma_{T'(r,t)}$ is the time evolution of the standard deviation between the filtered signals evaluated over the ensemble Σ , and $\sigma_{T'_j(r,t)}$ the standard deviation of signal $T'_j(r, \mathbf{t})$ evaluated over time. These two standard deviations are then averaged respectively over time and over the ensemble to compute the ratio.

3.3. Determination of quantiles

The evaluation of the CFD outputs with DS ensembles presented in §2.1.3 enables the evaluation of statistical moments up to order 2 to 4 depending on the complexity of the ensemble. These statistical moments can then be used with additional assumptions on the output's distribution to assess a PDF, CDF, or quantiles. In this work, the additional information provided by the statistical model will be used to provide q -quantiles which represent a boundary under which a proportion q of the population is represented.

For instance, if we assume that the output RV Y follows a gaussian distribution q -quantiles can be assessed as following:

$$Q_q = \mu_Y + k(q) \cdot \sigma_Y \quad (3-1)$$

Where k depends on the percentage of realization that must be bounded. For instance, the 2.5% quantile is obtained for $k(0.025) = -1.96$, a 5% quantile for $k(0.05) = -1.65$. In this work, the Metalog distribution introduced in [10] is used as a model distribution to reconstruct the output distribution. This distribution has been chosen for its easiness of use in addition to the diversity of shapes it reproduces. The Metalog distribution is defined from its quantile function $M_n(q)$ for n terms, with q being the percentage of realization that must be bounded as follows (see [10]):

$$M_n(q) = \begin{cases} a_1 + a_2 \ln\left(\frac{q}{1-q}\right) & \text{for } n = 2 \\ a_1 + a_2 \ln\left(\frac{q}{1-q}\right) + a_3(q - 0.5) \ln\left(\frac{q}{1-q}\right) & \text{for } n = 3 \\ a_1 + a_2 \ln\left(\frac{q}{1-q}\right) + a_3(q - 0.5) \ln\left(\frac{q}{1-q}\right) + a_4(q - 0.5) & \text{for } n = 4 \\ M_{n-1}(q) + a_n(q - 0.5)^{\left(\frac{n-1}{2}\right)} & \text{for odd } n \geq 5 \\ M_{n-1}(q) + a_n(q - 0.5)^{\left(\frac{n-1}{2}\right)} \ln\left(\frac{q}{1-q}\right) & \text{for even } n \geq 6 \end{cases} \quad (3-2)$$

The coefficients $(a_i)_{i \leq n}$ can be determined if discrete coordinates of the CDF are given. An alternative way of determining the coefficients is from the statistical moments.

In this work, a decomposition with three or four terms is studied. For these decompositions, a closed form expressing the four first order moments with the coefficients is given in [10]. A four term Metalog distribution is first fitted which is then verified according to the validity domain of the Metalog model. If the provided distribution is outside the domain of validity (in practice, noticed due to non-monotone quantile function), a three term Metalog is fitted. The coefficients a_1, a_2, a_3 and a_4 are obtained by solving the system provided in [10] with the python module `scipy` [20]. The q -quantiles are then assessed directly from this function M_k . Calculating the derivative of M_k provides the probability density function (PDF) m_k .

3.4. Sensitivity analysis

3.4.1. Evaluation of the statistical quantities

Statistical quantities can be computed from the N_Σ computations launched. First, the DS approach of using weights is used to compute the mean and standard deviation from each ensemble $\underline{\Sigma}$:

$$\mu_Y = \sum_{i=1}^{N_\Sigma} w_i Y^{(i)}, \quad \sigma_Y = \sqrt{\sum_{i=1}^{N_\Sigma} w_i (Y^{(i)} - \mu_Y)^2}$$

Where $(w_i)_{i \leq N_\Sigma}$ are the weights of the ensemble $\underline{\Sigma}$ and $(Y^{(i)})_{i \leq N_\Sigma}$ the evaluation of quantity Y over the sigma points of ensemble $\underline{\Sigma}$ which have been filtered with the approach described in the previous paragraph. Higher order centered statistical moments are evaluated with (2-3) and (2-4). In this study we will evaluate statistical moments up to order 4.

In addition, the sensitivity of a quantity Y to the four inputs X_1, X_2, X_3 and X_4 is evaluated from the covariance and correlation coefficients calculated as following:

$$\text{cov}(X_j, Y) = \sqrt{\sum_{i=1}^{N_\Sigma} w_i (Y^{(i)} - \mu_Y) (X_j^{(i)} - \mu_{X_j})}, \quad \text{corr}(X_j, Y) = \frac{\text{cov}(X_j, Y)}{\sqrt{\text{cov}(X_j, X_j) \cdot \text{cov}(X_j, Y)}}$$

Correlation and covariance will be evaluated on filtered signal when required if the data is too noisy. An illustration of the way to interpret correlation is shown on Figure 4. It can be seen on this figure that Y is highly correlated to X_1 which means $\text{corr}(X_1, Y)$ will be close to 1, is anti-correlated to X_2 meaning $\text{corr}(X_2, Y)$ will present a more moderate negative value (in this case $\text{corr}(X_2, Y) \approx -0.4$) and presents small to no correlation to X_3 and X_4 .

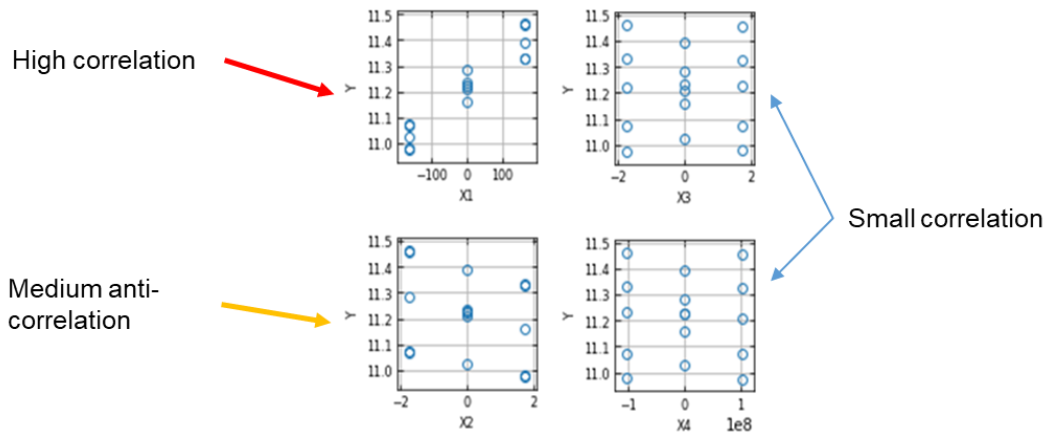


Figure 4: illustration of different correlation degrees between parameter Y and inputs X_1, X_2, X_3 and X_4

3.4.2. Processing of spatial data

For 2D data, an additional step is performed with POD to find spatial correlations between the CFD outputs obtained on the ensembles $\underline{\Sigma}$. The method will be illustrated on the i -th Fuel Assembly (FA) outlet temperature $T_{FA,o}(i)$ where i corresponds to the index of the FA.

If we take for instance an ensemble $\underline{\Sigma}$ for which N_Σ evaluations of $T_{FA,o}(i)$ are available. First, the 2D fields are processed to be arranged in columns. The N_Σ snapshots available are concatenated in a snapshot matrix S . The mean value over all the columns $\langle T_{FA,o} \rangle$ is calculated and subtracted from

each column. The POD base is then computed with the python module **modred** [21] with the snapshot method described in [12]. It should be noted that the snapshots are not time fluctuations but fluctuations of the 2D fields due to the different inputs. The POD applied to $T_{FA,o}(i)$ enables the calculation of modes ϕ_k which can then be used to write for all snapshots $(T_{FA,o}(i, X_j))_{j \leq N_\Sigma}$:

$$T_{FA,o}(i, X_j) = \langle T_{FA,o} \rangle + \sum_{k=1}^r a_k(X_j) \phi_k(i) + \epsilon_r(i)$$

An illustration of the decomposition is given on Figure 5. This decomposition is useful when making a sensitivity study of 2D data to uncertain inputs as it enables the observation of different modes of variation which can be correlated to different inputs.

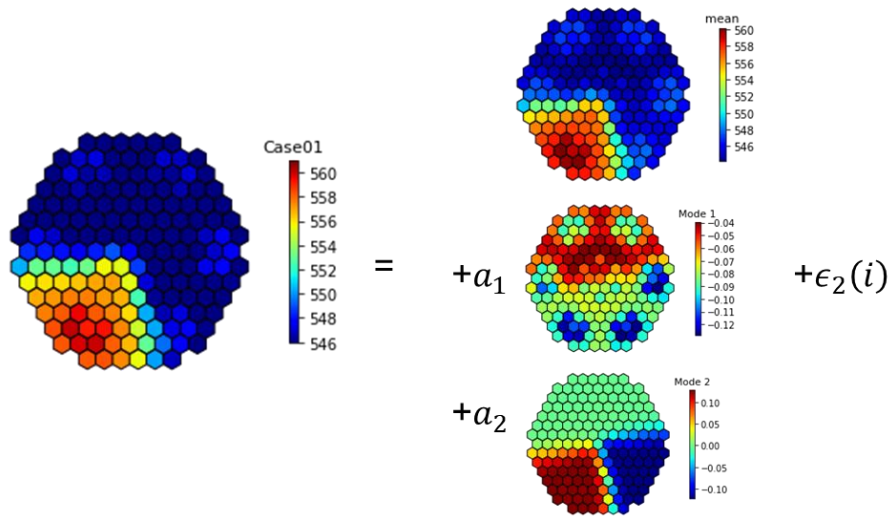


Figure 5: Illustration of the POD applied to $T_{FA,o}(i)$ with a truncation of order $r = 2$

It should be noted that time filtering has not been done on this quantity of interest which is only extracted at 800 s. Most of the models yield smooth data due to the choice of the turbulence model and meshing, however, some models are less dissipative and yield more time variation. For these cases, the time fluctuations have some impact on the calculation of spatial correlations as it will not be possible to separate these fluctuations from the fluctuations due to the sensitivity of the model to the inputs' variations.

3.5. List of performed computations

The list of computations performed are given in Table 3:

Table 3: List of ensembles chosen for the different partners

Partner	Standard	Hadamard	GHM	HYBRID KRT1	HYBRID KRT2
ENERGORISK	X			X	
FRAMATOME	X		X		X
KIT		X			
UNIPI		X	X		
CEA			X		

The results obtained by ENERGORISK, FRAMATOME, KIT and UNIPI models will be presented in the following section. The results obtained by CEA are given in Appendix C.

4. Results

4.1. Mixing coefficients

4.1.1. Overview of the results:

The mean value of the mixing coefficient C_1 evaluated on DS ensembles for the different models is given on Figure 6 and the standard deviation on Figure 7. Differences can be noticed between the mean values of C_1 obtained from the different models:

- ENERGORISK model shows more spread out non-zero values of C_1 in the core, especially at the junction between leg 1 and leg 2. In addition, this model yields more moderate values around 0.5 at the junction between legs indicating a more important mixing with the other legs when compared to other models. Also, C_1 presents slower spatial transition from $C_1(i) = 0$ to $C_1(i) = 1$.
- FRAMATOME, KIT and UNIPi models present lower mixing between the legs at the junction between the different zones with quick transition from $C_1(i) = 0$ to $C_1(i) = 1$. However, KIT model shows additional mixing with FA having values $C_1(i) \approx 0.2$ in the zones where most of the flow comes from leg 4 and leg 2.

Regarding the standard deviation, small amplitudes are found for all partners, except for ENERGORISK model which yields more important standard deviation at junction between the different zones on a non-negligible number of FA. The calculation of the mixing coefficient with this model is more sensitive to variation to inputs when compared to the other models, where the mixing coefficient is almost unchanged in the range covered by the uncertain input parameters. In addition to the difference in amplitude between ENERGORISK model and the other models, more FA are affected by the variability of the inputs with ENERGORISK model than the others. This difference between partners might be due to the choice of turbulence model and meshing which might smoothen fluctuation for the other partners and not for ENERGORISK model which yields more unsteady results.

Regarding the consistency of the evaluated standard deviation $\sigma_{C_1}(i)$, different ensembles yield very similar amplitudes and topology. More discrepancy is noticed between Σ_{STD} and the hybrid ensembles Σ_{GHM} and Σ_{KRT2} for FRAMATOME model. The same difference is noticed for ENERGORISK model, nevertheless, it is not clear in this case if the difference is due to the RV representation with Σ_{KRT1} and Σ_{STD} or to the important time variations that was observed on the mixing for this model. The results for the 3 other mixing coefficients C_2 , C_3 and C_4 show the same conclusions.

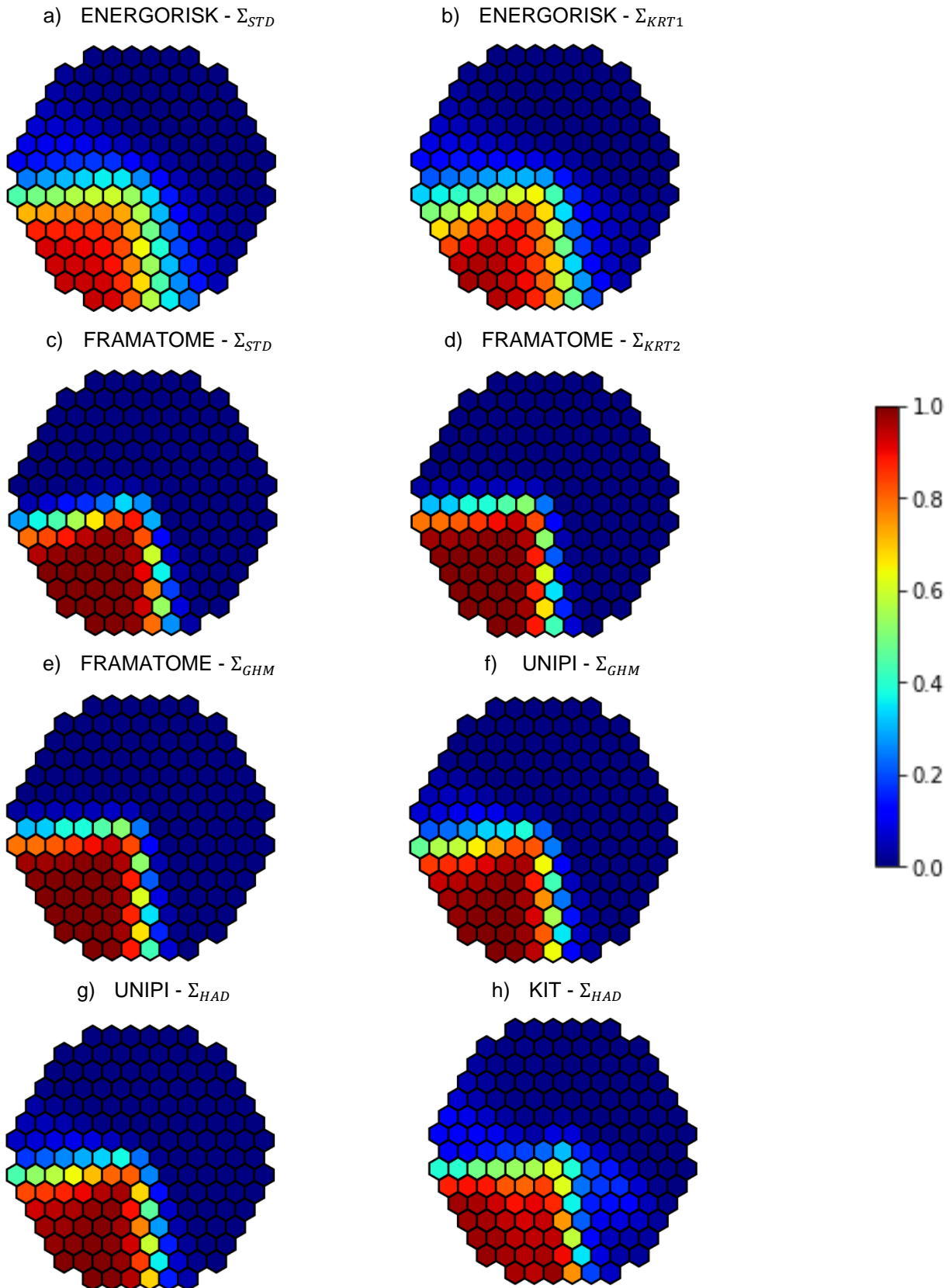


Figure 6 : Mean value of the mixing coefficient C_1 evaluated for different CFD models and DS ensembles.

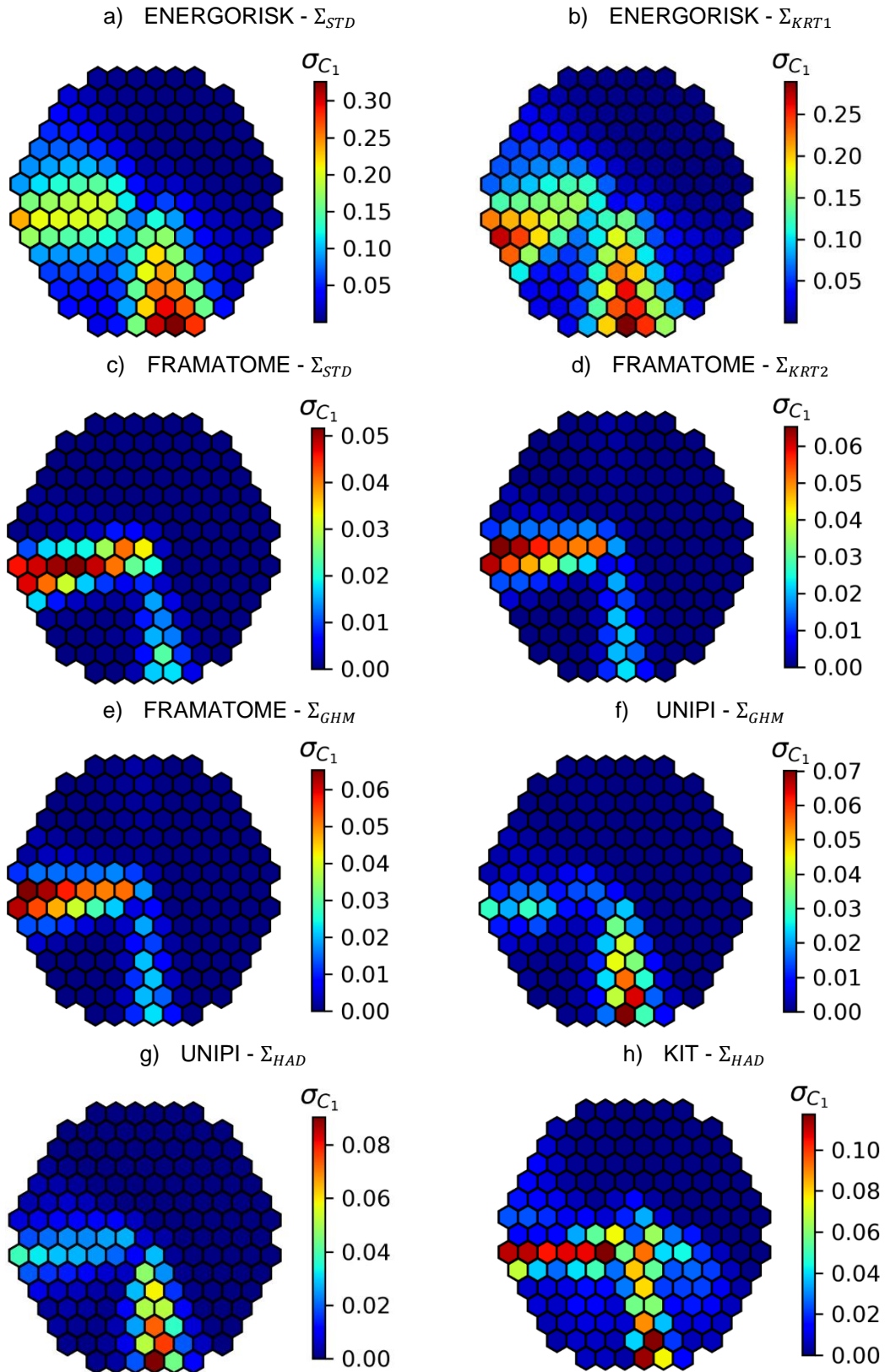


Figure 7 : Standard deviation of the mixing coefficient C_1 evaluated for different CFD models and DS ensembles.

4.1.2. Sensitivity analysis

In this section, POD is applied to the snapshots obtained from the different ensembles to see how the variations of the mixing coefficient topology are correlated to some of the input parameters. First, the RIC number (see (2-6)) of the first mode $RIC(1)$ is calculated for the POD applied to the different ensembles evaluated with the different CFD models, then the number of modes N_{POD} such as $RIC(N_{POD}) \geq 0.99$ is calculated. The results are given on Table 4.

A first remark general to all CFD models is the relative importance of the first mode which is significantly higher than for higher orders.

FRAMATOME model seem to show spatial fluctuations of the mixing in the core that can be expressed mainly with one mode. The second mode importance is significantly lower even though its use is required to reach $RIC(N_{POD}) \geq 0.99$. This is seen with the snapshots of Σ_{GHM} and Σ_{KRT2} ensembles. The mode that can be seen on Figure 8b shows that the variation of the inputs impact mainly the mixing between cold leg 1 and cold leg 4 and slightly the mixing between cold leg 1 and cold leg 2. This pattern is also observed for the standard deviation on Figure 7b which shows that the fluctuations are mainly due to this mode while the others can be neglected.

ENERGORISK model is also mainly affected by the first mode with smaller importance of the following ones but in this case, considering or not the 2nd mode changes noticeably the fluctuations amplitude in some FA. As for FRAMATOME model, the topology of the first mode can be noticed on the standard deviation 2D field on Figure 7a but many fuel assemblies' variations are not covered by this mode and require higher order modes to be represented.

KIT model first mode effect on the fluctuations appears clearly to be a rotation of the mixing in the core, and as for FRAMATOME, the higher order modes show less spatial correlation to identified phenomenon. When comparing the standard deviation of the mixing coefficients C_1 on Figure 7c, correlation to this mode 1 can be clearly seen.

UNIPI model shows similar results as FRAMATOME and KIT with spatial variations mainly reflected by the first mode topology. But, in this model, using one mode only enables the reproduction of fluctuations of the mixing between leg 1 and 2. The second mode is required to reproduce variation of the mixing between cold leg 1 and 4 which is visible on the standard deviation depicted Figure 7d.

In addition, the first mode for the four partners on different DS ensembles are given Figure 8.

Table 4 : RIC for one mode and number of modes N_{POD} required for $RIC(N_{POD}) \geq 0.99$

Partner - Ensemble	$RIC(N_{POD} = 1)$	N_{POD}
ENERGORISK Σ_{KRT1}	0.7	8
ENERGORISK Σ_{STD}	0.75	6
FRAMATOME Σ_{KRT2}	0.96	2
FRAMATOME Σ_{GHM}	0.98	2
KIT Σ_{HAD}	0.8	5
UNIPI Σ_{HAD}	0.8	3
UNIPI Σ_{GHM}	0.8	4

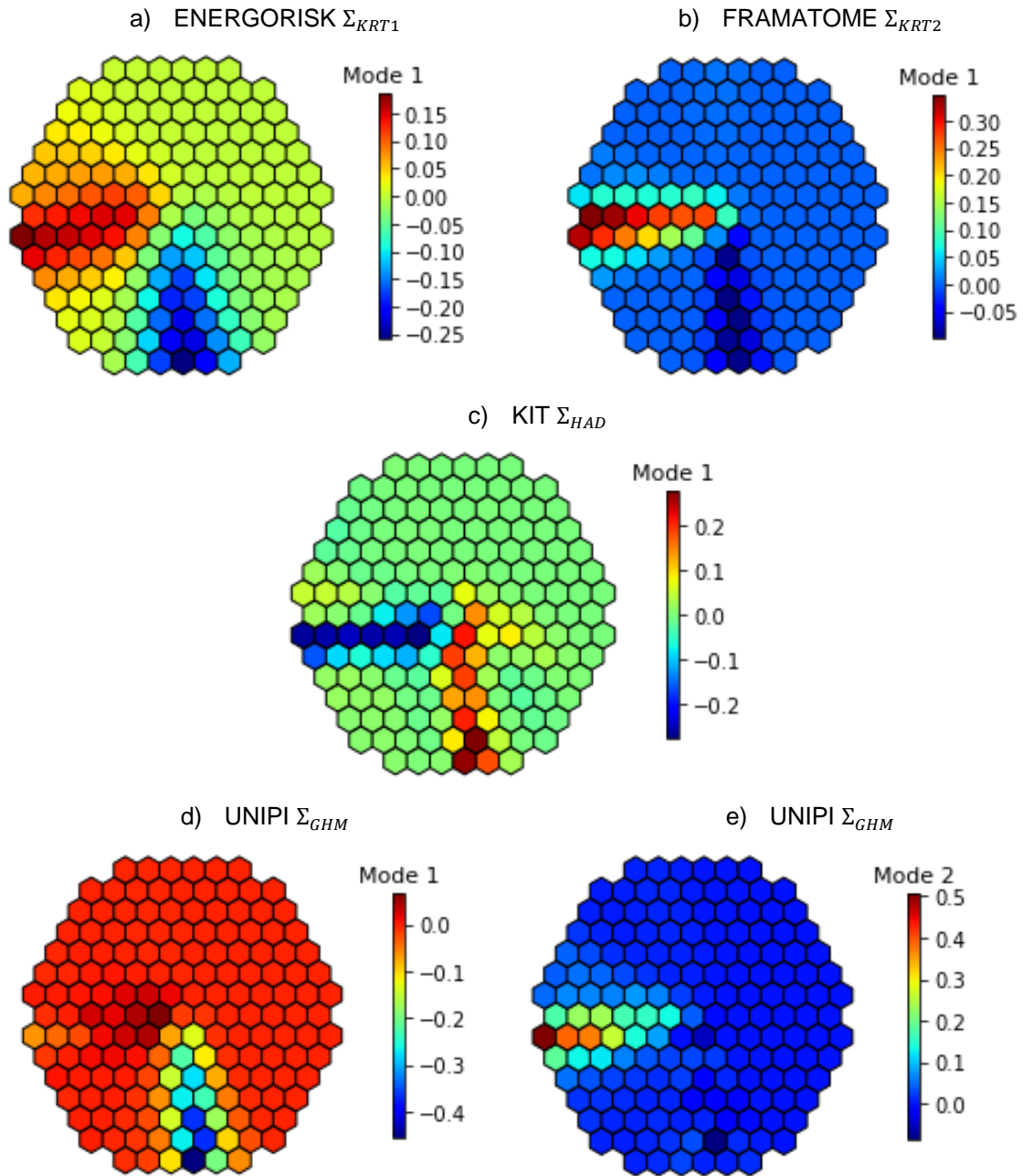


Figure 8 : Mode 1 of the POD applied to the snapshots of $C_1(i)$ obtained on different ensembles with different CFD models and mode 2 for UNUPI Σ_{GHM} snapshots

The evolution of the component a_1 with the input parameters is indicated on Figure 9. It can be noticed that the components a_1 from UNUPI and FRAMATOME model present high correlation to the flowrate values. In comparison, the correlation of a_1 to the inputs is unclear for ENERGORISK model while KIT model shows correlation to the total power in the core. Slight correlation to the flowrate is observed on KIT model but with a significantly lower amplitude than for UNUPI and FRAMATOME model. The results obtained for the other mixing coefficients were basically the same and are thus not described in this section.

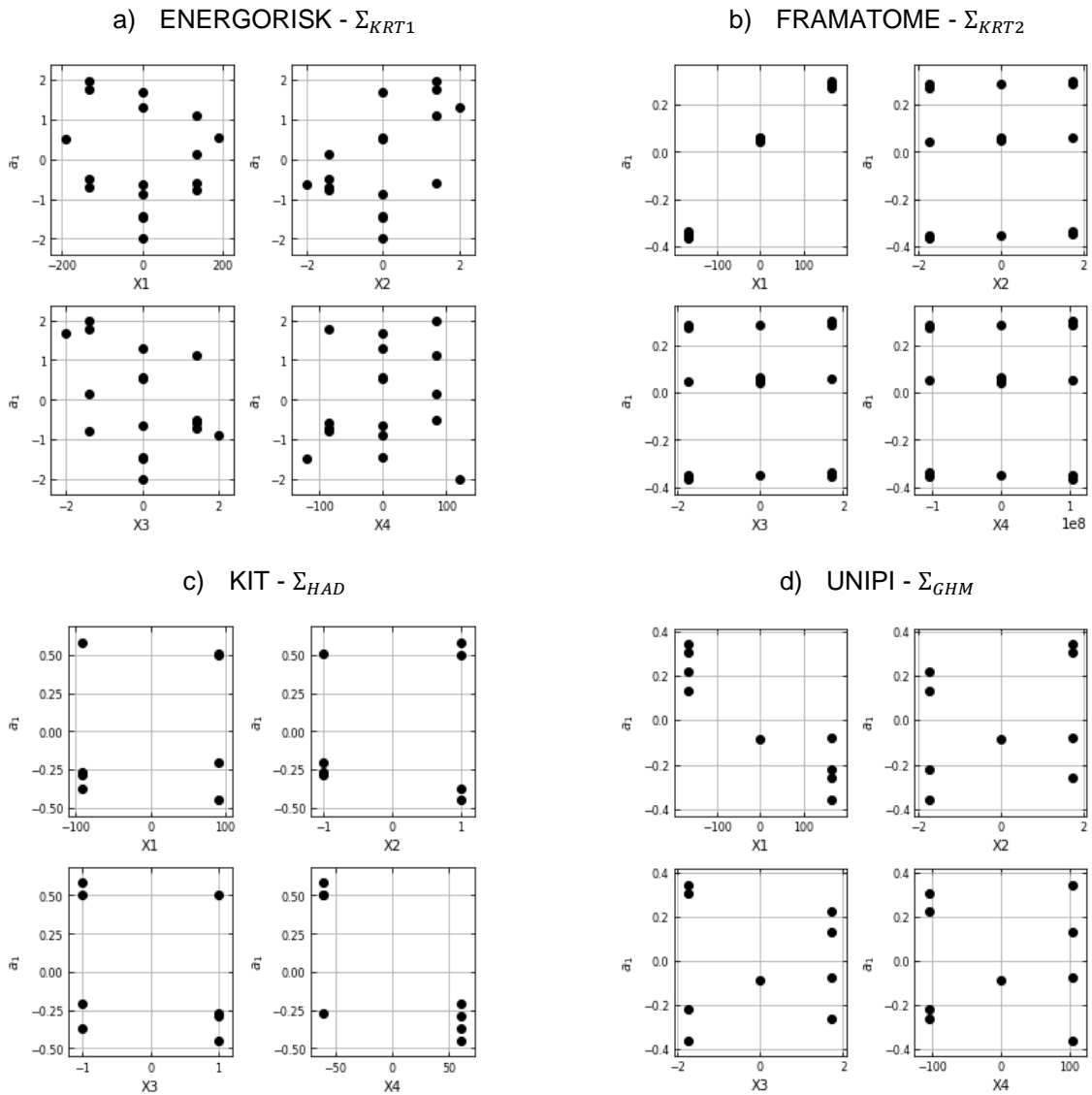


Figure 9 : Evolution of a_1 with the input parameters for POD performed on the results of the different CFD models/DS ensembles

4.1.3. Evaluation of quantiles

The quantiles of the mixing coefficient $C_1(i)$ are calculated using the 4 term Metalog distribution given in (3-2). The results for the different CFD models and DS ensembles are indicated on Figure 10. A preliminary remark that can be done is the fact that the fit of the Metalog distribution (3 or 4 term Metalog) on evaluations with ENERGORISK CFD model on Σ_{KRT1} model led to infeasible distributions on most of the fuel assemblies of the core (see Figure 11). The fit was successful for most of the FA in the core for all the other models/ensembles. Different remarks can be done on the results:

- The evaluation of the quantiles with ENERGORISK model on Σ_{STD} ensemble shows much more spread-out values of the mixing coefficients than the other models, reflecting the higher variability of the results with this model.
- Values obtained with FRAMATOME and UNIPI models show small variability with slight fluctuations that can be noticed near junctions.
- Quantiles are slightly more spread out for KIT model near junctions showing more variability of the mixing coefficient in the core.

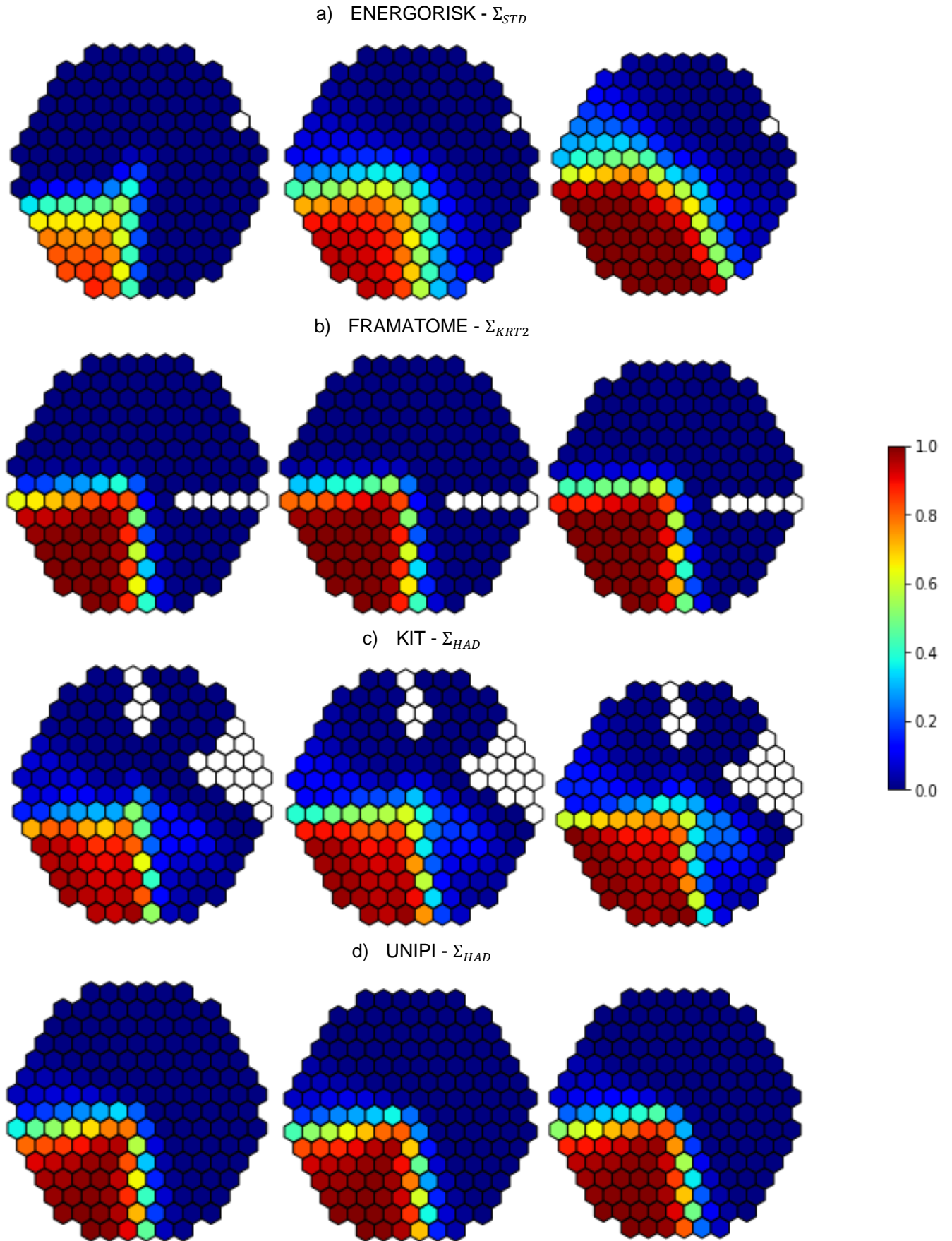


Figure 10 : Quantiles 2.5%, 50% and 97.5% on the mixing coefficient $C_1(i)$ for different ensembles and models. FA are white when the fitted Metalog distribution was infeasible.

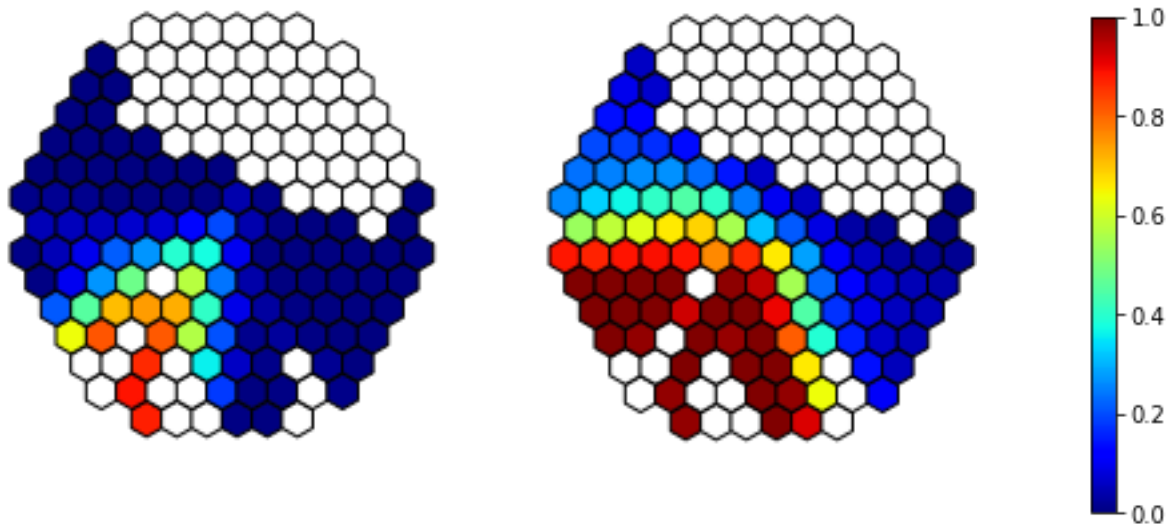


Figure 11 : 2.5% (left) and 97.5% (right) quantiles calculated with a Metalog distribution with ENERGORISK CFD model on Σ_{KRT} . FA are white when the fitted Metalog distribution was infeasible.

4.1.4. Discussion on the mixing coefficients results

The mixing coefficient has been found to vary slightly for FRAMATOME and UNIPI CFD models in the range covered by the evaluated ensembles, slightly more with KIT model and more significantly with ENERGORISK model. In this reproduction of the mixing experiment on Kozloduy-6 reactor, mixing in the core is a key phenomenon impacting the increase of temperature in hot legs during the transient when the temperature in cold leg 1 increases. For most of the partners the variations of the mixing map in the core were small, localized at junctions between zones influenced by the cold leg 1 and 2 and the junction between zones influenced by leg 1 and 4. Both FRAMATOME and UNIPI model found a correlation of the variations of the mixing map in the core to the flowrate in cold leg 1, while KIT model found correlation to the core power and ENERGORISK model no clear correlation. It should nevertheless be noted that the two most sensitive model relied on $k - \omega$ SST model which might be less dissipative and induce higher variations that are smoothed with the Standard $k - \epsilon$ model used by UNIPI and Realizable $k - \epsilon$ model used by Framatome (see [2] and [3] for more information on models).

Different DS ensembles were used to evaluate the uncertainty on the mixing coefficient which did not affect importantly the results, showing consistency of the method to propagate statistical moments. Some discrepancies were however noticed for ENERGORISK model which showed important variability of the mixing on the evaluation points. For this model, the low number of evaluations and the important discrepancy resulted in a more important deviations between the ensembles used to represent the random variable. However, the variations between the ensembles was still negligible on average in the core and showed important values (0.3 instead of 0.25 for the value of C_i) on a limited number of FA.

As a conclusion, the relatively low discrepancy of the results between the partners model which use different softwares, models and DS ensembles should still be noted.

Additional study on the combined effect of meshing and turbulence modelling should be done in the future to verify the effect of meshing in the model (grid size, type of cells, local refinement etc...) on the $k - \omega$ SST and $k - \epsilon$ time fluctuations.

4.2. Hot leg 1 temperature $T_{HL,1}$

4.2.1. Overview of the results variability

The signals giving the time evolution of the hot leg 1 temperature $T_{HL,1}(t)$ for all computations performed by the partners are given on Figure 12 and Figure 13a. The mean values over the computations are given on Figure 13b. Different remarks can be made on the results:

- Important variations can be noticed when considering uncertainties in comparison to the mean computations visible in black solid line on Figure 12. In fact, variation of parameters seems to guide the solution to lower values of the temperature during all the transient.
- The outputs mean values are similar between partners as it can be seen on Figure 13b with mean values showing small discrepancy (around 1°C).
- More time fluctuations of the temperature are noticed for ENERGORISK model on Figure 12a, which might be due to the more important fluctuation of the mixing map in the core as it has been noticed in the previous paragraph for $C_1(i)$. In comparison, the results obtained from the other partners were smooth with time fluctuations negligible in front of the discrepancy between the partners signals.

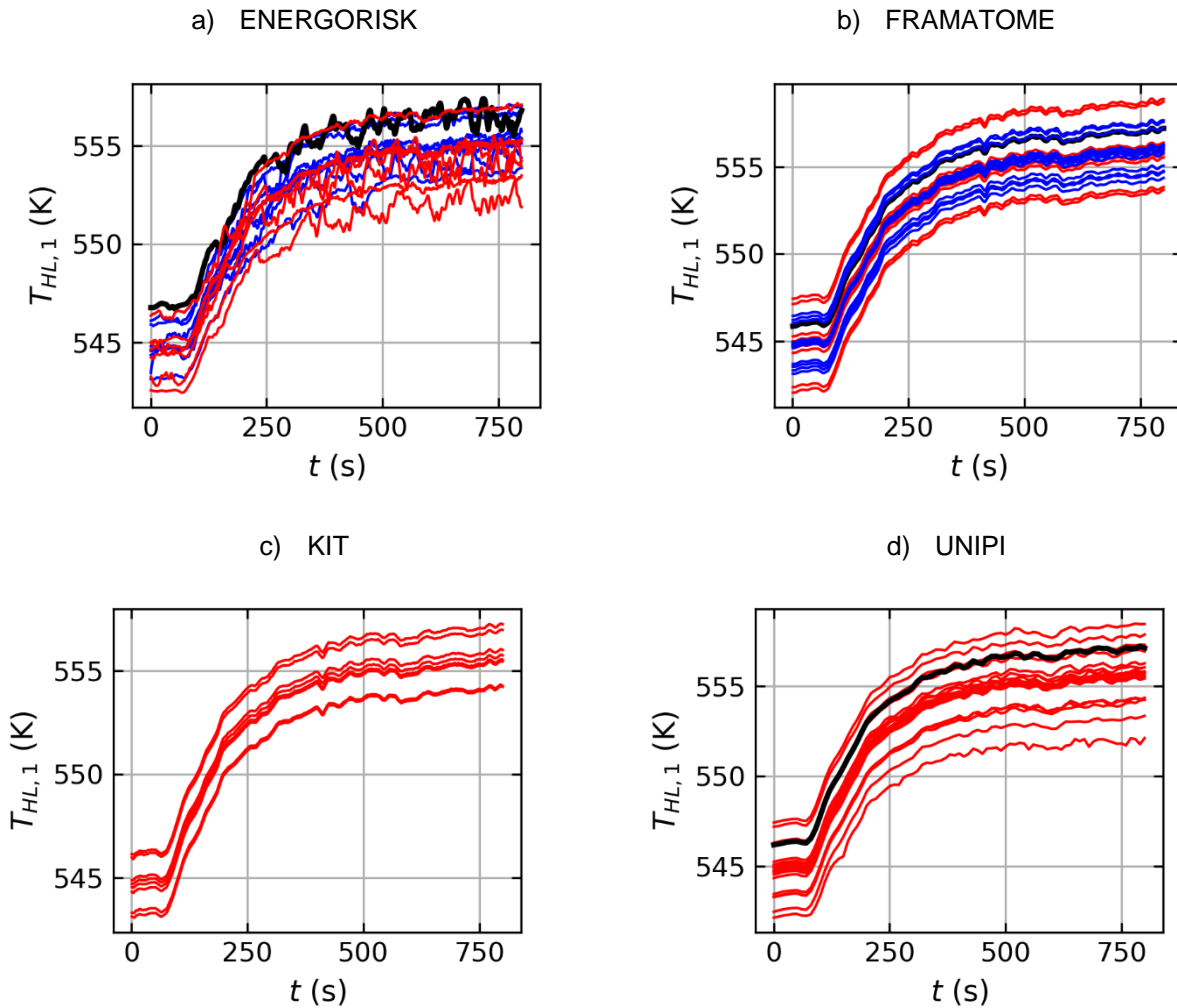


Figure 12: Time evolution of $T_{HL,1}$ obtained from the different ensembles and partners. Evaluation of CFD for the mean set of inputs (black) and for individual (red) and combined (blue) variations of inputs.

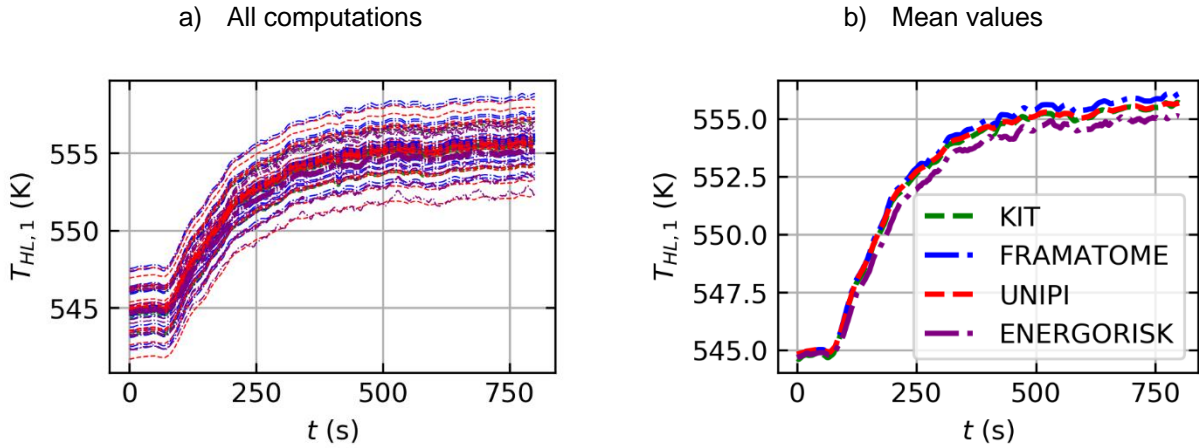


Figure 13: Comparison of the time evolution of increase of hot leg 1 temperature. All computations (a) and mean values (b).

4.2.2. Time fluctuations vs variability of signals due to inputs variability

A summary of the value of the ratio R which is the ratio between the amplitude of the time fluctuations of the signals and the amplitude of the variability between the signals over time is given in Table 5 for non-filtered signals and filtered signals ($r = 1$). The evolution of R with the truncation order r is given on Figure 14 .

Table 5: ratio R calculated before/after filtering (truncation with $r = 1$) for the different partners.

Partner	Filtered	No filter
FRAMATOME	$R = 0.002$	$R = 0.035$
ENERGORISK	$R = 0.057$	$R = 0.235$
KIT	$R = 0.003$	$R = 0.022$
UNIPI	$R = 0.018$	$R = 0.051$

The impact of the filtering is limited on FRAMATOME, UNIPI and KIT signals as the time fluctuations are small in amplitude in front of the variability of the signals (<5% in amplitude) while the impact is noticeable on ENERGORISK signals where the time fluctuations' amplitude are on average around 23% of the deviation between signals. These fluctuations are coherent with the results obtained in §4.1 where more variations of the mixing coefficients were found between the different computations. The impact on the hot leg 1 temperature downstream of the core is visible in this case.

For all partners, raw data will still be used for the evaluation of statistical moments. Filtering will be performed on ENERGORISK signals to see the potential effect on the statistical moments and evaluated correlation to input parameters.

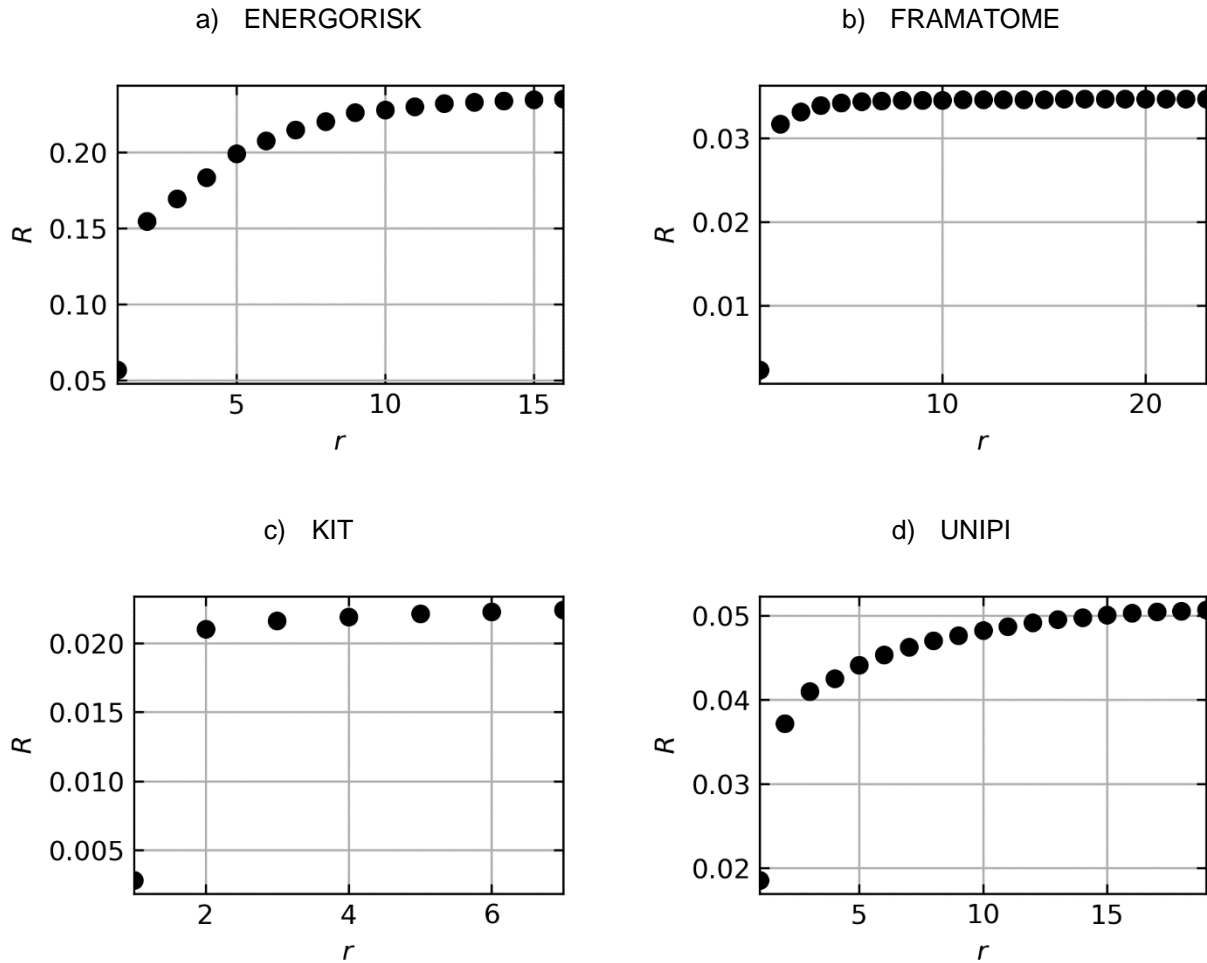


Figure 14: evolution of the ratio between time fluctuations and signal variability R with the truncation order of the filtering r .

4.2.3. Increase of temperature in the hot leg 1

The four first statistical moments are evaluated with all ensembles for all the partners for the increase of temperature in the hot leg 1 $\Delta T_{HL,1} = T_{HL,1}(t_0 + 800s) - T_{HL,1}(t_0)$. The statistical moments of $\Delta T_{HL,1}$ evaluated with the DS ensembles are summarized in Table 6.

The mean evaluated on FRAMATOME model with Σ_{STD} is 0.2°C lower than with Σ_{GHM} and Σ_{KRT2} . Similar differences are seen for ENERGORISK model with Σ_{STD} and Σ_{KRT1} evaluations in raw data. This might indicate a non-statistically converged result with Σ_{STD} which lacks in its representation of the RV as the combinations of simultaneous variations of inputs are not evaluated. The signals obtained from these inputs can be seen in red on Figure 12. It is visible that even though the amplitude of the variations of the input parameters are similar between the ensembles, the resulting discrepancy between the output is larger when the parameters vary simultaneously. This indicates the importance of evaluating the CFD response on those inputs.

Lower discrepancy between ensembles can be seen for the variance. The amplitude of the variance is more important on ENERGORISK model which yields signal presenting some higher amplitude time fluctuations which seems logical. When filtering, the variance decreases significantly and lower variations between ensembles can be seen. In comparison, UNIPI model evaluated on Σ_{GHM} is five time lower than non-filtered signals from ENERGORISK, but still approximately four time more important than other evaluations. This more important value of the variance might be due to the presence of one signal showing a more significant deviation as it can be seen on Figure 12d for the

signal with the lowest amplitude. The amplitude of the variance is the lowest for KIT model showing low discrepancy between the signals.

The ensembles which yield sparser results present higher values of skewness and kurtosis as it can be seen for UNIPI Σ_{GHM} signals and ENERGORISK nonfiltered signals. In addition, the discrepancy of the skewness and kurtosis between ensembles that enforces higher moments (Σ_{GHM} and Σ_{KRT}) and the other (Σ_{HAD} and Σ_{STD}) is not obvious.

Table 6 :Statistical moments on the output $Y = \Delta T_{HL,1}$

Partner	Ensemble	μ_Y	$\langle \delta^2 Y \rangle$	$\langle \delta^3 Y \rangle$	$\langle \delta^4 Y \rangle$
ENERGORISK	STD	10.734	2.5142e-1	1.3301e-1	2.5065e-1
	HYBKRT1	10.522	2.0049e-1	-2.6118e-2	2.1102e-1
	STD $r = 1$	10.395	8.7158e-3	-1.0450e-4	1.8219e-4
	HYBKRT1 $r = 1$	10.381	7.0479e-3	-3.2538e-4	2.5218e-4
FRAMATOME	STD	11.076	1.4757e-2	-5.3462e-4	8.6554e-4
	GHM	11.214	1.2457e-2	-1.3638e-4	6.0872e-4
	HYBKRT2	11.213	1.2560e-2	-2.4972e-4	4.6004e-4
KIT	HADAMARD	10.956	4.2190e-3	-2.3074e-5	2.2452e-5
UNIPI	HADAMARD	10.880	1.2232e-2	-1.6610e-4	1.8229e-4
	GHM	10.840	5.6689e-2	-4.6953e-2	4.9123e-2

The statistical moments were used to fit a k term metalog distribution given in (3-2). At first, a four term Metalog was fitted for $\Delta T_{HL,1}$ which yielded infeasible distributions for most of the results, thus a 3 terms metalog was fitted. Values of quantiles for all ensembles and partners can be found in Table 7.

The quantile functions $M_3(y)$ obtained for each partner and ensemble are given on Figure 15. It should be noted that the 3 term Metalog distribution could not be fitted on the GHM ensemble from UNIPI due to the high value of the skewness which is beyond the range of values acceptable for the Metalog distribution.

The derivative is calculated to evaluate the PDF which is given on Figure 16. It should be noted that the value of the kurtosis is not considered in the 3 term Metalog. Thus, ensembles which differ mainly by their statistical moments of order 4 will still show strong similarities as it can be seen on GHM and HYBKRT ensembles quantile function or PDF Figure 15b and Figure 16. In comparison, the Metalog fitted on statistical moments evaluated with STANDARD ensemble is shifted due to differences on the mean value. The distributions show low asymmetry. This can be noticed when comparing the median $Q_{50\%}$ to the mean value μ_Y for the different ensembles showing strong similarities. Slightly higher deviation between the median and mean value can be noticed on ENERGORISK model. In fact, a difference around 0.13°C between the median and mean value is calculated (non-filtered signals) which is coherent with the more important skewness indicated in Table 6.

Table 7 :Evaluation of quantiles on $Y = \Delta T_{HL,1}$ with different ensembles

Partner	Ensemble	$Q_{2.5\%}$	$Q_{5\%}$	$Q_{50\%}$	$Q_{95\%}$	$Q_{97.5\%}$
ENERGORISK	STD	9.97	10.09	10.64	11.67	11.95
	HYBKRT1	9.57	9.76	10.54	11.21	11.37
FRAMATOME	STD	10.82	10.87	11.08	11.26	11.31
	GHM	10.98	11.03	11.22	11.39	11.43
	HYBKRT2	10.98	11.03	11.22	11.39	11.43
KIT	HADAMARD	10.82	10.85	10.96	11.06	11.08
UNIFI	HADAMARD	10.64	10.68	10.81	10.95	10.99
	GHM	N.A.	N.A.	N.A.	N.A.	N.A.

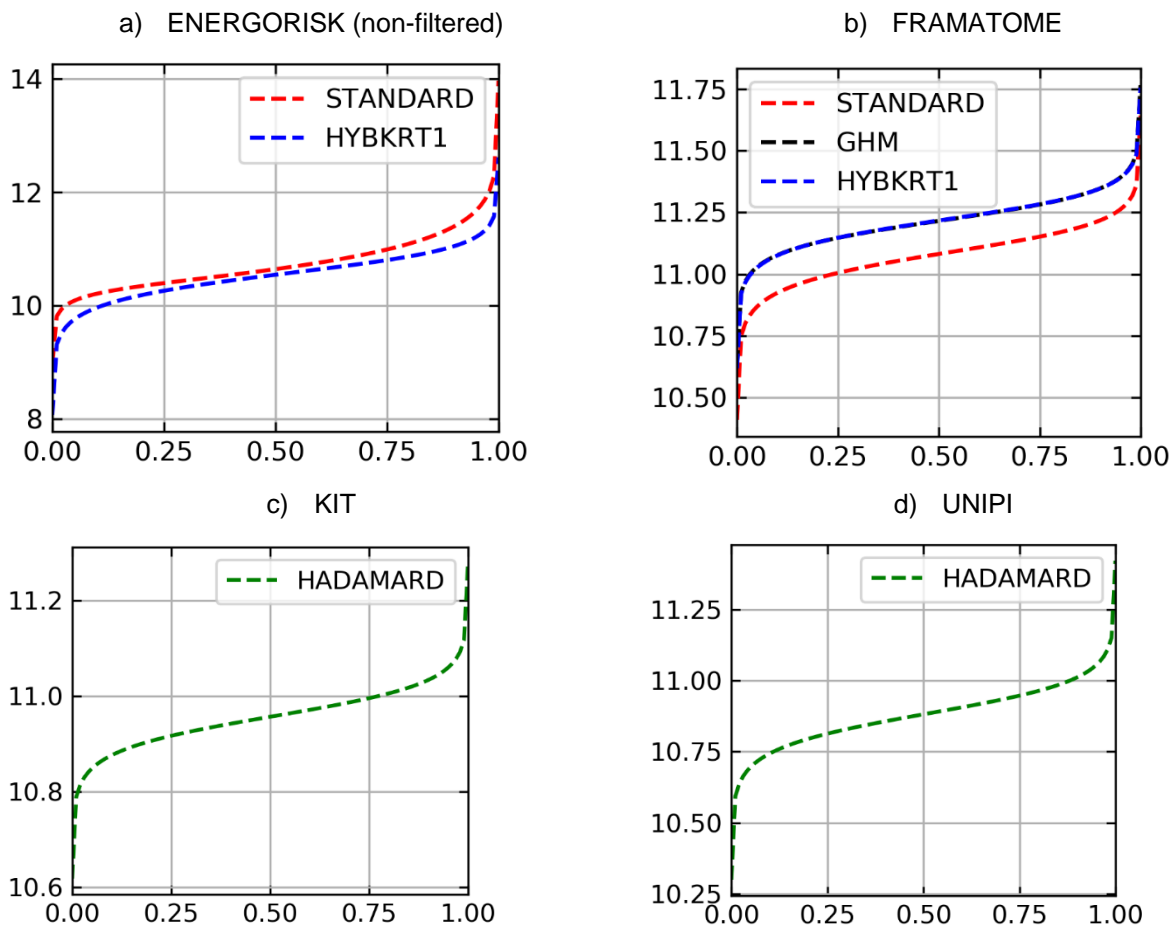


Figure 15: Quantile functions associated to the fitted Metalog distribution for the different ensembles and partners

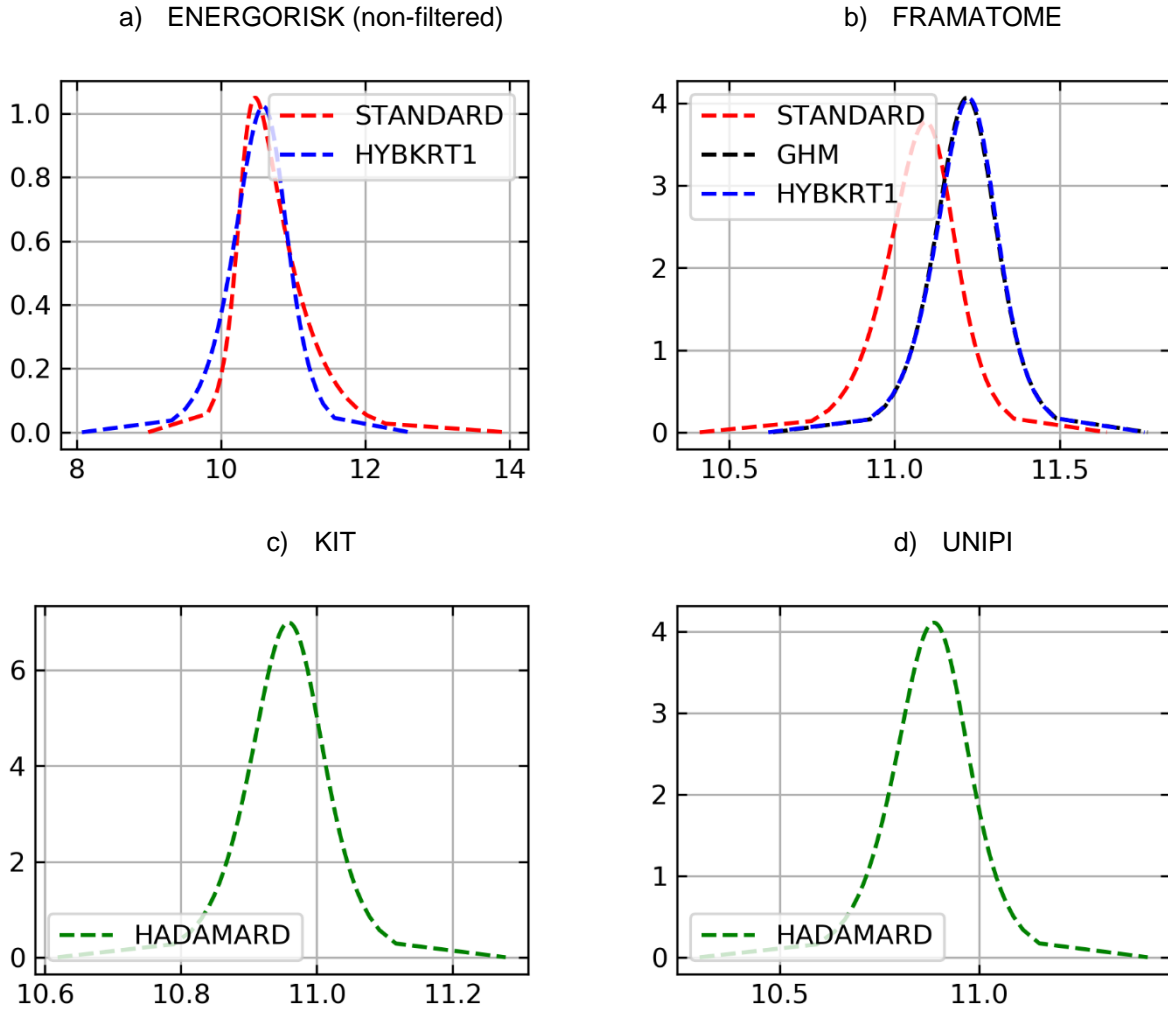


Figure 16 : Non normalized PDF associated to the fitted Metalog distribution for the different ensembles and partners

4.2.4. Time evolution of the hot leg 1 temperature

The same data processing as $\Delta T_{HL,1}$ is applied for each instant of the time evolving signal $T_{HL,1}(t)$: statistical moments are calculated up to order 4 which are then used to fit a four term Metalog distribution. If the resulting distribution is infeasible, a three term Metalog is fitted. This distribution is then used to evaluate the quantiles $Q_{2.5\%}$, $Q_{5\%}$, $Q_{50\%}$, $Q_{95\%}$ and $Q_{97.5\%}$. It should be noted that very few instants in the time evolution yielded infeasible 4-term Metalog (<1%).

The time evolution of the mean value and quantiles for the different ensembles is given for ENERGORISK on Figure 17 for filtered and non-filtered signals, and on Figure 18 for the other partners. The effect of filtering can be seen on Figure 17 where the quantiles $Q_{2.5\%}$, $Q_{5\%}$ show less fluctuations on filtered signals for the Σ_{STD} ensemble. Its effect is less visible for the Σ_{KRT1} ensemble where the individual weight of the fluctuating signals is less important due to higher number of samples. When looking at the results of the different partners, it can be noticed that most of the experimental data is bounded by the quantiles $Q_{2.5\%}$ and $Q_{97.5\%}$. In addition, the experimental uncertainty is not indicated on the figures, but it should be reminded that the experimental uncertainty is around $\pm 2^\circ C$.

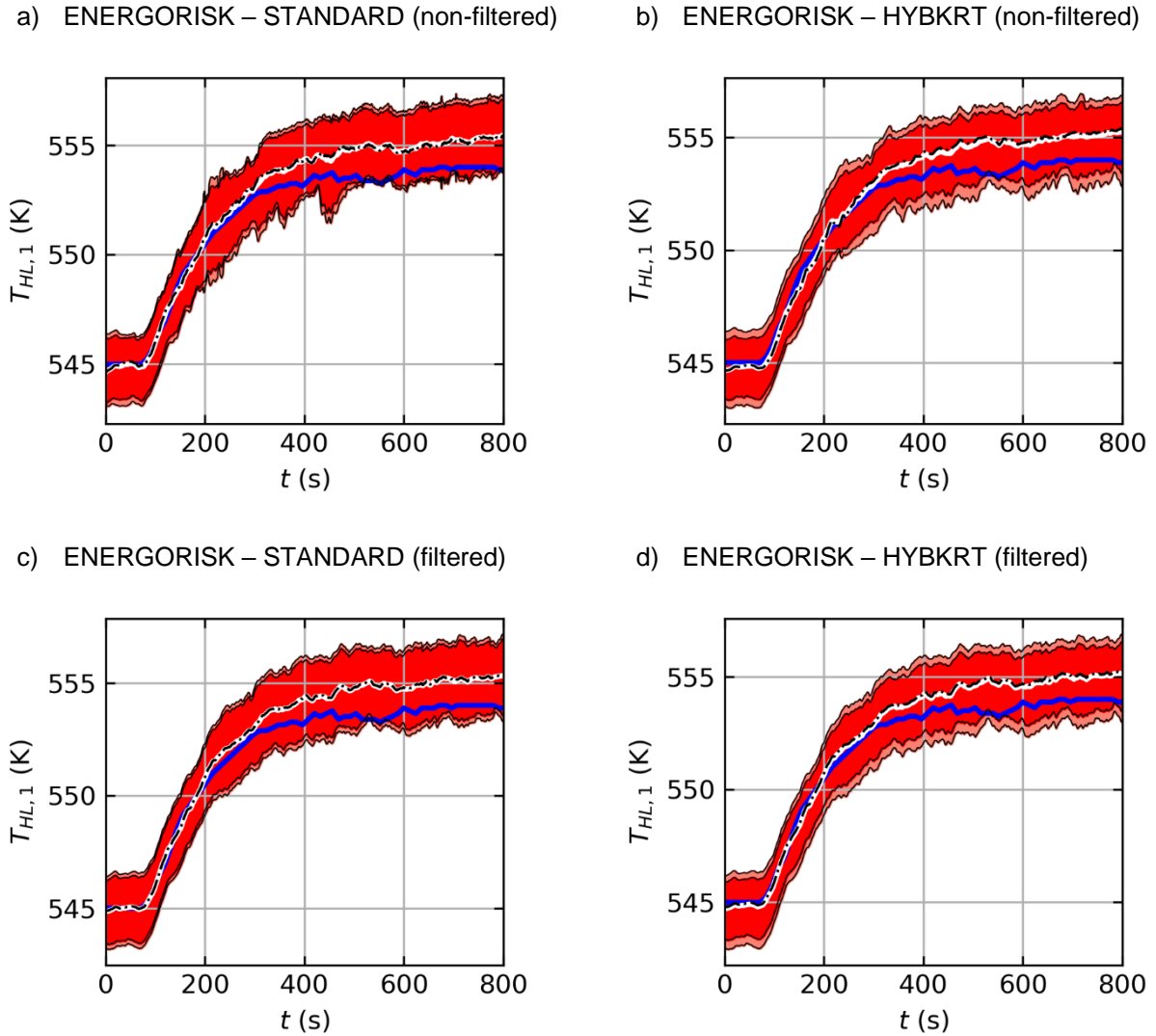
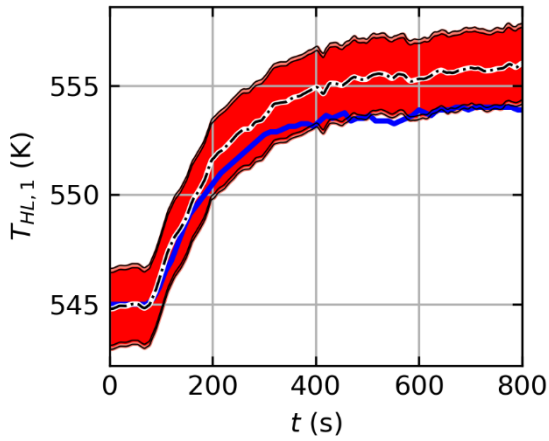


Figure 17 : Time evolution of $T_{HL,1}$ – Mean value (dotted black), median value (solid white), $Q_{5\%}$, $Q_{95\%}$ (filled red), $Q_{2.5\%}$, $Q_{97.5\%}$ (filled salmon) and experimental value (solid blue)

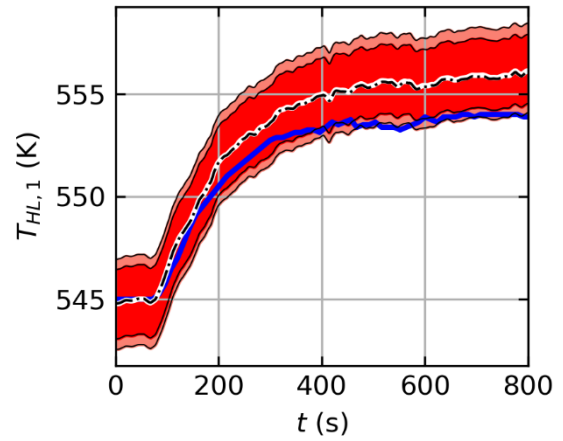
Regarding the sensitivity of the results to the ensemble, different remarks can be made. First, it can be noticed that the distribution's skewness is only noticeable on UNIPi- Σ_{GHM} and ENERGORISK- Σ_{KRT1} . Nevertheless, this impact is still negligible in front of the variance of the signal. In addition, it can be noticed that enforcing the fourth order moment (with Σ_{GHM} or Σ_{KRT} ensembles) impacts the quantiles as the tails of the distributions seem more spread out inducing larger confidence intervals. Finally, the additional information provided by the mixed moments of order 4 with Σ_{KRT1} ensemble is not visible in this case.

The intersections and union of the time evolution of the interval $[Q_{2.5\%}, Q_{97.5\%}]$ between partners are given on Figure 19. The intervals given are ENERGORISK evaluations over Σ_{KRT2} , UNIPi evaluations over Σ_{GHM} , FRAMATOME over Σ_{GHM} and KIT over Σ_{HAD} . It is visible that the experimental measurements are within the $[Q_{2.5\%}, Q_{97.5\%}]$ interval provided.

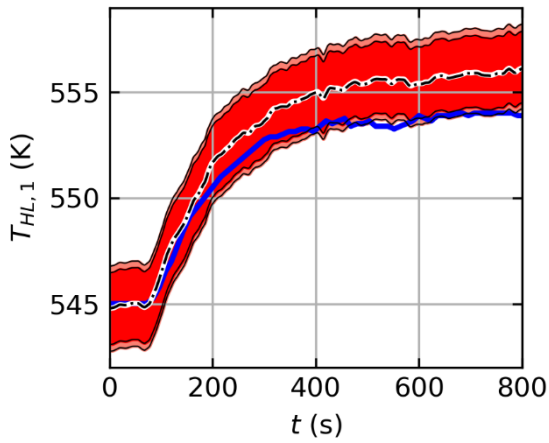
a) FRAMATOME – STANDARD



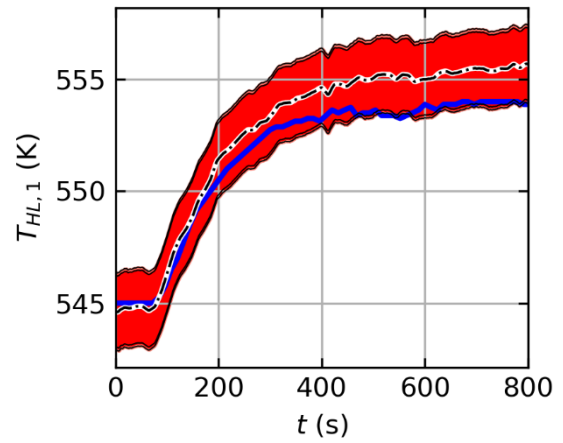
b) FRAMATOME – GHM



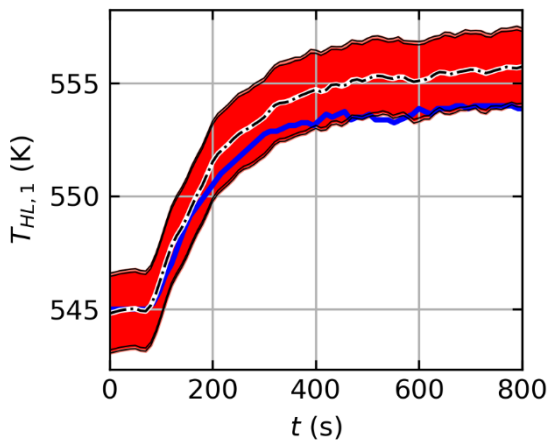
c) FRAMATOME – HYBKRT



d) KIT – HADAMARD



e) UNIPI – HADAMARD



f) UNIPI – GHM

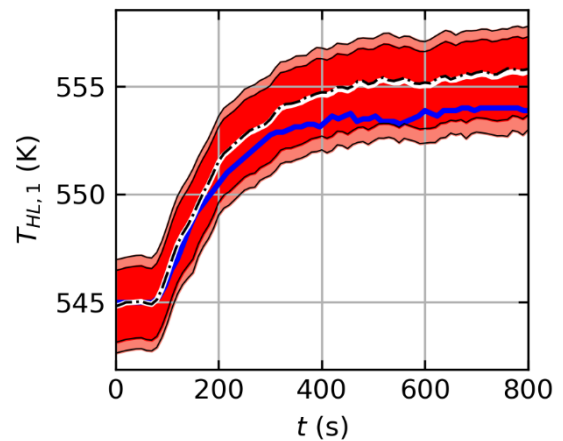


Figure 18: Time evolution of $T_{HL,1}$ – Mean value (dotted black), median value (solid white), $Q_{5\%}$, $Q_{95\%}$ (filled red), $Q_{2.5\%}$, $Q_{97.5\%}$ (filled salmon) and experimental value (solid blue)

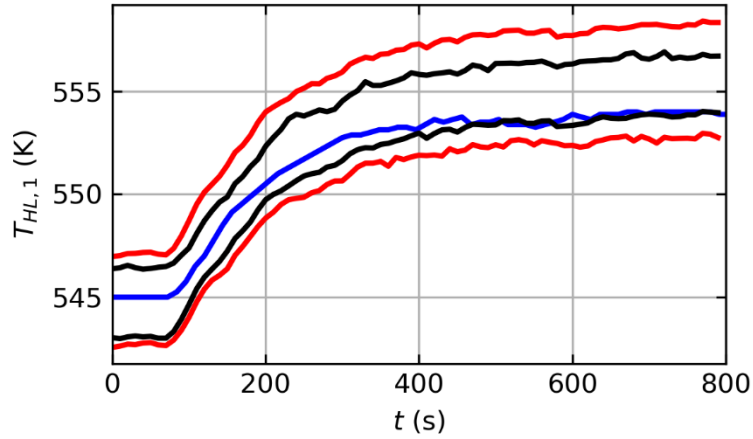


Figure 19: Intersection and union of the interval $[Q_{2.5\%}, Q_{97.5\%}]$ over the evaluations. Union of the intervals between partners/ensembles (red), intersection of intervals (black), experimental values (blue)

4.2.5. Sensitivity analysis

Correlations between the output $Y = \Delta T_{HL,1}$ and the inputs X_1, X_2, X_3, X_4 which are respectively the flow rate in cold leg 1, the temperature in cold leg 2, the temperature in cold leg 1 and the total power in the core, are calculated and given on Table 8. An important correlation of Y to X_1 is observed for most of the models and ensembles. The evolution of Y with the amplitude of X_1 is given on Figure 20. For FRAMATOME, UNIPi and KIT, a clear correlation between X_1 and Y can be seen on this figure. However, one of the set of inputs from Σ_{GHM} yields a significantly different output affecting the evaluated correlation. The evaluation of Y with ENERGORISK model shows more results variability with no clear correlations.

Table 8 :Correlation of the inputs with the output $Y = \Delta T_{HL,1}$

Partner	Ensemble	$corr(Y, X_1)$	$corr(Y, X_2)$	$corr(Y, X_3)$	$corr(Y, X_4)$
ENERG	STD	-0.19	-0.02	0.15	-0.60
	HYBKRT2	-0.36	-0.21	0.06	-0.19
FRAMA	STD	0.99	-0.07	-0.01	-0.05
	GHM	0.95	-0.29	0.00	-0.01
	HYBKRT1	0.95	-0.31	0.00	-0.05
KIT	HADAMARD	0.95	-0.06	0.12	-0.13
UNIPi	HADAMARD	0.97	0.09	-0.19	-0.01
	GHM	0.02	0.41	0.26	0.35

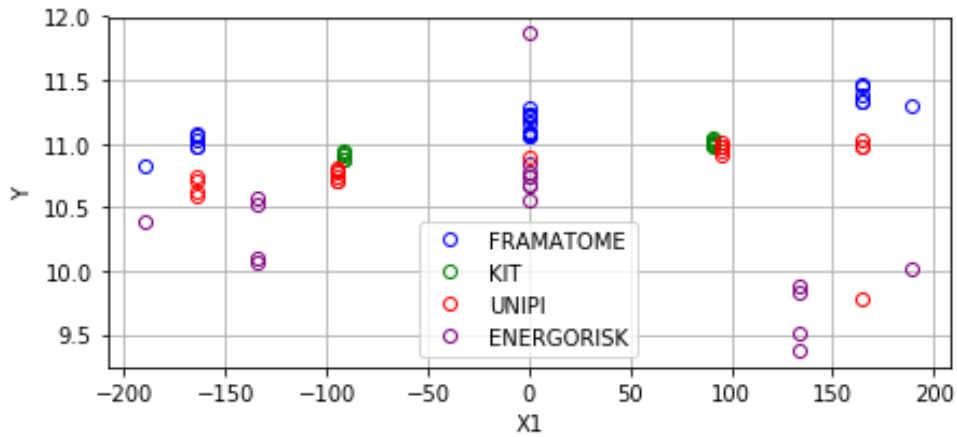


Figure 20: Scatter plot for $Y = \Delta T_{HL,1}$ as a function of X_1

Scatter plots on which the evolution of Y with respect to X_i, X_j are given for ENERGORISK, FRAMATOME, KIT and UNIFI models respectively on Figure 21, Figure 22, Figure 23 and Figure 24. The amplitude of Y is indicated by a colormap. Having combined effect of parameters can be seen on these scatter plots when a different behavior is seen in principal directions and the diagonals. If we first look at FRAMATOME model on Figure 22, combined effects of X_1 and X_2 on Y can be seen. For instance, the impact of the increase of X_1 and decrease of X_2 on the amplitude of Y is less important when they are taken separately rather than simultaneously. This behavior can also be seen for KIT model on Figure 23. For UNIFI combined effects are much more present between X_2 and X_3 . The data from ENERGORISK given on Figure 21 shows more noise which hides correlations. However, we can still observe that high values of flowrate yielded significantly lower results which seem to show a different behavior of CFD on that range than for lower values of flowrates.

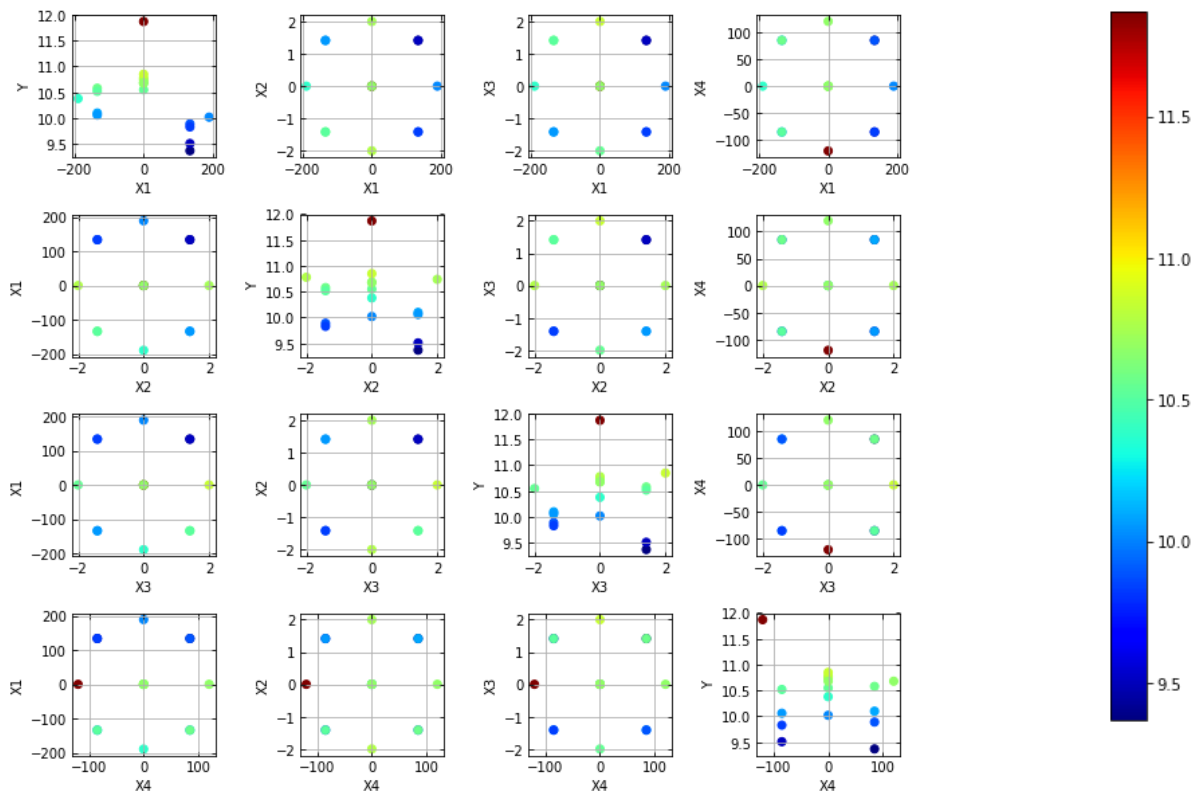


Figure 21 : Evolution of $\Delta T_{HL,1}$ on scatter plots X_i, X_j – ENERGORISK – Amplitude of Y is given with a jet colormap

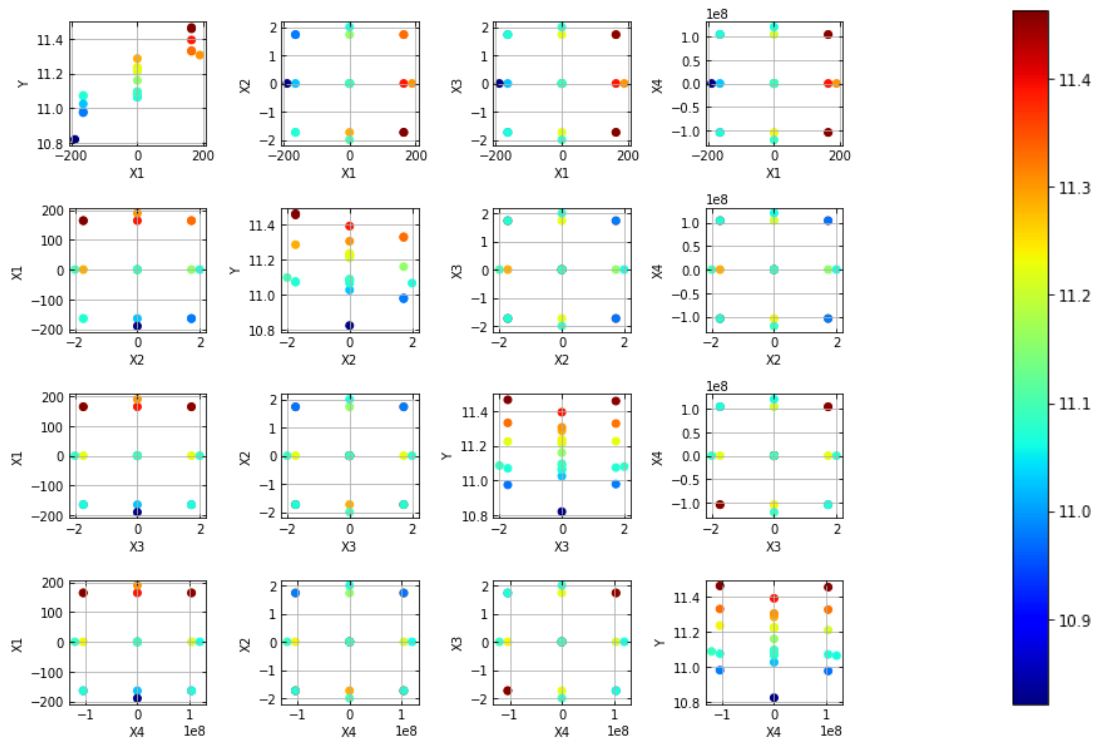


Figure 22 : Evolution of $\Delta T_{HL,1}$ on scatter plots X_i, X_j – FRAMATOME – Amplitude of Y is given with a jet colormap

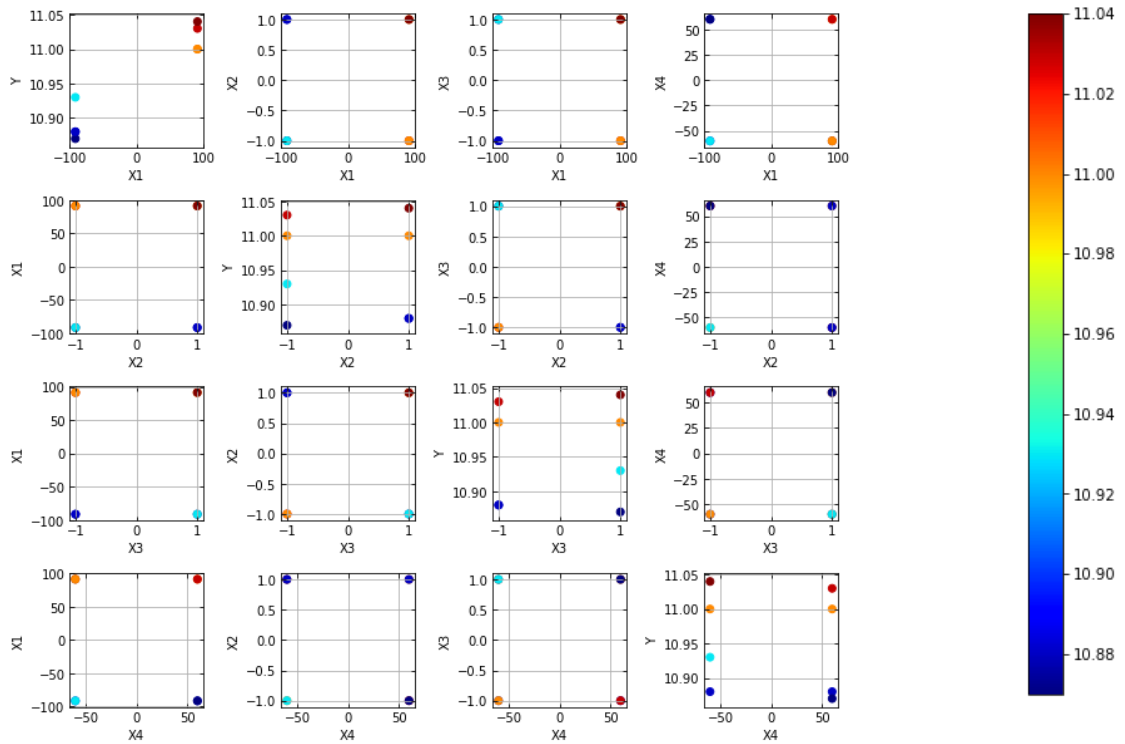


Figure 23: Evolution of $\Delta T_{HL,1}$ on scatter plots X_i, X_j – KIT – Amplitude of Y is given with a jet colormap

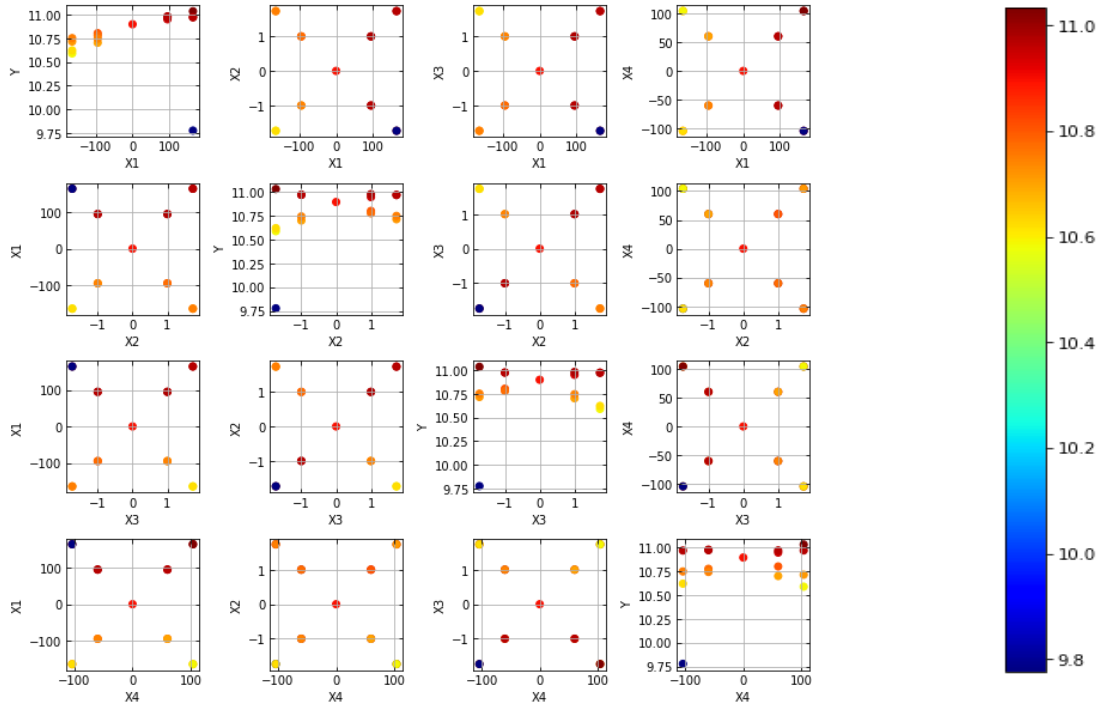


Figure 24 : Evolution of $\Delta T_{HL,1}$ on scatter plots X_i, X_j – UNIPI – Amplitude of Y is given with a jet colormap

4.2.6. Conclusion on U_{inputs}

A realization $\delta_{U_{inputs}}$ of the random variable (RV) U_{inputs} can be written:

$$\delta_{U_{inputs}} = f_{CFD}(\mu_X) - \delta_{f_{CFD}(\delta_X)}$$

The quantity $f_{CFD}(\mu_X)$ is a constant, thus, the statistical moments of order $m \geq 2$ of U_{inputs} are the same as $T_{HL,1}(t)$ and $\Delta T_{HL,1}$ (according to which uncertainty we try to assess). However, the mean values are shifted to a value reflecting the bias of the CFD results when considering or not the inputs uncertainties.

$$\mu_{U_{inputs}} = f_{CFD}(\mu_X) - \mu_{f_{CFD}(X)}$$

The mean value and standard deviation of U_{inputs} are given on Table 9 and plotted on Figure 25.

Table 9 : Mean and standard deviation of U_{inputs} for the calculation of $Y = \Delta T_{HL,1}$

Partner	Ensemble	$\mu_{U_{inputs}}$	$\sigma_{U_{inputs}}$
ENERGORISK	STD	-5.4e-2°C	0.50°C
	HYBKRT2	0.16°C	0.45°C
	STD (filtered)	0.28°C	0.09°C
	HYBKRT2 (filtered)	0.30°C	0.08°C
FRAMATOME	STD	0.15°C	0.12°C
	GHM	4.4e-3°C	0.11°C
	HYBKRT1	4.3e-3°C	0.11°C
KIT	HADAMARD	4.1e-3 °C	6.7e-2°C
UNIPI	HADAMARD	3.4e-2°C	0.11°C
	GHM	7.3e-2°C	0.24°C

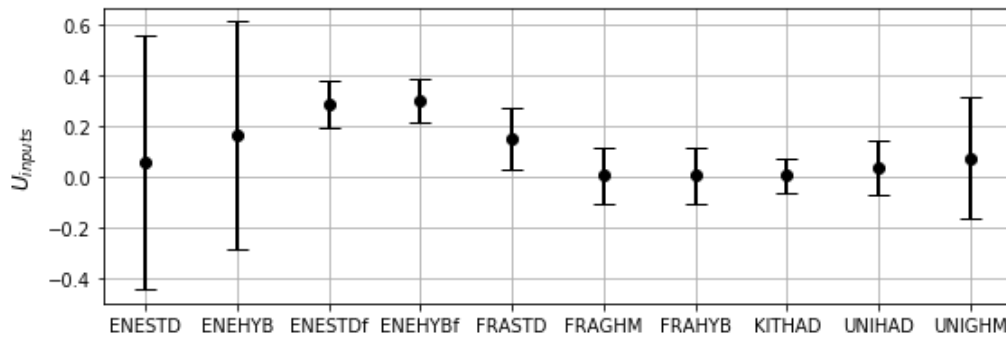


Figure 25: mean value (point) and standard deviation (error bars) evaluated for the different partners and ensemble.

In the general case, the amplitude of the bias induced by the uncertain parameters is lower than the variability induced by the inputs except for FRAMATOME evaluation on Σ_{STD} where both are of the same amplitude. The results obtained with FRAMATOME, UNIFI and KIT models which showed small time fluctuations should be considered $\pm 0.5^\circ$. In comparison, ENERGORISK results for $\Delta T_{HL,1}$ show more important fluctuations which is consistent with the results obtained on the mixing coefficient C_1 in §4.1. In fact, the temperature in hot leg 1 reflects the mixing in the core, thus, it is normal to have more variance on temperature for this model as more variance has been noticed on the mixing in the core. The results can be considered $\pm 1^\circ C$. When the filtering is applied, the bias increases significantly however the standard deviation is divided by 5.

The sensitivity of the results to the flowrate variations are visible for all models. Correlations between $\Delta T_{HL,1}$ and $Q_{CL,1}$ were found for UNIFI, KIT and FRAMATOME models. It has also been noticed that the values of correlations can be affected by individual points presenting important discrepancy compared to others as the total number of evaluations is small. Concerning the sensitivity of $\Delta T_{HL,1}$, some models showed a combined effect of parameters which increased the fluctuations when compared to separate fluctuations of inputs.

Regarding the use of DS for uncertainty propagation, the importance of the choice of the DS ensemble has been highlighted. In fact, different behaviors of the CFD models were observed whether the inputs were varying simultaneously or separately. Thus, ensembles enabling the evaluation of CFD for combinations of parameters should be preferred than separate variations between parameters. The ensembles Σ_{KRT1} and Σ_{KRT2} seems to be a good choice for propagating as it combines separate and simultaneous variations of parameters. In addition, the results obtained with different ensembles and the fit of the Metalog distribution showed the impact of enforcing the fourth order moment on the evaluation of quantiles which were more spread out when kurtosis was correctly enforced when compared to more basic ensembles. This impact is nevertheless limited to the kurtosis of the output and is negligible for instance on the variance of the output. In addition, the gain of enforcing mixed moment of order 4 is not obvious when comparing Σ_{KRT} ensembles to Σ_{GHM} which yield similar quantiles.

In conclusion, the DS method of propagation enabled the assessment of quantiles and statistical moments of U_{inputs} . Also, the consistency of the statistical moments obtained with the different ensembles is representative of the model response: if the CFD model sensitivity to the inputs is strong and chaotic, the uncertainty will be higher with amplitudes of the order of magnitude of the time fluctuations of the signal. Also, the results will be more dependent to the chosen ensemble as it has been seen on ENERGORISK outputs and correlation to parameters will be unclear. In comparison, if the CFD model is less noisy, the variance is lower and correlation to the parameters is noticeable. It should still be noted that the quantiles obtained from the different partners are consistent with good agreement between models, ensembles, and experimental data.

4.3. FA Temperature average

4.3.1. Overview of the results

Example of 2D views of mass flow averaged outlet temperature for each fuel assembly i at $t = t_0 + 800s$ $T_{FA,o}(i)$ are given for the different CFD models on Figure 26. Differences are visible on these examples on the amplitude of the temperature and the mixing in the core.

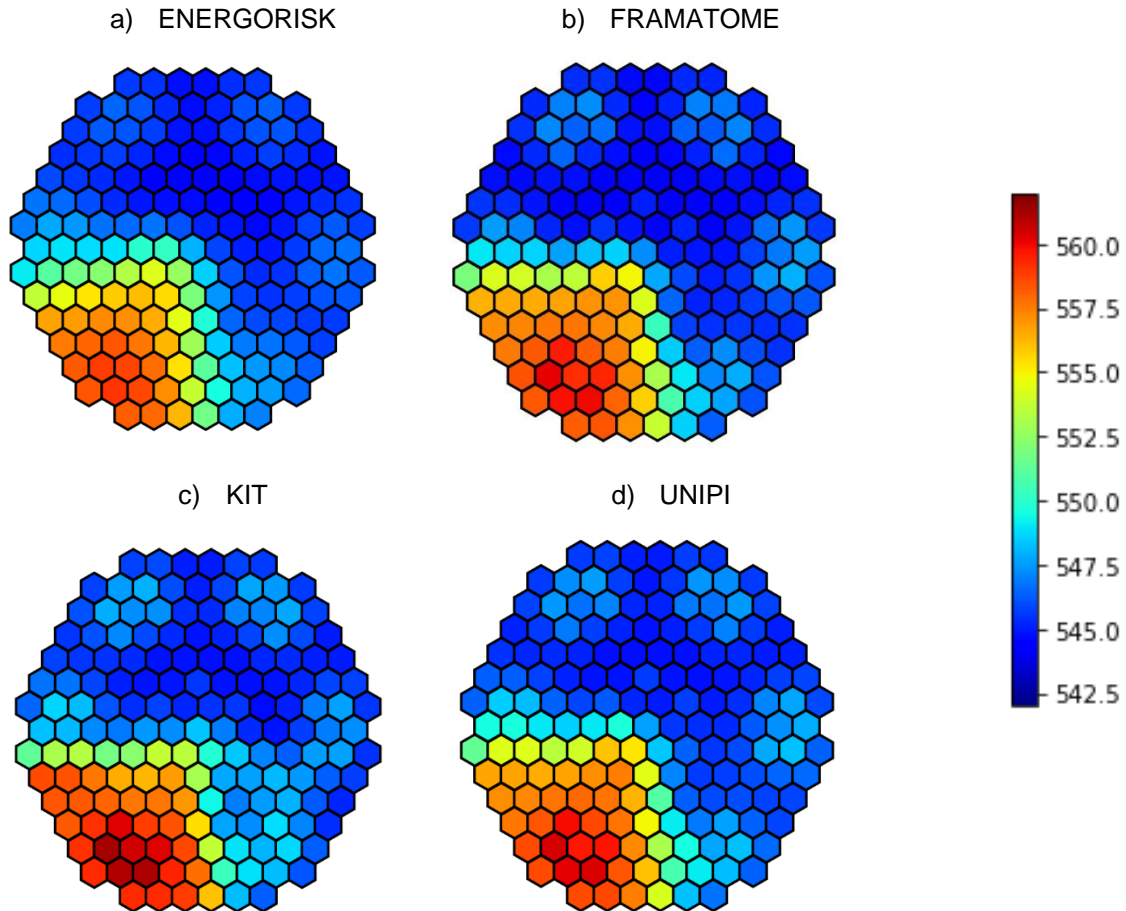
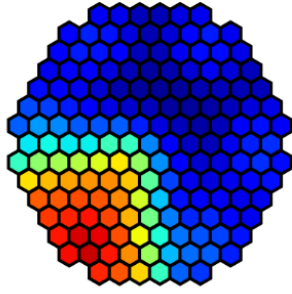


Figure 26 : Temperature $T_{FA,o}(i)$ (K) at $t = t_0 + 800s$ – Examples for the different partners

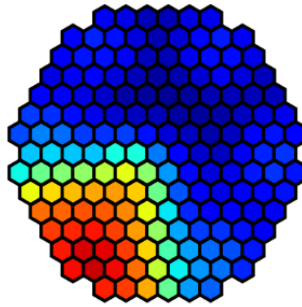
The mean values and standard deviation of $T_{FA,o}(i)$ evaluated from the different ensembles are given respectively on Figure 27 and Figure 28. First it can be noticed that the topology is similar between all partners and are representative of the mixing map $C_1(i)$ described in §4.1. In terms of amplitude, ENERGORISK model yields lower values of the temperature maximum due to higher mixing, followed by KIT, UNUPI and FRAMATOME evaluations. This result is coherent with the mixing coefficient values obtained for the different models in §4.1.

Regarding the standard deviation, similar amplitudes are observed for all partners except for ENERGORISK which outputs presented more fluctuations. This might be due to the time fluctuations that were also observed when studying the hot leg 1 temperature. These fluctuations seem to be related to the mixing in the core which shows more variability than for other models. In fact, the topology of the standard deviation distribution in the core shows important values at junctions between the affected zone of the different cold legs as it can be seen for the mixing coefficient on Figure 7a and Figure 7b. In comparison, the topology of the standard deviation obtained from the other partners models presents symmetries between the mixing zones 1 and 2 corresponding to areas affected by cold legs 1 and 2 and are more consistent from a computation to another.

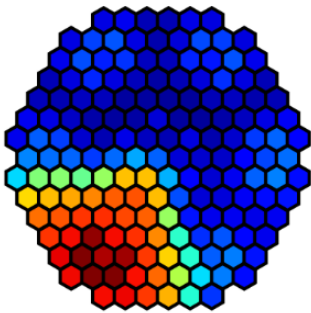
a) ENERGORISK - Σ_{STD}



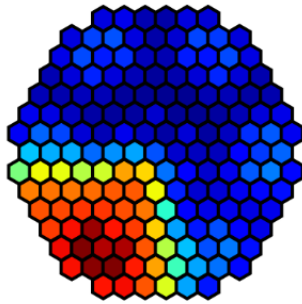
b) ENERGORISK - Σ_{KRT1}



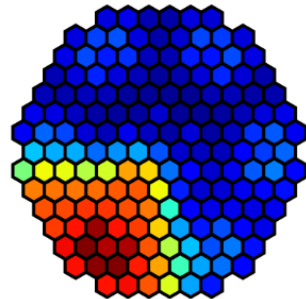
c) FRAMATOME - Σ_{STD}



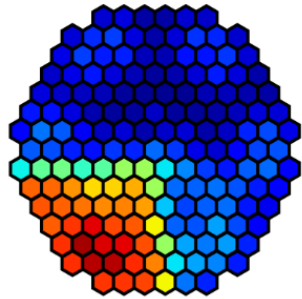
d) FRAMATOME - Σ_{GHM}



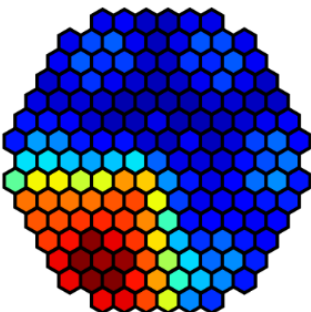
e) FRAMATOME - Σ_{KRT2}



f) KIT - Σ_{HAD}



g) UNIPI - Σ_{GHM}



h) UNIPI - Σ_{HAD}

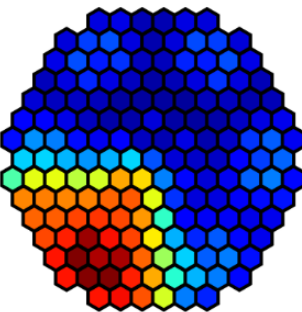


Figure 27 : Mean value of $T_{FA,o}(i)$ (K) at $t = t_0 + 800s$ – Results for the different partners/ensembles

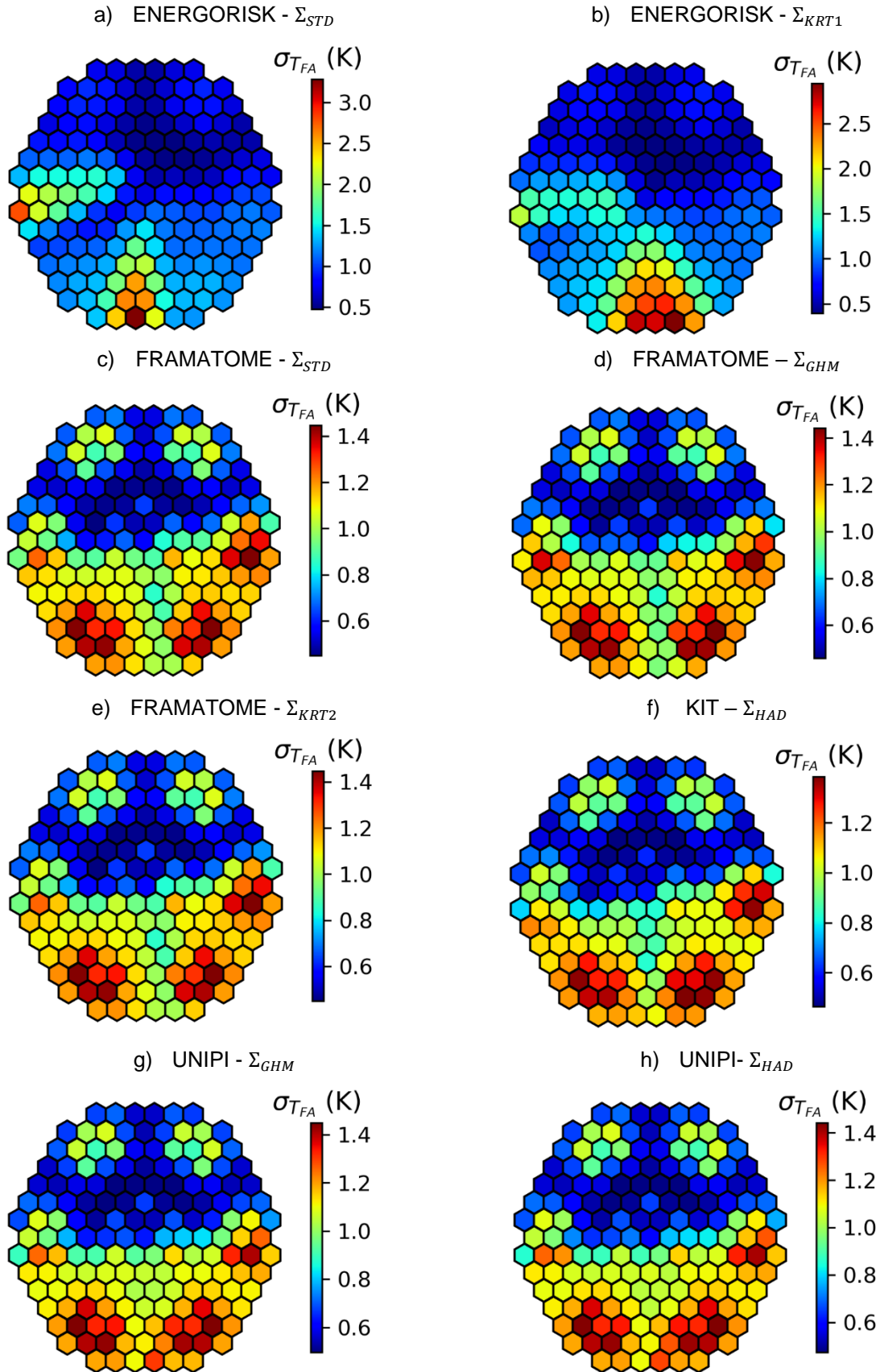


Figure 28 : Standard deviation of $T_{FA,0}(i)$ (K) at $t = t_0 + 800s$ – Results for the different partners/ensembles

If we investigate some specific computations, different topology of spatial fluctuations when compared to the mean calculation can be seen. Examples are given on Figure 29. The topology of the fields is a good indicator of the impact of inputs variations in the core. Increasing the temperature in cold leg 2 induces an increase of temperature near cold leg 2 zone of influence in the core (see Figure 29b). The topology of this fluctuations shows important similarities to the mixing map $C_2(i)$, which reflects the way the temperature coming from the cold leg 2 is mixed in the core. Increasing the total power induces an increase of temperature in specific region of the core related to the power and mass flow distribution (see Figure 29a), while combining inputs variations seem to combine the spatial variations (see Figure 29d). Nevertheless, it should be noted that for some models, the response to inputs variations were more chaotic due to the fluctuations of mixing in the core.

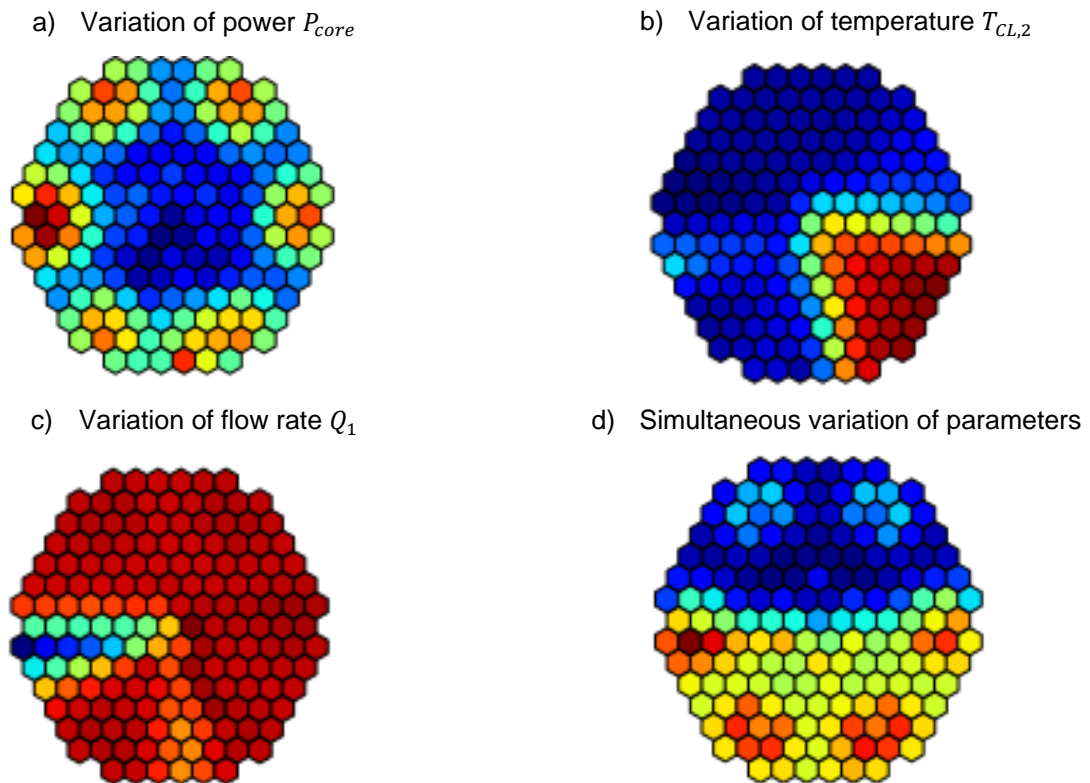


Figure 29 : Example of 2D variation field $T_{FA,o}(i, X) - T_{FA,o}(i, \mu_X)$ for different variations of inputs X .

4.3.2. Sensitivity analysis

The sensitivity of $T_{FA,o}(i)$ to the different inputs is studied in this section. This study is done by applying the POD described in §2.2 to find spatial correlation between the variations of the 2D fields with the modification of the inputs X_1, X_2, X_3 and X_4 . In this section we first analyse separately the results of the different partners, then a comparison of the models' sensitivity will be done.

4.3.2.1. ENERGORISK

Two ensembles were used to evaluate the results with this model: Σ_{STD} (8 available snapshots) and Σ_{KRT1} (17 available snapshots). These two different groups of snapshots were used to evaluate the POD modes and eigenvalues. The relative information content (RIC) is given as a function of the POD truncation on Figure 30. The four first modes calculated for the two ensembles are given on Figure 31 and Figure 32.

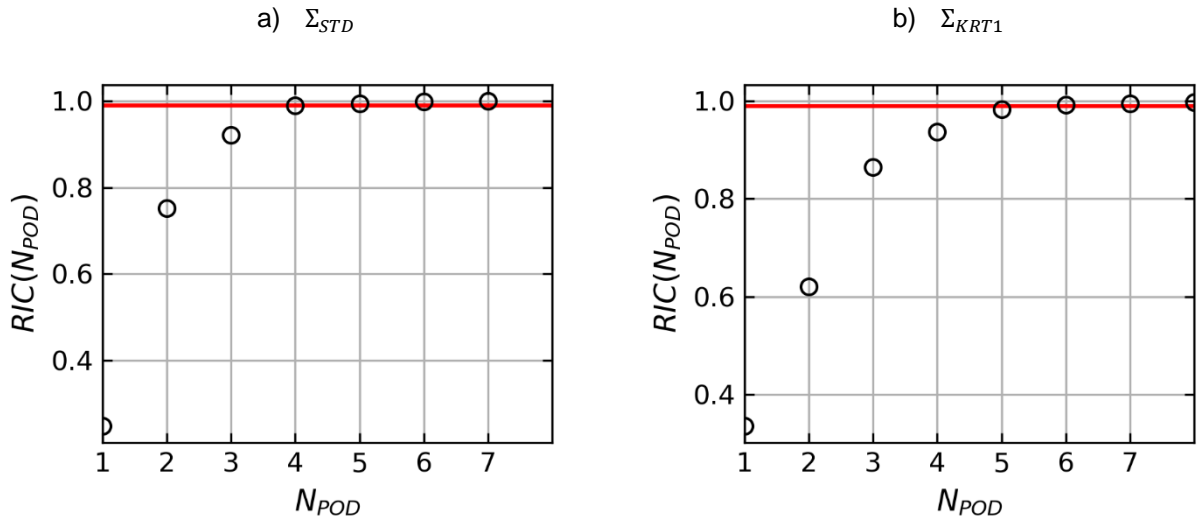


Figure 30 : RIC as a function of the number of modes for the POD applied to the snapshots of the different ensembles evaluated by ENERGORISK.

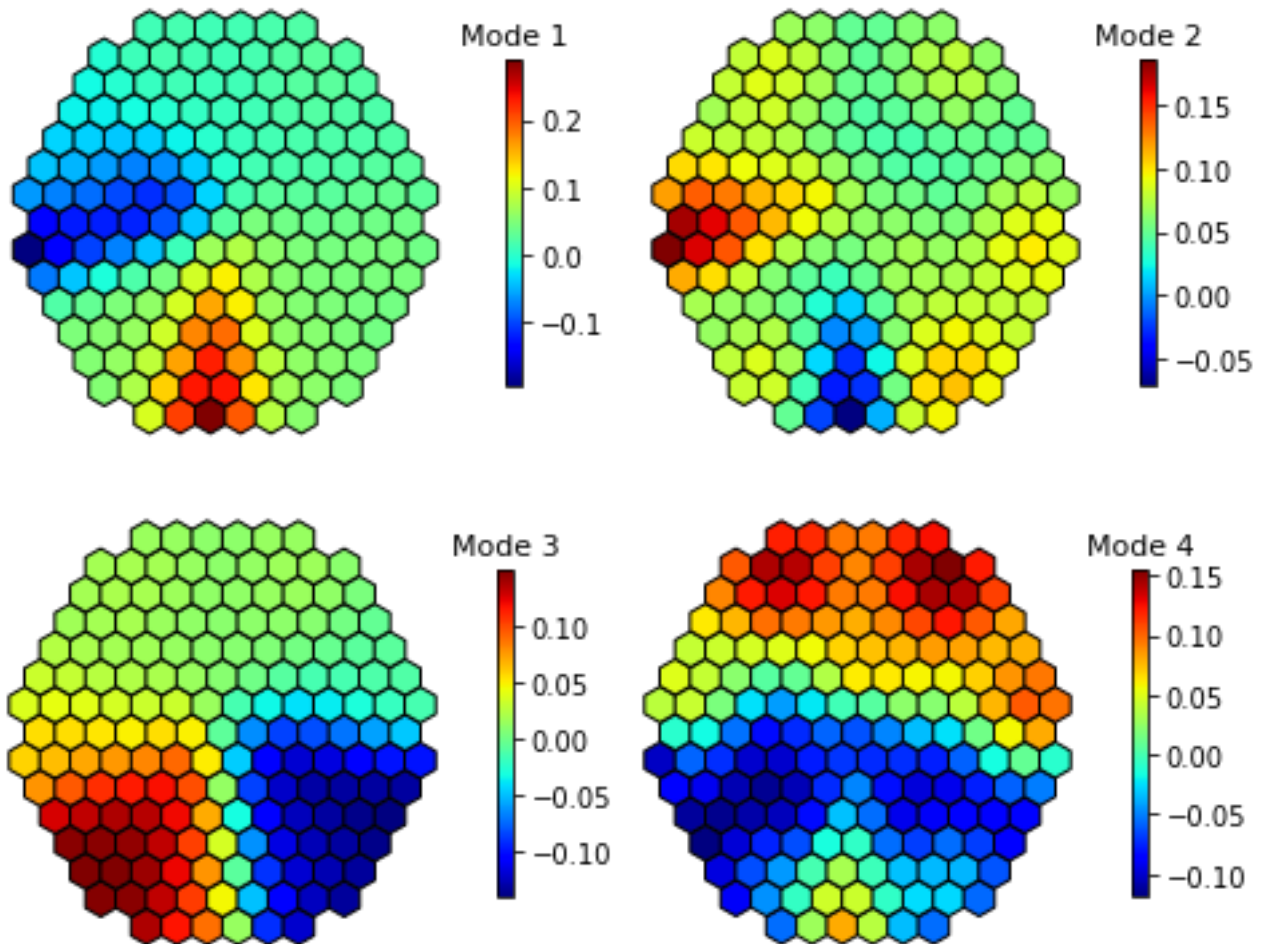


Figure 31 : 4 first modes calculated from the snapshots of ensemble Σ_{STD} .

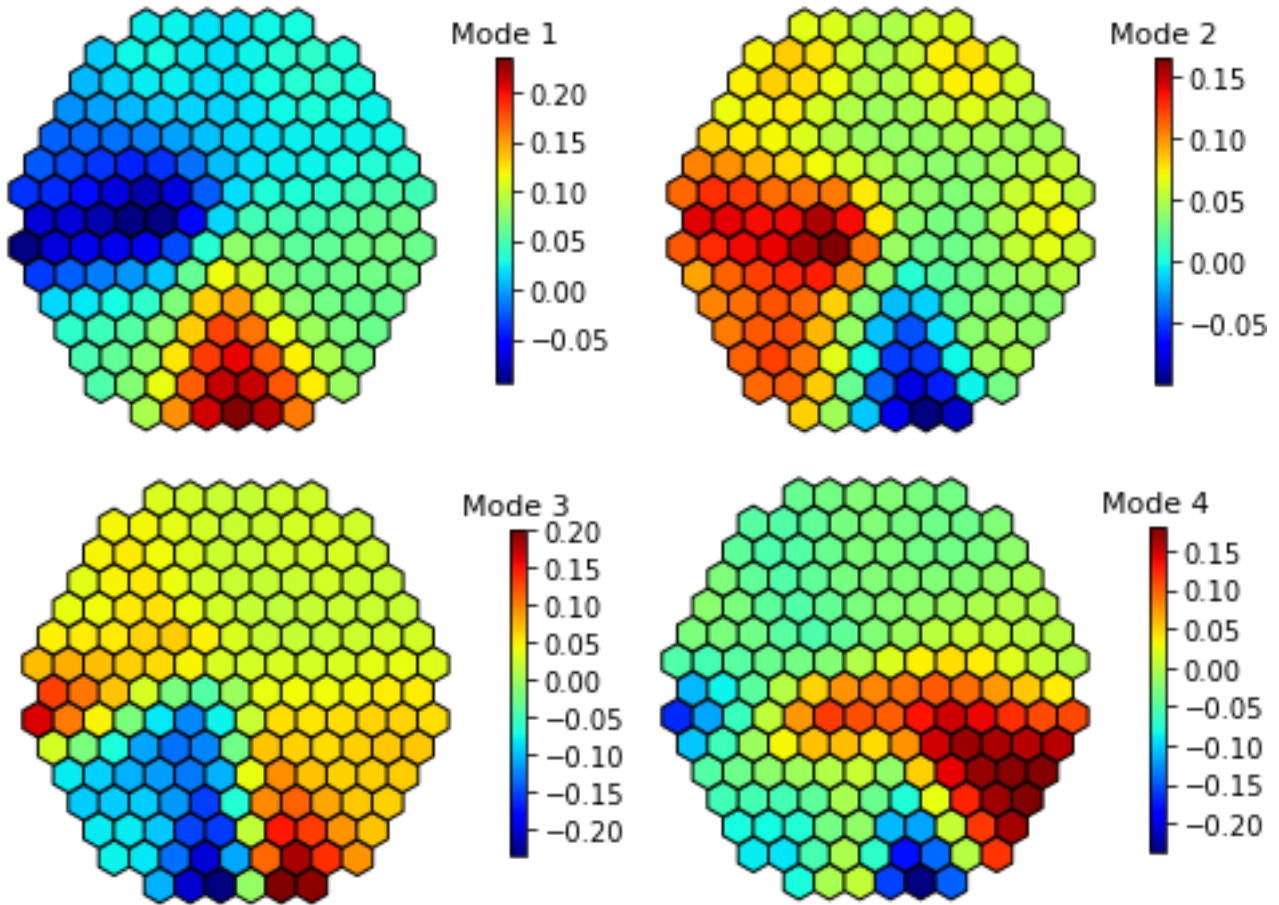


Figure 32 : 4 first modes calculated from the snapshots of ensemble Σ_{KRT} .

Different remarks can be done on the POD obtained from the different ensembles:

- The RIC number given for the two ensembles on Figure 30 indicates that 4 to 5 modes are required to have $RIC(N_{POD}) > 0.99$. Also, the snapshots from the Σ_{KRT1} ensemble add information not provided by the Σ_{STD} ensemble, requiring additional modes for the same level of representation.
- The modes obtained seem to be mainly related to mixing for both ensembles. In fact, it is visible on Figure 31 and Figure 32 that the mode 1 of both POD shows important similarities to mode 1 obtained on C_1 in §4.1.2. Mode 2 seems to be the symmetric of mode 1 and differences between the two ensembles start at mode 3. The variations of the mixing in the core are especially important for this model, which indirectly impacts the mixing of temperature between cold leg 1 and 2 affecting $T_{FA,o}(i)$.
- For Σ_{STD} , the mode 3 is closely related to the mixing map in the core between leg 1 and leg 2. This mode reflects the way temperatures in cold leg 1 and 2 variations are propagated through the core. For Σ_{KRT1} , the resemblance is less obvious even though important values of the mode can be seen in the zone corresponding to high values of $C_1(i)$.
- When changing the range of the colormap for mode 2, structures related to the power distribution and mass flow are visible as it can be seen on Figure 33. In fact, lobes are visible at different locations near zones similar to the one visible on Figure 29a. Nevertheless, the low amplitude of the mode values on these one when compared to values on the lower left of the core indicate the relative low importance of these fluctuations compared to the ones related to mixing on this model.

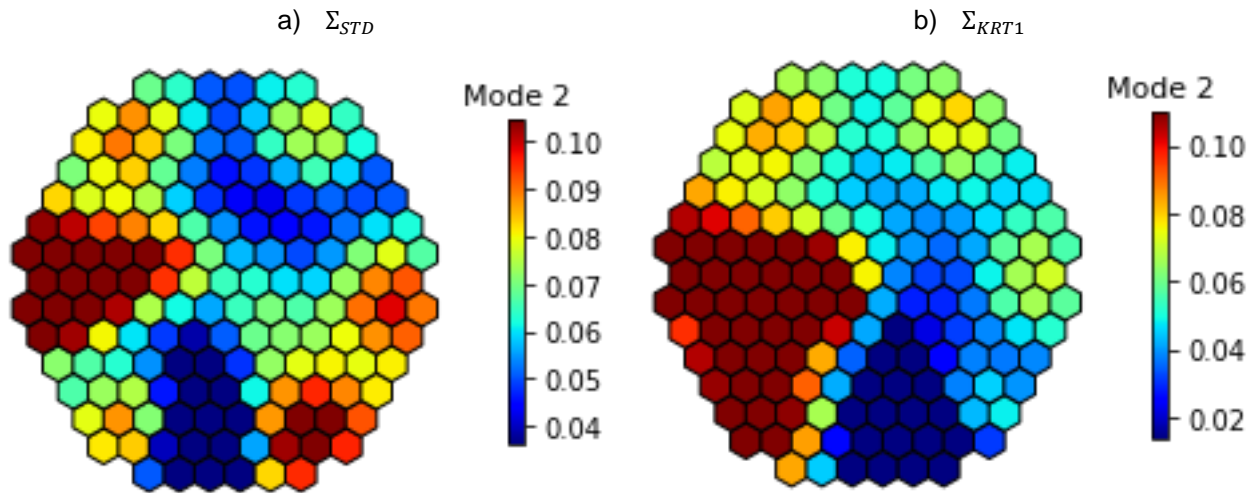


Figure 33 : Zoom on mode 2 from the two ensembles evaluated with ENERGORISK model

On this specific model, correlations are hard to see as the output was sensitive to any modification of input parameters, they will thus not be shown in this paragraph.

4.3.2.2. FRAMATOME

Three ensembles were used to evaluate the results with this model. These three different ensembles of snapshots were used to evaluate the POD modes and eigenvalues. The relative information content (RIC) is given as a function of the POD truncation on Figure 34. The four first modes calculated for the three ensembles are given on Figure 35 Figure 36 and Figure 37. Different remarks can be done on the results. For the three ensembles, 4 modes are sufficient to obtain $RIC(i) \geq 0.99$. Also, the four modes obtained for the three ensembles show strong similarities with differences observed only for mode 3 where opposite sign is found for Σ_{STD} ensemble when compared to Σ_{GHM} and Σ_{KRT2} . If we investigate the structure of the different modes, it is visible that mode 1 and 3 show symmetric topology between the left and right side of the core with amplitudes different between the upper and lower side of the core. Asymmetry is provided with modes 2 and 4.

The correlation of components a_1, a_2, a_3 and a_4 of the POD computed for all snapshots on Σ_{KRT2} ensemble to the inputs X_1, X_2, X_3 and X_4 are indicated on Table 10. Small differences are observed between the correlations evaluated from different ensembles.

- When the mode presents symmetry between leg 1 and 2, the correlation between the component and the inlet temperatures in cold leg 1 and 2 are of the same sign. On the other side, for the antisymmetric mode 2, the sign of the correlation $corr(a_2, X_2)$ and $corr(a_2, X_3)$ are of opposite signs.
- The power P_{core} impacts the value of components a_1 and a_3 . The related modes both presents the lobes that can be seen on Figure 29a. In addition, the opposite sign found for mode 3 with Σ_{STD} is counterbalanced by the negative sign of the components when compared to the other ensembles.
- The flowrate has a limited impact on $T_{FA,o}(i)$, expressed by the mode 4 which only impacts a small proportion of the core fuel assemblies located at the junction of the mixing zone 1 and 4. In terms of amplitude, the low number of assemblies are nevertheless affected with variations going up to $0.6^\circ C$.

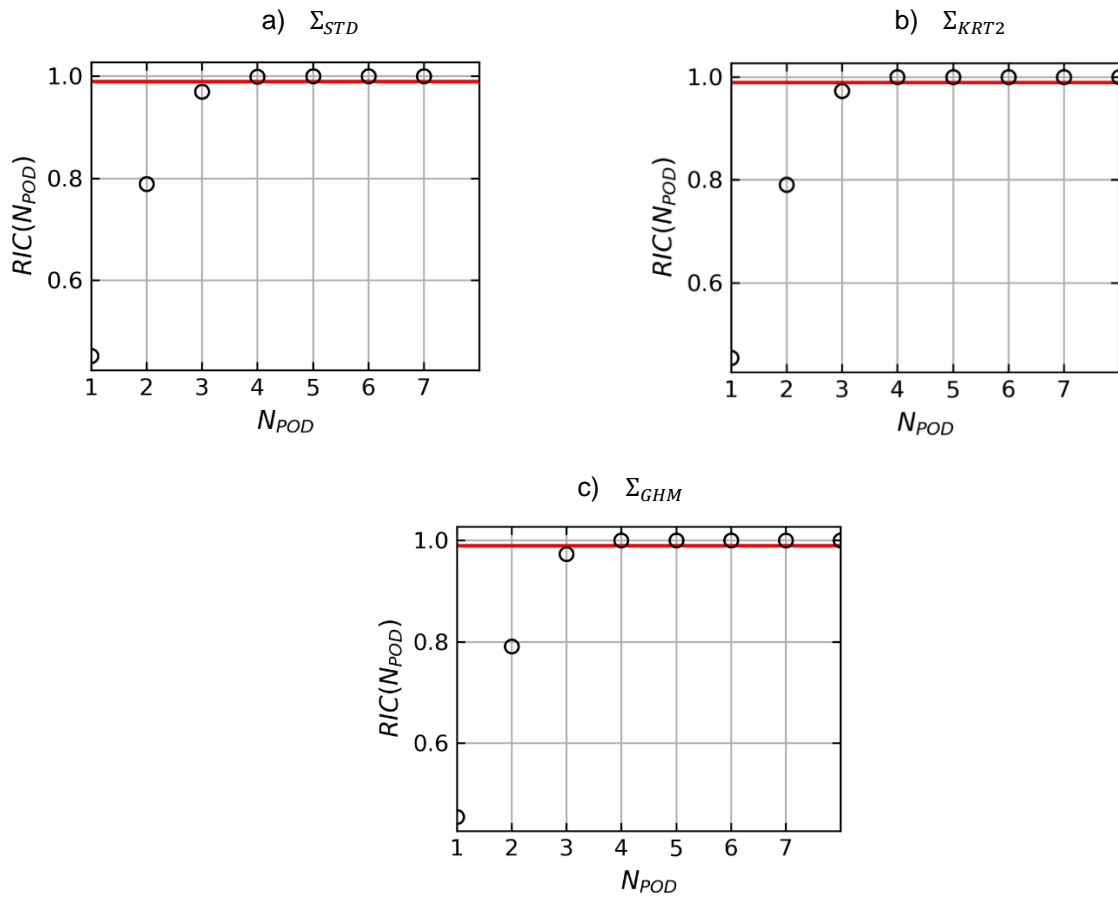


Figure 34 : RIC as a function of the number of modes for the POD applied to the snapshots of the different ensembles.

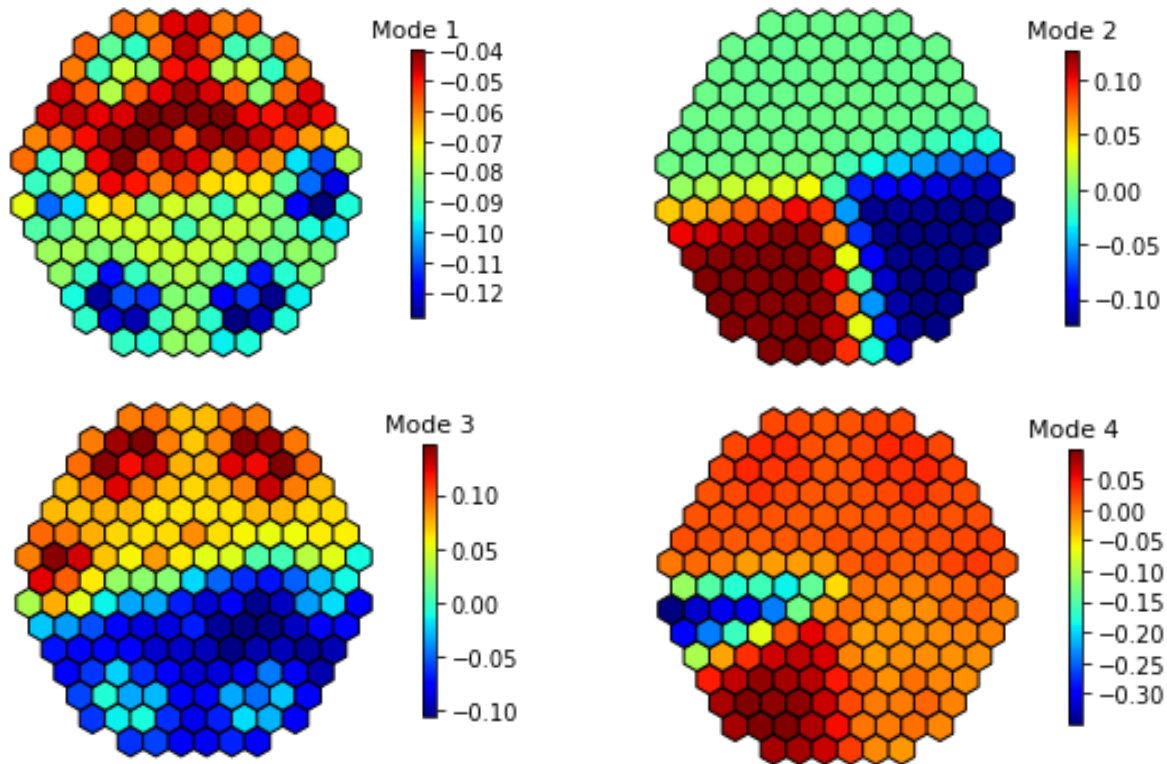


Figure 35: 4 first modes calculated from the snapshots of ensemble Σ_{STD} with FRAMATOME model.

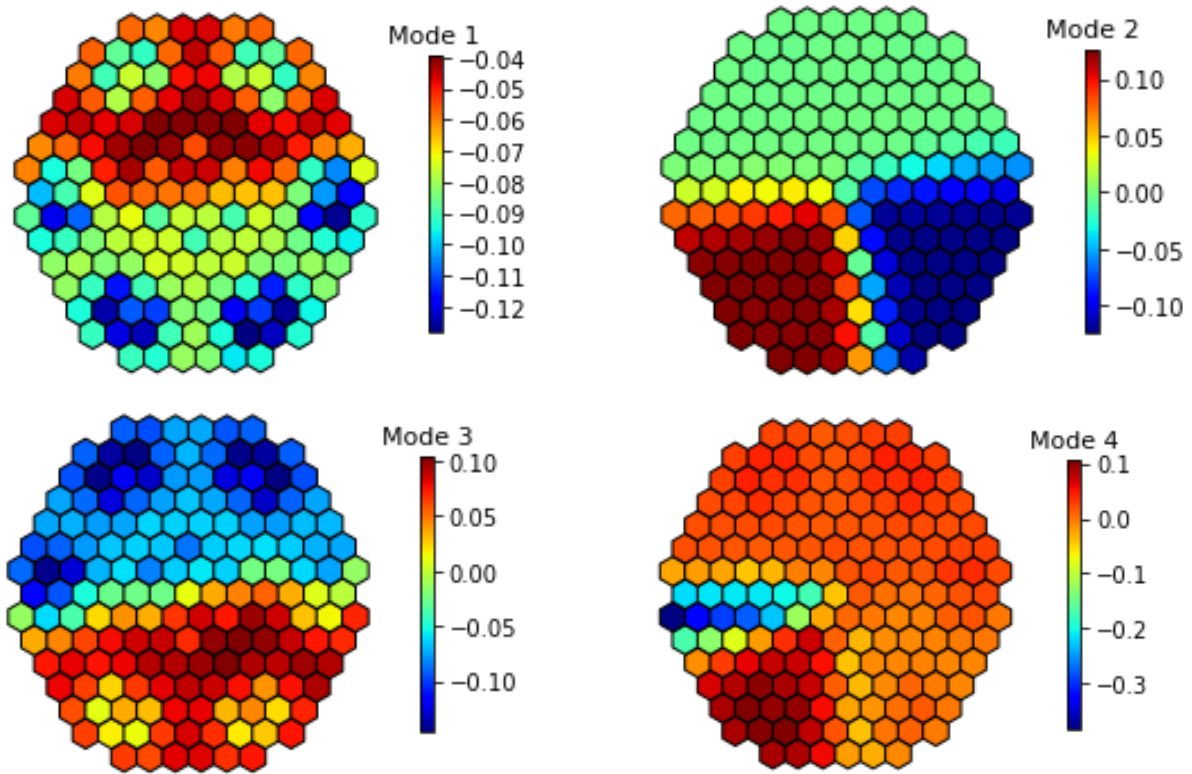


Figure 36 : 4 first modes calculated from the snapshots of ensemble Σ_{GHM} with FRAMATOME model.

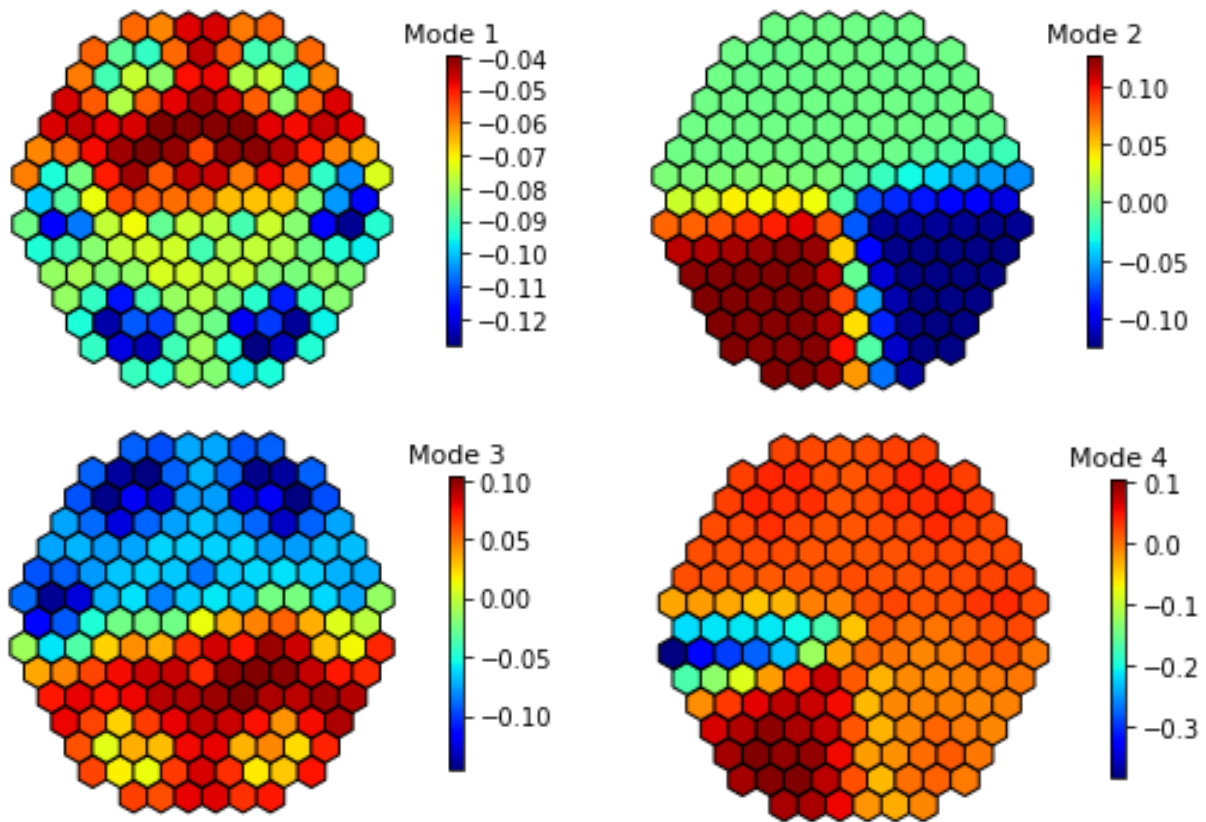


Figure 37 : 4 first modes calculated from the snapshots of ensemble Σ_{KRT} with FRAMATOME model.

Table 10: FRAMATOME - Correlation of the components of the POD with the inputs – Importance of the correlation given with shades of orange.

Ensemble	Component	$corr(y, X_1)$	$corr(y, X_2)$	$corr(y, X_3)$	$corr(y, X_4)$
Σ_{STD}	$y = a_1$	-4,40E-02	-3,70E-01	-3,60E-01	-8,56E-01
	$y = a_2$	9,51E-02	-6,73E-01	7,33E-01	-2,23E-02
	$y = a_3$	-6,20E-03	-6,39E-01	-5,70E-01	5,16E-01
	$y = a_4$	-9,94E-01	-4,40E-02	8,99E-02	3,24E-02
Σ_{GHM}	$y = a_1$	-4,73E-02	-3,65E-01	-3,53E-01	-8,60E-01
	$y = a_2$	8,91E-02	-6,81E-01	7,26E-01	-1,33E-02
	$y = a_3$	3,66E-03	6,33E-01	5,84E-01	-5,08E-01
	$y = a_4$	-9,95E-01	-4,13E-02	8,40E-02	3,79E-02
Σ_{KRT2}	$y = a_1$	-4,76E-02	-3,67E-01	-3,59E-01	-8,57E-01
	$y = a_2$	9,16E-02	-6,81E-01	7,27E-01	-2,12E-02
	$y = a_3$	3,60E-03	6,35E-01	5,82E-01	-5,08E-01
	$y = a_4$	-9,87E-01	-3,49E-02	8,58E-02	1,10E-01

4.3.2.3. KIT

Evaluations of KIT model were performed on Hadamard ensemble Σ_{HAD} . The 8 snapshots were then used to evaluate the POD modes and eigenvalues. The relative information content (RIC) is given as a function of the POD truncation on Figure 38. The values of the RIC show that $N_{POD} = 4$ is sufficient to obtain $RIC(N_{POD}) \geq 0.99$. The four first modes calculated are given on Figure 39. It can be noticed that the three first modes show strong similarities to the one obtained by FRAMATOME model with the different ensembles. The correlation of the components to the input parameters are indicated in Table 11. The behavior of the components with variations of the input parameters is similar to what has been observed with the FRAMATOME model:

- A strong anti-correlation to the power variations is visible on component a_1 , which is also moderately anti-correlated to the inlet temperature in cold leg 1 and cold leg 2.
- Mode 2 which is antisymmetric between the legs 1 and 2 shows correlations of different signs for the temperature in these legs.
- Mode 3 is correlated to both cold legs temperature variations and anticorrelated to the core total power. Also, in comparison to FRAMATOME's model, the flowrate in cold leg 1 is slightly more important as the component associated to mode 3 shows more correlation to it.
- Mode 4 is strongly anticorrelated to the flow rate in leg 1. Differences can be noticed with FRAMATOME mode 4 where the expression of this mode changes the field at the junction between leg 1 and leg 4 on the left-hand side of the figure as it can be seen on Figure 36d) for instance. In the case of KIT snapshots, the flowrate effect is strong on three FA at the junction between leg 1 and leg 2, and more moderate on different fuel assemblies which are more scattered in the core.

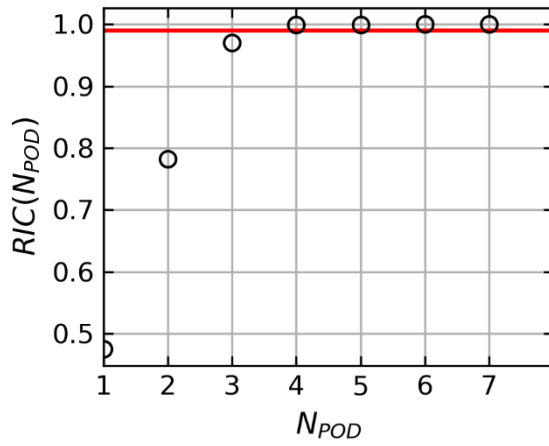


Figure 38 : RIC as a function of the number of modes for the POD applied to the snapshots of the different ensembles evaluated by KIT.

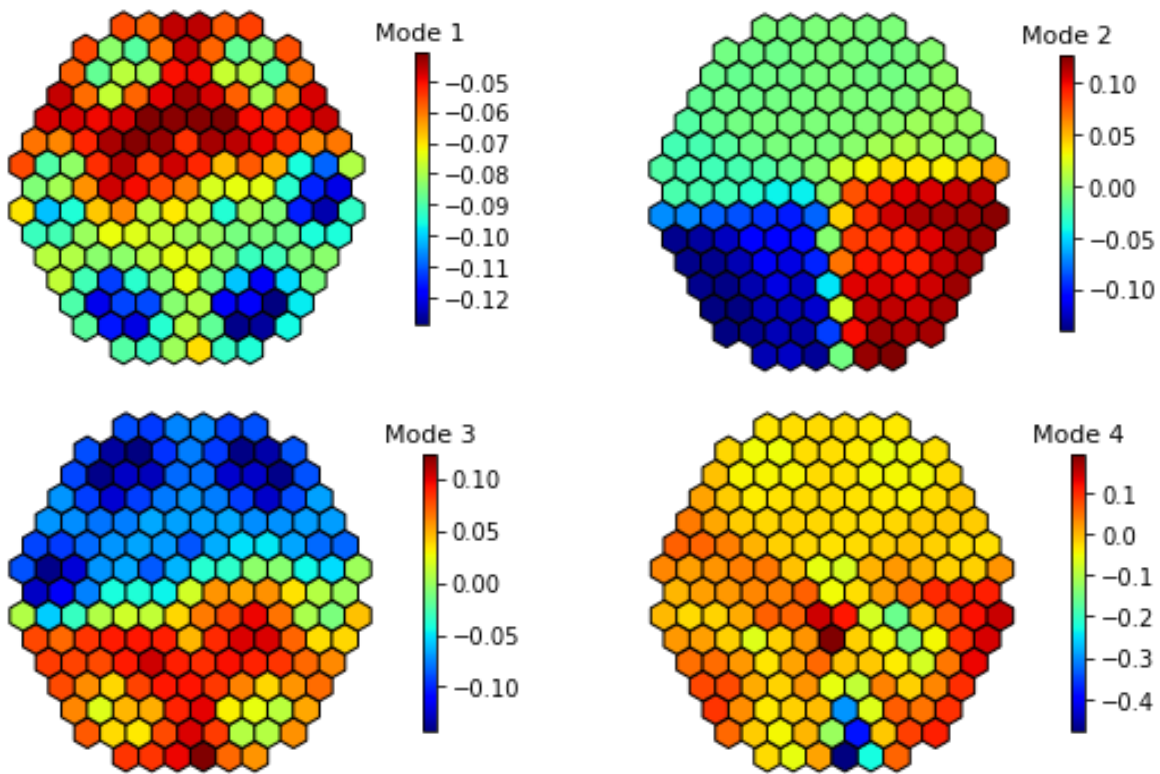


Figure 39 : 4 first modes calculated from the snapshots of ensemble Σ_{HAD} with KIT model.

Table 11: KIT - Correlation of the components of the POD with the inputs – Importance of the correlation given with shades of orange.

Ensemble	Component	$corr(y, X_1)$	$corr(y, X_2)$	$corr(y, X_3)$	$corr(y, X_4)$
Σ_{HAD}	$y = a_1$	-5,37E-02	-3,92E-01	-3,49E-01	-8,49E-01
	$y = a_2$	1,38E-01	7,06E-01	-6,93E-01	-4,95E-02
	$y = a_3$	2,51E-01	5,28E-01	6,25E-01	-5,17E-01
	$y = a_4$	-9,56E-01	2,63E-01	8,36E-02	-9,54E-02

4.3.2.4. UNIFI

Evaluation of UNIFI model were performed on ensembles Σ_{HAD} and Σ_{GHM} (respectively 8 and 9 computations). The snapshots associated to both ensembles were then used to evaluate the POD modes and eigenvalues. The relative information content (RIC) is given as a function of the POD truncation for each ensemble on Figure 40. The values of the RIC show that $N_{POD} = 4$ is sufficient to obtain $RIC(N_{POD}) \geq 0.99$. The four first modes calculated on each ensemble are given on Figure 41 and Figure 42.

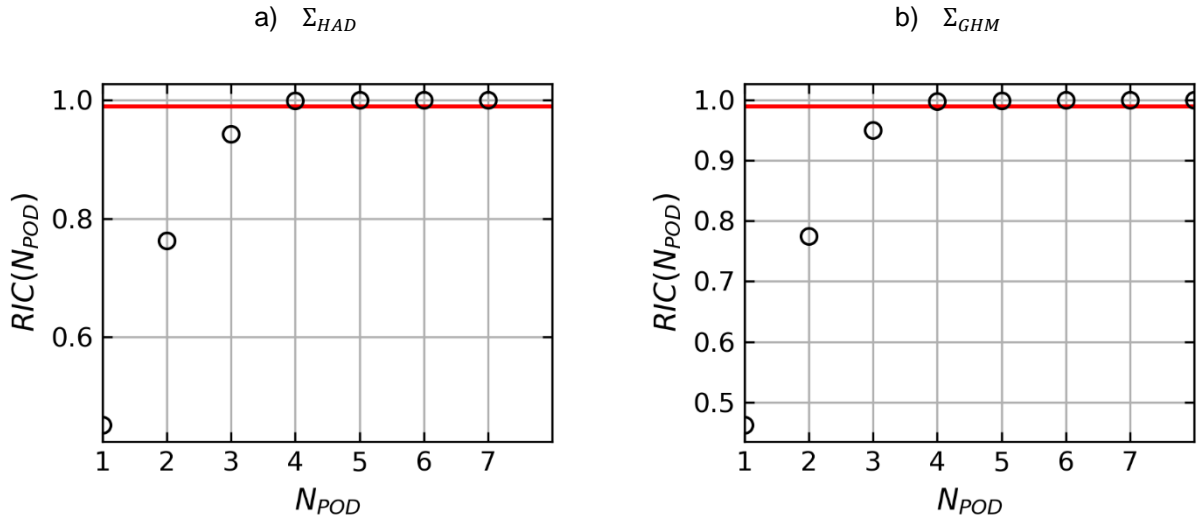


Figure 40 : RIC as a function of the number of modes for the POD applied to the snapshots of the different ensembles evaluated by UNIFI.

The importance of mode 1 and 2 are slightly changed between the two ensembles with a relative information content $RIC(N_{POD} = 1)$ lower for evaluations on Σ_{GHM} than for Σ_{HAD} . When looking more precisely the topology of all the modes, the structures are similar to the modes obtained by FRAMATOME and KIT. The same remarks can be made on the modes 1, 2 and 3. In addition, the mode 3 includes higher values near the junction between leg 1 and leg 2 which is not visible on the other partners modes. More important differences are visible on the mode 4 which impacts fuel assemblies at the junction between legs 1 and 2. The correlation of the components to the different inputs are given on Table 12. Remarks can be made on the correlation of the components to the different input parameters:

- The correlations of components to the inputs show strong similarities to the results obtained with FRAMATOME and KIT models.
- It should be noted that as for KIT, the parameter X_1 corresponding to the flowrate in cold leg 1 Q_1 has more importance than in FRAMATOME model with higher correlation to the variations of component a_3 .
- Small differences can be seen between the behavior of the model evaluated on Σ_{HAD} and Σ_{GHM} ensembles.

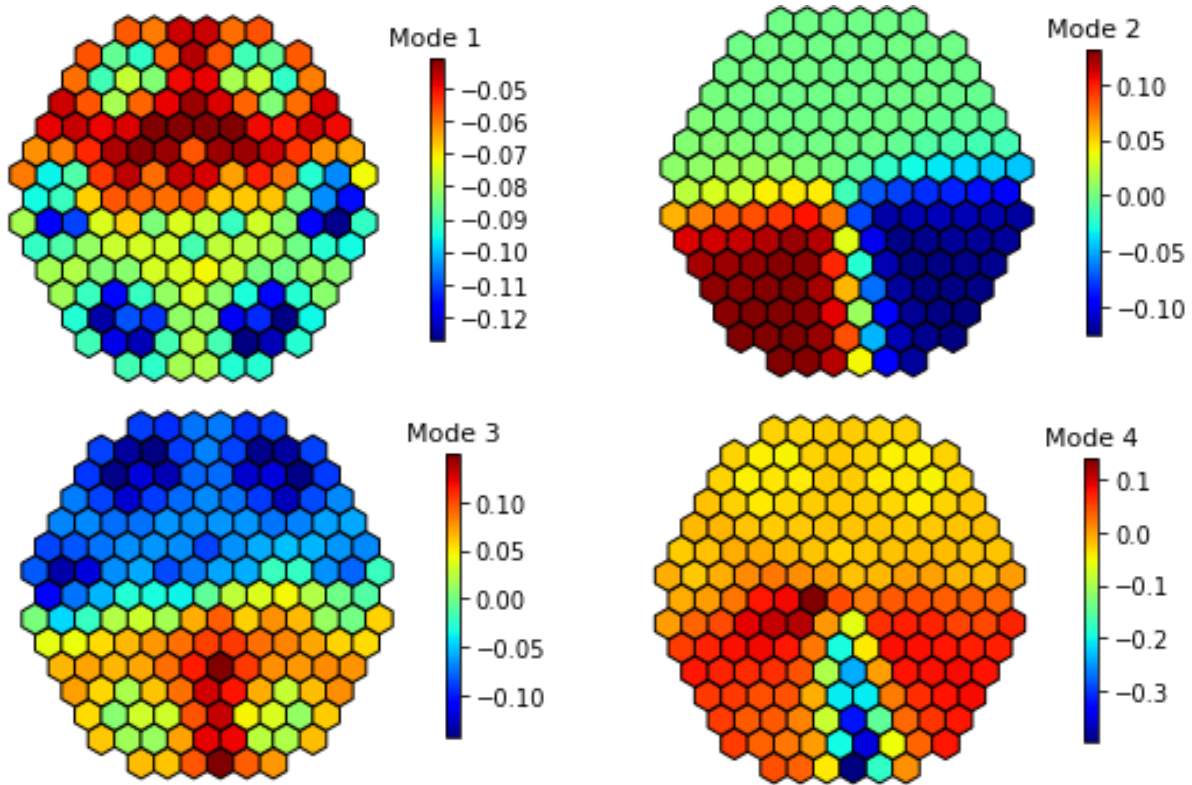


Figure 41 : 4 first modes calculated from the snapshots of ensemble Σ_{HAD} with UNIPI model.

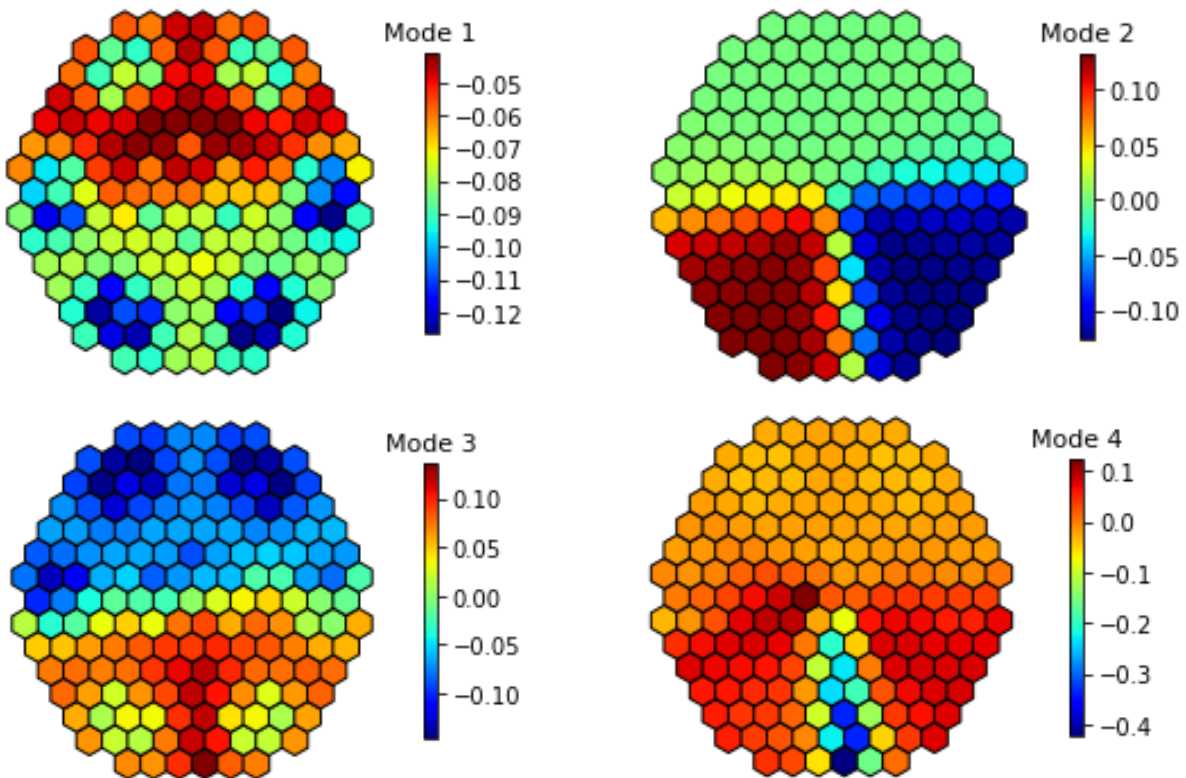


Figure 42: 4 first modes calculated from the snapshots of ensemble Σ_{GHM} with UNIPI model.

Table 12 : UNIFI - Correlation of the components of the POD with the inputs – Importance of the correlation given with shades of orange

Ensemble	Component	$corr(y, X_1)$	$corr(y, X_2)$	$corr(y, X_3)$	$corr(y, X_4)$
Σ_{HAD}	$y = a_1$	-5,11E-02	-3,69E-01	-3,51E-01	-8,59E-01
	$y = a_2$	-3,08E-02	-6,88E-01	7,25E-01	1,03E-03
	$y = a_3$	3,01E-01	5,82E-01	5,67E-01	-4,99E-01
	$y = a_4$	-9,49E-01	2,27E-01	1,75E-01	-1,12E-01
Σ_{GHM}	$y = a_1$	-4,88E-02	-3,64E-01	-3,44E-01	-8,44E-01
	$y = a_2$	-2,99E-02	-6,95E-01	7,18E-01	9,63E-03
	$y = a_3$	2,54E-01	5,83E-01	5,82E-01	-5,05E-01
	$y = a_4$	-9,04E-01	1,91E-01	1,45E-01	-7,60E-02

4.3.2.5. Comparison between partners

The results of the sensitivity analysis done by using POD showed strong similarities between FRAMATOME, KIT and UNIFI models:

- The total power in the core and the inlet temperature in cold leg 1 and 2 impact importantly the variations of $T_{FA,o}(i)$. The impact of power in the core is mainly brought by the expression of mode 1 and 3 while the impact of the temperatures in cold leg 1 and 2 are brought by mode 1, 2 and 3.
- The flowrate in cold leg 1 impacts a more limited number of fuel assemblies in the core which are given by mode 4. The topology of this mode shows more variation between partners and is related to the evolution of the mixing maps in the core on the range covered by the input parameters.
- The correlations of the POD components are similar when evaluated on different ensembles.

In comparison, ENERGORISK model showed an increased sensitivity of the mixing in the core to the input parameters which made the emergence of correlations harder.

The snapshots obtained with FRAMATOME, KIT and UNIFI models were used to find a POD base general to all three partners. In addition, ENERGORISK snapshots were projected on this base to see if correlations could emerge by finding an appropriate base. The relative information content for this POD base is given on Figure 43. The results indicate that 7 modes are required to satisfy $RIC(N_{POD}) \geq 0.99$. When compared to the RIC obtained from the POD applied separately to the different ensembles, additional modes are required to correctly represent the fluctuations. The 6 first modes are indicated on Figure 44. Different remarks can be made on these modes:

- The three first modes show strong similarities to the ones obtained for the FRAMATOME, KIT and UNIFI models independently. Differences can be seen on mode 2 due to differences in the mixing between cold leg 1 and 2 but its expression still shows the mixing between legs 1 and 2.
- Differences start appearing from modes 4 to 6 which seem more related to the mixing of leg 1 as their appearance impacts the boundaries between zone 1 and 4 and between 1 and 2. The mode 7 is not depicted on the figure

The correlation between the components associated to the 7 first modes and the inputs parameters are calculated for different ensembles of the different CFD models and given on Table 13.

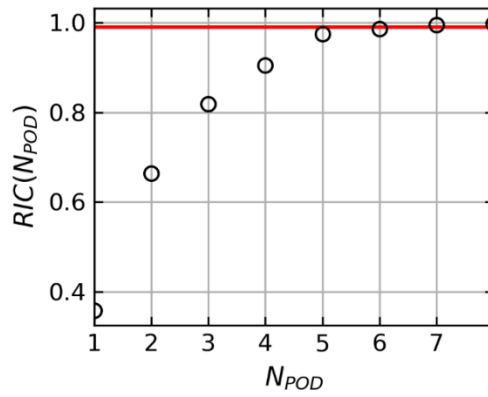


Figure 43 : RIC as a function of the number of modes

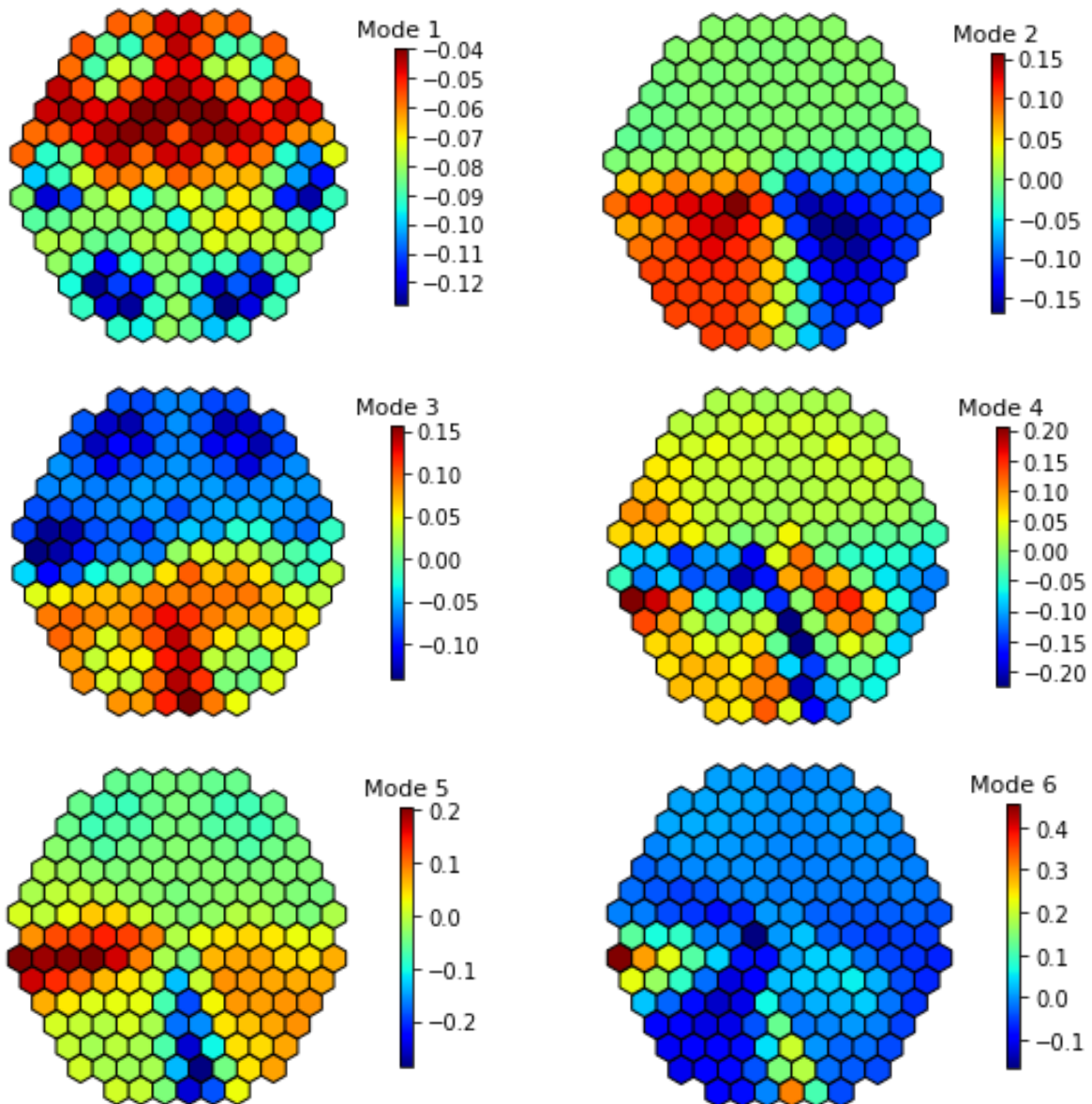


Figure 44: 6 first modes calculated from all the snapshots evaluated with FRAMATOME, KIT and UNIPI models.

Table 13 : Correlation between the components of the POD and the input parameters evaluated on different CFD models and ensembles.

Ensemble	Component	$corr(y, X_1)$	$corr(y, X_2)$	$corr(y, X_3)$	$corr(y, X_4)$
ENEKRT	$y = a_1$	-4,92E-02	-3,58E-01	-3,68E-01	-8,57E-01
	$y = a_2$	1,18E-01	-7,31E-01	6,71E-01	-3,72E-02
	$y = a_3$	-4,26E-02	4,91E-01	7,16E-01	-4,93E-01
	$y = a_4$	-3,30E-01	-7,50E-01	4,57E-01	3,45E-01
	$y = a_5$	6,34E-01	6,60E-01	2,01E-01	-3,42E-01
	$y = a_6$	9,87E-01	-1,44E-01	1,14E-02	-2,92E-03
	$y = a_7$	9,46E-01	-7,71E-02	7,09E-03	-2,99E-01
FRAKRT	$y = a_1$	-5,43E-02	-3,59E-01	-3,54E-01	-8,41E-01
	$y = a_2$	-1,11E-02	-7,22E-01	6,91E-01	-2,98E-02
	$y = a_3$	2,85E-01	5,06E-01	6,13E-01	-5,30E-01
	$y = a_4$	-3,04E-01	-7,23E-01	5,07E-01	3,46E-01
	$y = a_5$	-7,19E-01	3,98E-01	3,89E-01	-1,41E-01
	$y = a_6$	9,64E-01	1,06E-01	-2,37E-01	-5,04E-02
	$y = a_7$	9,02E-01	1,64E-01	7,47E-02	-1,86E-01
KITHAD	$y = a_1$	-5,17E-02	-3,74E-01	-3,63E-01	-8,52E-01
	$y = a_2$	-1,44E-01	-7,58E-01	6,34E-01	-4,79E-02
	$y = a_3$	2,66E-01	4,92E-01	6,64E-01	-4,96E-01
	$y = a_4$	-6,97E-02	-6,71E-01	6,77E-01	2,92E-01
	$y = a_5$	-5,57E-01	4,15E-01	6,37E-01	-3,01E-01
	$y = a_6$	9,14E-01	-1,84E-01	-2,81E-01	-2,09E-01
	$y = a_7$	8,32E-01	-3,77E-01	-2,55E-01	-2,63E-01
UNIGHM	$y = a_1$	-5,49E-02	-3,83E-01	-3,53E-01	-8,49E-01
	$y = a_2$	-3,31E-01	-6,06E-01	5,00E-01	-1,05E-01
	$y = a_3$	-8,05E-02	4,53E-01	4,65E-01	6,97E-02
	$y = a_4$	-6,33E-01	-4,38E-01	4,08E-01	2,08E-01
	$y = a_5$	-1,30E-01	-1,80E-01	-1,66E-01	-3,53E-01
	$y = a_6$	7,07E-01	-1,85E-03	-2,53E-01	-9,70E-02
	$y = a_7$	6,25E-01	-1,47E-01	-1,89E-01	-1,25E-01

Different comments can be made regarding the sensitivity of each component to the input parameters:

- Mode 1: all partners have the same behavior, with correlations to the four input parameters close to each other.
- Mode 2: the correlation of a_2 to X_2 and X_3 is similar for the different models with opposite signs of the evaluated correlation. Slight differences can be seen for the UNUPI model which yields a more important correlation to parameter X_1 corresponding to the flowrate in cold leg 1.
- Mode 3: all models show positive correlation between the component a_3 and the parameters X_2 and X_3 which ranges between 0.4 and 0.7. Slightly lower values are found with UNUPI model on Σ_{GHM} ensemble, in addition, all partners find an anticorrelation around -0.5 with the parameter X_4 except the UNUPI model.
- Mode 4: All models show correlation of a_4 with X_2 and X_3 around the same amplitude. However, the correlation to the flowrate X_1 differs between models: the UNUPI models yields high anti-correlation of this component to the flowrate, while ENERGORISK and FRAMATOME are slightly lower. In contrast, KIT does not show any correlation between the flowrate and this component.
- Modes 5, 6 and 7: the components associated to these modes show important correlation to the flowrate. Differences are however seen between models especially regarding the sign of the correlation. However for all models, these components variations are mainly due to variations of the flowrate with lower effect of the temperatures in cold leg 1 and 2.

An interesting result is the fact that ENERGORISK model shows similar behavior as the other models when projected in the same POD base. In this application, the projection of ENERGORISK snapshots on the modal base calculated with the snapshots of other partners seems to have the same effect than filtering the fluctuations of temperature due to the unstable mixing in the core. For a sensitivity study, this process has some interest as it allows to bring out the correlation between identified spatial fluctuations and variation of inputs. Nevertheless, the truncation error when reconstructing in such a base must be considered to reflect the real variability of the results.

4.3.3. Evaluation of quantiles

The same process applied to $T_{HL,1}(t)$ to evaluate quantiles with the Metalog distribution in §4.2.4 is used to evaluate quantiles of $T_{FA,o}(i)$ with the different DS ensembles for the different CFD models. Quantiles evaluated on Σ_{KRT2} with FRAMATOME model are given on Figure 45. The data is rearranged on an (x,y) plot on Figure 46 on which different quantiles are indicated. Also, examples are given on Figure 47 for the other models/ensembles:

- The results are similar between FRAMATOME, UNUPI and KIT models: the minimum-maximum difference is important in regions presenting local minimum or maximum, reaching values of 4°C.
- An increased uncertainty is present on the ENERGORISK model where the amplitude between the 2.5% quantile and the 97.5% quantile reaches values over 5°C. In addition, regions which are not affected by the inputs' uncertainty in FRAMATOME, UNUPI and KIT model are affected in ENERGORISK model. It should be mentioned that the results obtained with this model were found to be closer to experiments than FRAMATOME, UNUPI and KIT in deliverable D6.2 [3].

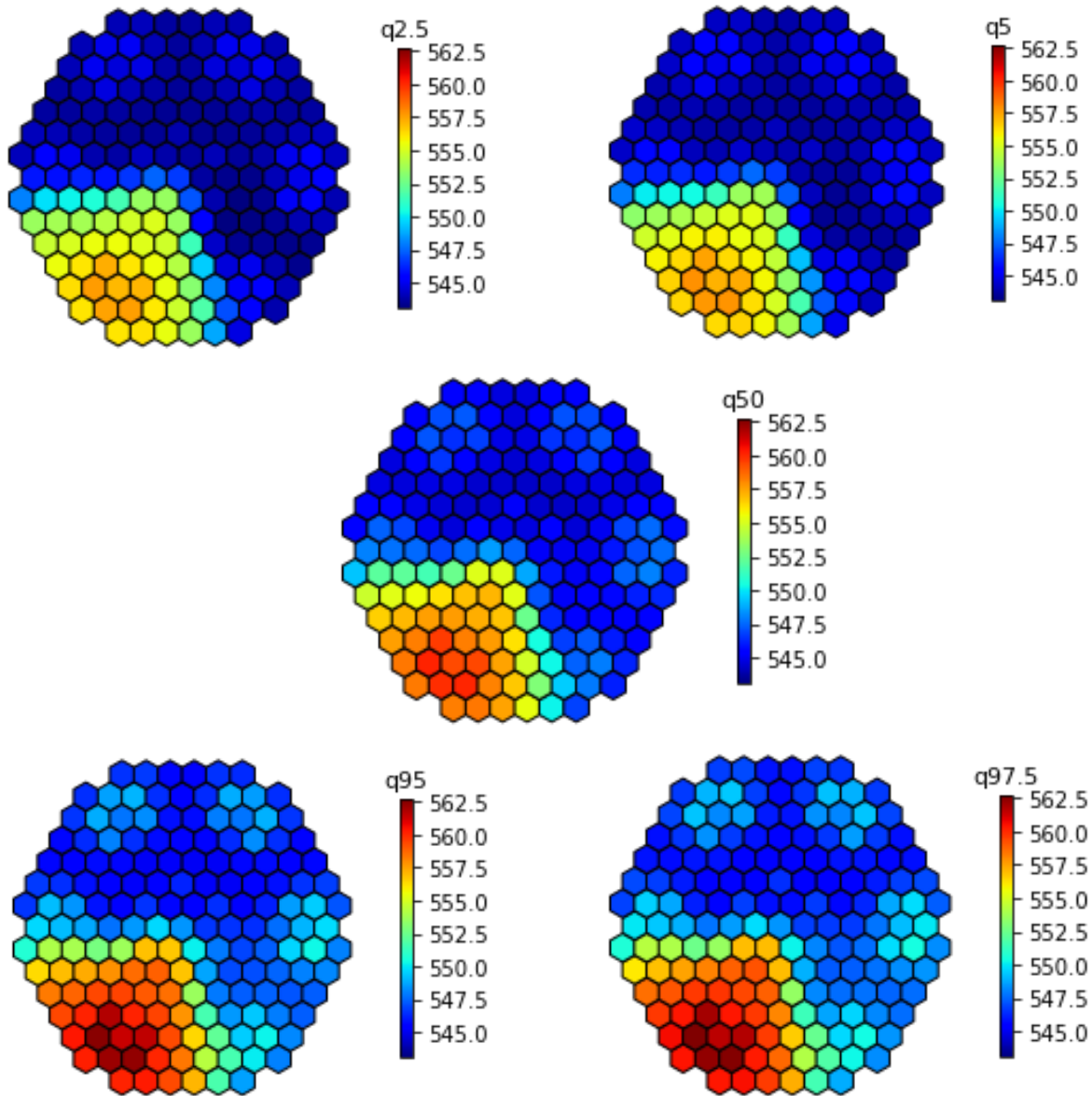


Figure 45: quantiles of $T_{FA,0}(i)$ evaluated with FRAMATOME model on Σ_{KRT} ensemble.

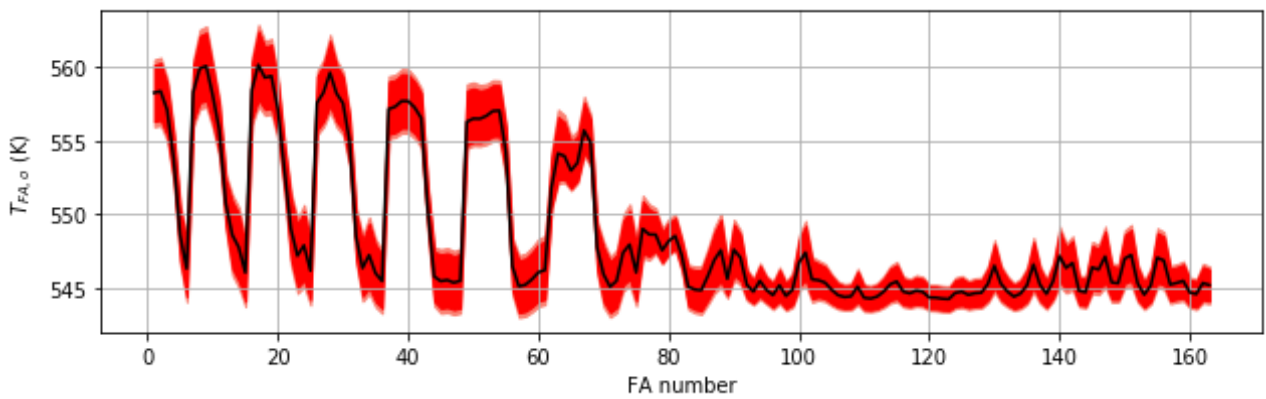


Figure 46 : Median temperature $T_{FA,0}(i)$ evaluated with FRAMATOME model on Σ_{KRT} ensemble (solid black line). The interval between the 5% quantile and 95% quantile is filled in red, and the 2.5% 97.5% quantiles in salmon.

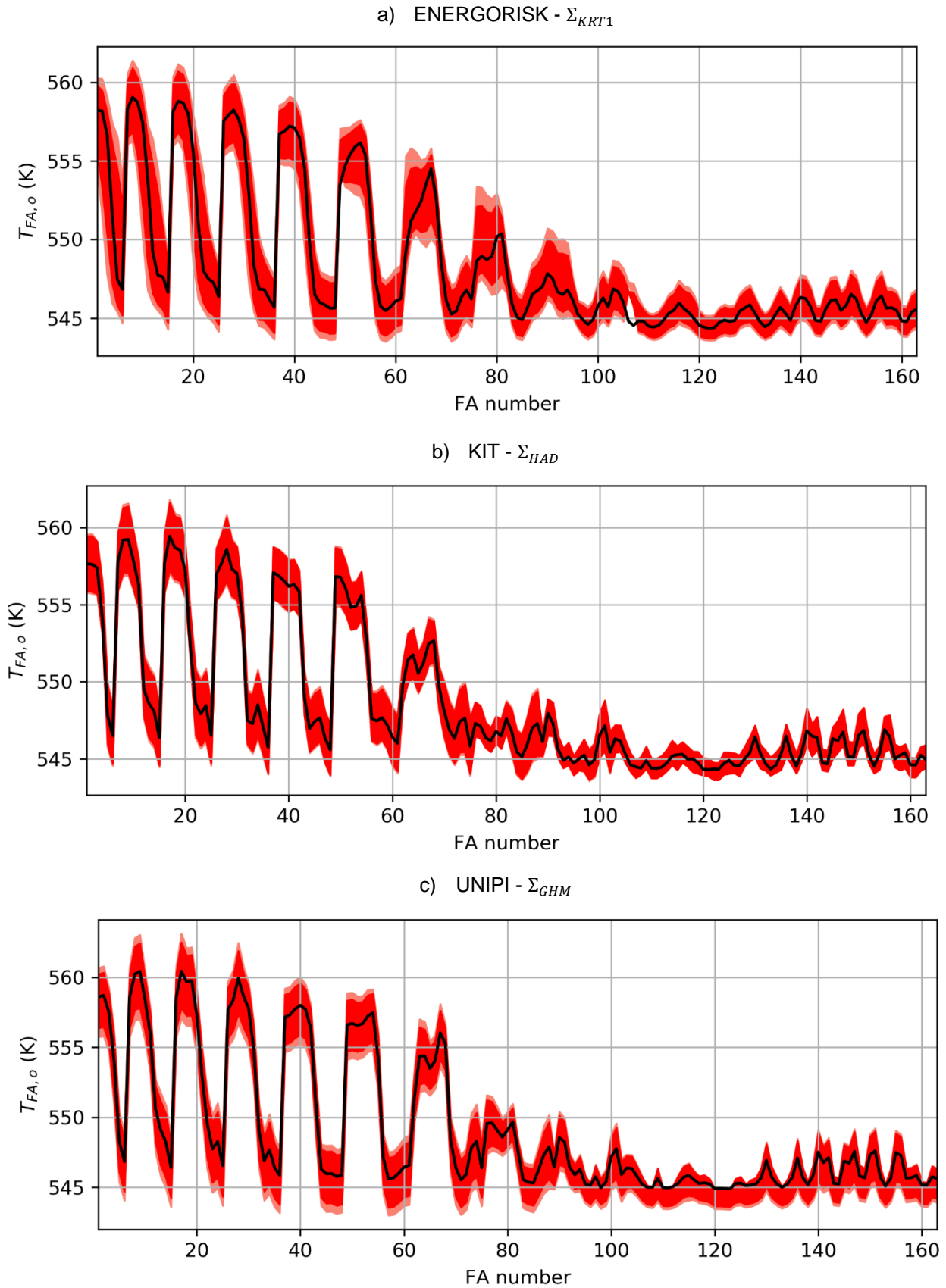


Figure 47: Examples of quantiles evaluated for different models on different ensembles. Median (solid black line), [2.5,97.5%] interval filled in salmon and [5,95%] interval filled in red

4.3.4. Conclusion on the uncertainty of $T_{FA,o}$

In this section, statistical moments and quantiles of $T_{FA,o}(i)$ were given for different models and different DS ensembles. In addition, a sensitivity analysis has been performed by applying the POD to snapshots obtained from the different models. Different conclusions can be drawn based on the results presented:

- The results obtained with FRAMATOME, KIT and UNUPI models showed similarities in terms of amplitude of the uncertainty standard deviation. In contrast, ENERGORISK's model yielded standard deviation higher due to more important fluctuations of the mixing in the core during the transient. Their model was in fact more sensitive to input parameters, resulting in higher variance. As it has been indicated previously, the use of the $k - \omega$ SST model combined to the meshing strategy yield more unsteady results that might be smoothed by the models of the other partners. Further studies on the impact of the mesh should be done to verify this assumption.
- The sensitivity analysis performed highlighted different structures of the fluctuations whose amplitude were correlated to some of the input variations.
 - o For all models, the most important fluctuation mode was brought by simultaneous increase of the power and of the temperature in cold legs 1 and 2. This mode showed lobes on which fluctuations were found to be more important, and showed an important amplitude of the fluctuations on the lower part of the 2D field in zones influenced by legs 1 and 2. The topology of this mode is similar to the topology of the standard deviation obtained with the DS ensembles for most of the partners.
 - o The differences between the partners were mostly due to differences in the mixing of cold legs 1 and 2. The boundaries between the two zones influenced by the two cold legs were different for the different models leading to different effects of the temperature variations in cold legs 1 and 2. Nevertheless, the impact has been found to be negligible in front of the variation of power in the core and in front of the varying temperatures in the cold legs 1 and 2.
 - o The ENERGORISK model showed important fluctuation of the mixing in the core which covered up correlations to the inputs. However, the POD base calculated with snapshots of the other CFD models was used to evaluate components of ENERGORISK snapshots which were then used for the calculation of correlations. This process was found effective to bring up correlations between the components associated to the different modes and the inputs. The components showed similar behaviour of the ENERGORISK model compared to the others. Nevertheless, projecting in this base does not reflect the real variability of the snapshots as the truncation error in this case is significant.
- As for $T_{HL,1}(t)$, the correlations calculated with the different DS ensembles were close for FRAMATOME, KIT and UNUPI model. For ENERGORISK, the correlations were similar when projected on the POD base found with the other partners snapshots. In addition, noticeable changes in the confidence intervals were found when enforcing the fourth order moments. For instance, the UNUPI model evaluated on Σ_{GHM} included a computation for which important deviation was found with other samples. The inclusion of this computation combined to the enforcement of the fourth order statistical moment induced a lower 2.5% quantile than when evaluated on Σ_{STD} .

In conclusion of the processing of the FA temperature average, the results were similar for most of the partners with an important effect of the power variations in the core and an amplitude of

the uncertainty around 1°C on average. Only ENERGORISK model presenting additional variations due to the less stable mixing was observed with values of the standard deviation increased at junctions between mixing zones reaching 2°C to 3°C.

5. Conclusion

In this study, the mixing experiment on Kozloduy-6 reactor has been reproduced with different CFD models. Four boundary conditions of the CFD model were selected for their impact on the quantities of interest and set as uncertain. Deterministic sampling was then used to find alternative representations of these random variables based on different ensembles that have been briefly described. Four ensembles were used:

- The Standard ensemble Σ_{STD} , enforcing the Random Variables (RV) marginal moments up to order 3 and mixed moments up to order 4
- The Hadamard ensemble Σ_{HAD} , enforcing the RV marginal moments up to order 3 and mixed moments up to order 2.
- The Gauss Heavy middle ensemble Σ_{GHM} , enforcing the RV marginal moments up to order 4 and mixed moments up to order 2.
- A hybrid ensemble Σ_{KRT} , with the same representation complexity than Σ_{GHM} but combining evaluation with the Hadamard ensemble and the standard ensemble. Two versions Σ_{KRT1} and Σ_{KRT2} were provided.

These ensembles were then used to evaluate the CFD response which then enabled the assessment of the statistical moments of the outputs. The statistical moments were then used to fit a Metalog distribution which provided quantiles on the different outputs.

In the first place, it should be noted that the propagation through the different CFD models yielded significant similarities. The estimated uncertainty is coherent with the amplitude of the inputs variations with moderate values for most of the models results presented in §4.1 §4.2 and §4.3. An important effect of mixing has been found due to its role in the calculation of temperature in the core based on cold legs temperature. In fact, the small differences between the propagated uncertainty which were found between the partners were mainly due to the difference of mixing in the core which affects the way temperature in cold legs 1 and 2 propagates through the core. On most of the models (FRAMATOME, KIT, UNIP) the mixing fluctuations were shown to be negligible. However, the mixing was found to be more sensitive on ENERGORISK model which induced an increased uncertainty. It should also be mentioned that the results obtained with this model were slightly better for the calculation of the temperature in hot leg 1 as shown in §4.2.

Also, the POD was used to make a brief sensitivity analysis and try to correlate the fluctuations of the temperature and mixing in the core to input parameters. Its use brought out modes of fluctuations related to the mixing map, the power distribution, and the flow rate distribution in the core. This decomposition was found to be effective to support assessment on the way variations of inputs were propagated through computations in the core. In addition, the use of POD on ENERGORISK's model which showed initially no clear correlation of the fluctuations to the inputs' fluctuations allowed to bring to light correlations which were similar to the other models.

In conclusion, the assessment of U_{inputs} statistical moments was performed with DS and supported by POD which enabled to illustrate the effect of inputs on computations of the mixing coefficients and temperature in the core. DS was found to yield consistent results on the models which showed small fluctuations in time, yielding consistent results between partners and ensembles. The importance of evaluating simultaneous variations of parameters was also highlighted, thus, ensembles such as Σ_{HAD} , Σ_{GHM} and Σ_{KRT} should be preferred to Σ_{STD} . In this specific case, the use of Σ_{GHM} seem to be the best compromise between the number of computations and the accuracy of the assessed uncertainty. In contrast, the propagation through CFD models presenting more noisy data was more sensitive to the ensemble used, resulting in more discrepancy between ensembles and higher variance, which nevertheless remains moderate.

In general, the results were found to be close from a model to another, whether it is for the computations of the quantities of interest, or their uncertainty. This important result increases the confidence we have for mixing simulation in a VVER vessel with CFD codes.

Further studies could be done to study the impact of meshing and turbulence modelling on the unsteadiness of computations in order to give recommendation on modelling whether a low bias or low variance is sought. In addition, a 4D gaussian distribution was assumed for the input variables, in addition, independency between the four parameters was enforced. The resulting output distribution was found to be similar to the input, showing low dissymmetry and kurtosis. Alternative representations could be given to these random variables to study the impact on the output uncertainty: asymmetric distributions, covariance between parameters or even random variables inputs which are varying in time. Other parameters affecting the mixing in the core could be investigated to see their impact on the output uncertainty: swirl in cold legs, model parameters of explicit modelling of porous zones. Finally, a comprehensive study of uncertainty quantification could be performed to evaluate other sources of uncertainty (grid, experimental uncertainty, model).

6. References

- [1] D. Verrier, B. Vezzoni, B. Calgaro, O. Bernard, A. P., C. L, H. A, P. Groudev, A. Stefanova, Z. Neli, F. Damian and e. al., "Codes and Methods for VVER comprehensive Safety Assessment: The CAMIVVER H2020 Project," in ICONE 2021-64169,," 2019..
- [2] O. Bernard, M. Böttcher, A. Hashimov, D. Ruban, U. Bieder, R. Nop, O. Abdelhalim and A. Pucciarelli, "D6.1 – Description of CFD models from partners - Results of outlet flow distribution benchmark".
- [3] V. Sanchez, M. Böttcher, C. Marchand, O. Bernard, U. Bieder, R. Nop, D. Ruban, A. Hashymov, Sevbo, N. Forgione, O. Abdelhalim and A. Pucciarelli, "Deliverable D6.2 - Results of Kozloduy-6 mixing experiment benchmark".
- [4] Computational Fluid Dynamics Committee, "Guide : Guide for the Verification and Validation of Computational Fluid Dynamics Simulations AIAA G-077-1998," 2002.

- [5] S. Lee and W. Chen, "Comparative study of uncertainty propagation methods for black-box-type problems," *Structural and multidisciplinary optimization*, no. 37, pp. 239-253, 2009.
- [6] J. Morio, M. Balesdent, D. Jacquemard and C. Verge, "A survey of rare event simulation methods for static input-output models," *Simulation Modelling Practice and Theory*, vol. 49, pp. 287-304, 2014.
- [7] B. Sudret, "Meta-models for structural reliability and uncertainty quantification," *arXiv preprint arXiv:1203.2062*, 2012.
- [8] P. Hessling, "Deterministic Sampling for Propagating Model Covariance," in *SIAM/ASA Journal on Uncertainty Quantification*, 2013.
- [9] P. Hedberg and P. Hessling, "Use of Deterministic Sampling for Uncertainty Quantification in CFD," in *16th International Topical Meeting on Nuclear Reactor Thermal Hydraulics (NURETH 16)*, Chicago, Illinois, 2015.
- [10] T. W. Keelin, "The metalog distributions," *Decision Analysis*, vol. 13, no. 4, pp. 243-277, 2016.
- [11] S. J. Julier and J. K. Uhlmann, "Unscented filtering and nonlinear estimation," *Proceedings of the IEEE*, vol. 92, no. 3, pp. 401-422, 2004.
- [12] L. Sirovich and M. Kirby, "Application of the Karhunen-Loeve procedure for the characterization of human faces," *Journal of the Optical Society of America A*, vol. 4, no. 3, pp. 519-524, 1987.
- [13] K. L. Diamantaras and S. Y. Kung, *Principal component neural networks: theory and applications*, John Wiley & Sons, Inc., 1996.
- [14] J. L. Lumley, "The structure of inhomogeneous turbulent flows," *Atmospheric turbulence and radio wave propagation*, pp. 221-227, 1967.
- [15] G. Berkooz, P. Holmes and J. L. Lumley, "The proper orthogonal decomposition in the analysis of turbulent flows," *Annual review of fluid mechanics*, vol. 25, no. 1, pp. 539-575, 1993.
- [16] P. J. Holmes, J. L. Lumley, G. Berkooz, J. C. Mattingly and R. W. Wittenberg, "Low-dimensional models of coherent structures in turbulence," *Physics Reports*, vol. 287, no. 4, pp. 337-384, 1997.
- [17] L. Cordier and M. Bergmann, "Proper Orthogonal Decomposition: an overview. Lecture series 2002-04, 2003-4, 3 and 2008-01 on post-processing of experimental and numerical data," Von Kármán Institute for Fluid Dynamics, 2008.
- [18] L. Margheri and P. Sagaut, "A hybrid anchored-ANOVA – POD/Kriging method for uncertainty quantification in unsteady high-fidelity CFD simulations," *Journal of Computational Physics*, vol. 324, pp. 137-173, 2016.
- [19] Q. Lu, L. Wang and L. Li, "Efficient uncertainty quantification of stochastic problems in CFD by combination of compressed sensing and POD-Kriging," *Computer Methods in Applied Mechanics and Engineering*, vol. 396, pp. 115-118, 2022.

- [20] P. Virtanen, R. Gommers, T. E. Oliphant, M. Haberland, T. Reddy, D. Cournapeau, E. Burovski, P. Peterson, W. Weckesser, J. Bright, S. J. van der Walt, M. Brett, J. Wilson and K. J. Millman, "SciPy 1.0: Fundamental Algorithms for Scientific Computing in Python," *Nature Methods*, vol. 17, pp. 261-272, 2020.
- [21] B. A. Belson, J. H. Tu and C. W. Rowley, "Algorithm 945: modred—a parallelized model reduction library," *ACM Transactions on Mathematical Software (TOMS)*, vol. 40, no. 4, pp. 1-23, 2014.

A. Building ensemble

Activation matrices

Previous work has been done in the field of deterministic sampling providing ensembles that can be used as elementary bricks for the construction of the ensemble $\underline{\Sigma}$ by using different operations described further on (aggregation, parametrization, and padding).

The activation matrices that are used in the CAMIVVER application are:

- The Standard matrix named Σ_{STD}
- The Hadamard matrix named Σ_{HAD}
- The Binary matrix named Σ_{BIN}

The ensembles are given for normalized random variables. In addition, the presented ensembles aim to enforce independence between parameters. These ensembles can then be transformed as indicated in [8] to add covariance between parameters.

It should be noted that the following ensembles are used with equal weights.

$$w_i = \frac{1}{N_{\Sigma}}$$

Standard ensemble

The Standard ensemble $\underline{\Sigma}_{STD}$ which originates from the Unscented Kalman Filtering (UKF) to propagate covariance [11] is one of the simplest ensembles in terms of complexity. Its expression for any order p is as follows:

$$\underline{\Sigma}_{STD} = \sqrt{p} \cdot (I_{p \times p} \quad -I_{p \times p})$$

This ensemble enables the propagation of covariance with $N = 2p$ points which allows to explore two values for each parameter. It can be shown that the Standard matrix encodes in the case of a p dimensional normal distribution the marginal moments up to order 3. In fact, the symmetry of the ensemble guarantees nil valued odd statistical moments. In addition, the second moment is verified. We obtain the following equation when evaluating the marginal moments of order 2 of the RV:

$$\forall j \leq p, \langle \delta X_j^2 \rangle = \frac{1}{2p} \cdot (\sqrt{p})^2 + \frac{1}{2p} \cdot (-\sqrt{p})^2 = 1$$

Which is the value awaited for a gaussian RV. For order 4, we obtain

$$\langle \delta X_j^4 \rangle = \frac{1}{2p} \cdot (\sqrt{p})^4 + \frac{1}{2p} \cdot (-\sqrt{p})^4 = p$$

The value of 3 is expected for a normal distribution thus, this ensemble does not correctly represent the 4th marginal moment of a gaussian RV for $p \neq 3$.

In conclusion, this ensemble correctly represents the RV up to order 3 with $2p$ samples. The low number of elements and the simplicity of use are its advantages; however, the Standard Ensemble presents some limitations for the propagation of covariance through a function f :

- Only the partial derivative of the function f are evaluated; if f is nonlinear, the mixed derivative can have their importance which would lead to important differences with other ensembles taking them into account
- When the dimension of the RV increases, the \sqrt{p} term in front of the matrix can scale importantly. For non-linear physics such as CFD, an increasing scaling of the samples would lead to bad results.

Hadamard ensemble

The Hadamard ensemble $\underline{\Sigma}_{HAD}$ originates from Hadamard matrix that can be built with recursive rules for instance with a method from Sylvester invented in 1867

$$H_{2^n} = \begin{cases} 1, & 2^n = 1 \\ \begin{pmatrix} H_{2^{n-1}} & H_{2^{n-1}} \\ H_{2^{n-1}} & -H_{2^{n-1}} \end{pmatrix}, & 2^n > 1 \end{cases}$$

This matrix is only defined to specific orders k , thus an additional operation is done to extend its construction to any order p . The smallest integer m which is a power of 2 and such as $m \geq n + 1$ is taken to build an Hadamard matrix on which p columns are extracted:

$$\underline{\Sigma}_{HAD} = H_m(:, 2:p+1)$$

This ensemble may look like the binary ensemble in reference [8] but is built differently.

It can be shown that this Hadamard matrix correctly enforces correctly statistical moments up to order 3,

$$\forall j \leq p, \quad \langle \delta X_j^2 \rangle = \frac{1}{N_\Sigma} \cdot N_\Sigma \cdot (\pm 1)^2 = 1$$

In addition, its symmetry on each column ensures nil value for odd marginal moments as all values of a column add to zero. Regarding the fourth marginal moment:

$$\forall j \leq p, \quad \langle \delta X_j^4 \rangle = \frac{1}{N_\Sigma} \cdot N_\Sigma \cdot (\pm 1)^4 = 1$$

This value of the fourth marginal moments is different than what is expected from a normal distribution where the value $\langle \delta X_j^4 \rangle = 3$ is expected.

When looking into crossed moment, the symmetry of the ensemble induces no covariance between columns as Hadamard ensemble ensures independence between columns. Nevertheless, for higher order mixed moments, the independence of the parameters is not enforced as all the combinations of +1 and -1 are not present in the matrix.

In term of statistical moments, this ensemble is slightly less efficient than the Standard matrix, however, some qualities overcome its shortcomings for propagation through CFD:

- All combinations of 2 parameters are present which enables evaluation of the function in different directions than the principal ones.
- No scaling of the matrix when increasing the dimension of the RV

Binary ensemble

The last activation matrix presented in this paragraph is the Binary ensemble $\underline{\Sigma}_{BIN}$ which is different from the Binary ensemble of reference [8]. This ensemble includes all combinations of 1 and -1 for p parameters and thus presents the advantage of enforcing total independence between parameters by testing all possible combinations of parameters up to mixed moment of order p . In contrast, this ensemble's size is significantly higher than Hadamard ensemble with a total size of 2^p . Regarding marginal moments, the statistical moments are correctly represented up to order 3. The fourth order statistical moment is not correctly enforced for a normal distribution.

Elementary operations

The different matrices presented in the previous paragraph can be combined in order to find different ensembles with the chosen properties. The elementary operations presented in this document which are used to combine these matrices are:

- Padding: consists of adding the $\mathbf{0} = (0, \dots, 0)$ sample to the ensemble.

- Ensemble concatenation
- Scaling of the activation matrices.

These operations lead to the modification of the previous system (2-5) built for chosen statistical moments. The modification affects the weights values, and thus must be controlled to verify that the modification did not lead to high discrepancy or negative weights. In counterpart, the addition of degrees of freedom may enable the encoding of additional statistical moments of higher order.

Padding and scaling

Padding consists of adding $\mathbf{0} = (0, \dots, 0)$ sample to the ensemble.

$$\Sigma_{\text{padded}} = \begin{pmatrix} \mathbf{0} \\ \Sigma \end{pmatrix}$$

In addition, we differentiate the value of the weights associated to the ensemble Σ and to the $\mathbf{0}$ vector. When looking to the system (2-5), the equations are modified for the marginal moments. For instance, if we look for the standard activation matrix. The mean value is correctly encoded, however, when evaluating the second marginal moment of any column:

$$\forall j \leq p, \quad \langle \delta X_j^2 \rangle = w_{STD} \cdot (\sqrt{p})^2 + w_{STD} \cdot (-\sqrt{p})^2 = 2p \cdot w_{STD}$$

In addition, the sum of weights must be equal to 1:

$$N_{\Sigma_{STD}} \cdot w_{STD} + w_0 = 1$$

The enforcement of the 2nd order statistical moments is equivalent to :

$$\langle \delta X_j^2 \rangle = 1$$

$$2p \cdot w_{STD} = 1$$

Thus:

$$w_{STD} = \frac{1}{2p}$$

$$w_0 = 1 - \frac{1}{2p} \times 2p = 0$$

In this case, the padding has been used but the enforcement of the variance is possible only with $w_0 = 0$.

To increase the dimension of the space of solutions, a scaling factor a is added to the initial ensemble Σ_{STD} . With this scaling factor, enforcing the second order marginal moment results in:

$$j \leq p, \quad \langle \delta X_j^2 \rangle = w_{STD} \cdot (a\sqrt{p})^2 + w_{STD} \cdot (-a\sqrt{p})^2 = 2a^2p \cdot w_{STD}$$

$$w_{STD} = \frac{1}{2a^2p}, \quad w_0 = 1 - \frac{1}{2a^2p} \times 2p = 1 - \frac{1}{a^2}$$

Now an infinite number of solutions which are included in a 1D linear space exist and allow to encode the variance of a normal distribution ($\langle \delta X_j^2 \rangle = 1$). We can now observe the fourth moment and see if a specific value of a can reproduce the fourth order marginal moment:

$$\forall j \leq p, \quad \langle \delta X_j^4 \rangle = w_{STD} \cdot (a\sqrt{p})^4 + w_{STD} \cdot (-a\sqrt{p})^4 = 2w_{STD}a^4p^2 = 2 \cdot \frac{1}{2a^2p} \cdot a^4p^2 = a^2p$$

For a normal distribution, the enforcement of the 4th marginal moments is equivalent to:

$$a = \sqrt{\frac{3}{p}}$$

It should be noted that for $p > 3$, enforcing the fourth order moment leads to negative values of w_0 which must be avoided as it can lead to incoherent values for even statistical moments (negative values). Reproducing the process with Hadamard activation matrix leads to better results.

Matrix concatenation and scaling

Ensembles can be concatenated and scaled to gain degrees freedom on the system (2-5) and enforce additional statistical information.

If we take for instance the Standard activation matrix and the Hadamard matrix Σ_{STD} and Σ_{HAD} and denote their respective weights w_{STD} and w_{HAD} .

As both ensembles are symmetric, the aggregated matrix is also symmetric and automatically encodes the mean value and skewness of the RV. Enforcing the second and fourth marginal moments translates as follows:

$$\begin{aligned} N_{\Sigma_{STD}} \cdot w_{STD} + N_{\Sigma_{HAD}} \cdot w_{HAD} &= 1 \\ 2 \cdot w_{STD} \cdot (\pm\sqrt{p})^2 + N_{\Sigma_{HAD}} \cdot w_{HAD} \cdot (\pm 1)^2 &= 1 \\ 2 \cdot w_{STD} \cdot (\pm\sqrt{p})^4 + N_{\Sigma_{HAD}} \cdot w_{HAD} \cdot (\pm 1)^4 &= 3 \end{aligned}$$

Let's take the case of a 4D RV to simplify. The system is reduced to the following equations:

$$\begin{aligned} w_{STD} + w_{HAD} &= \frac{1}{8} \\ 32 \cdot w_{STD} + 8 \cdot w_{HAD} &= 3 \end{aligned}$$

This system has a solution:

$$w_{STD} = \frac{1}{12}, \quad w_{HAD} = \frac{1}{24}$$

As for the padding, concatenation can be used with scaling by defining two real numbers a and b scaling the matrices Σ_1 and Σ_2 . This may increase the degrees of freedom of the linear system solved to deduce the weights and potentially lead to the addition of information that can be encoded.

B. CEA results

The results obtained with CEA model are given in the following appendix. Their simulations are done with the following proces:

- A steady state is simulated
- The transient calculation is performed by frozing the flow and imposing only the temperature evolution.

In addition, the power in the core is not implemented. This is equivalent of considering only 3 uncertain parameters being the X_1 , X_2 and X_3 which are respectively, the flowrate Q_1 , the temperature in cold leg 2 T_{CL2} and the temperature in cold leg 1 T_{CL1}

a. Mixing coefficient

The mixing coefficient obtained at 800s for these computations are the ones obtained at the steady state as the flow solver is frozen during the transient. The mean value and standard deviation obtained for the different mixing zones are given respectively on Figure 48 and **Erreur ! Source du renvoi introuvable.** It should be noticed that the view is rotated in comparison to the other partners. Also, the standard deviation is found relatively stable for the different inputs that were scanned.

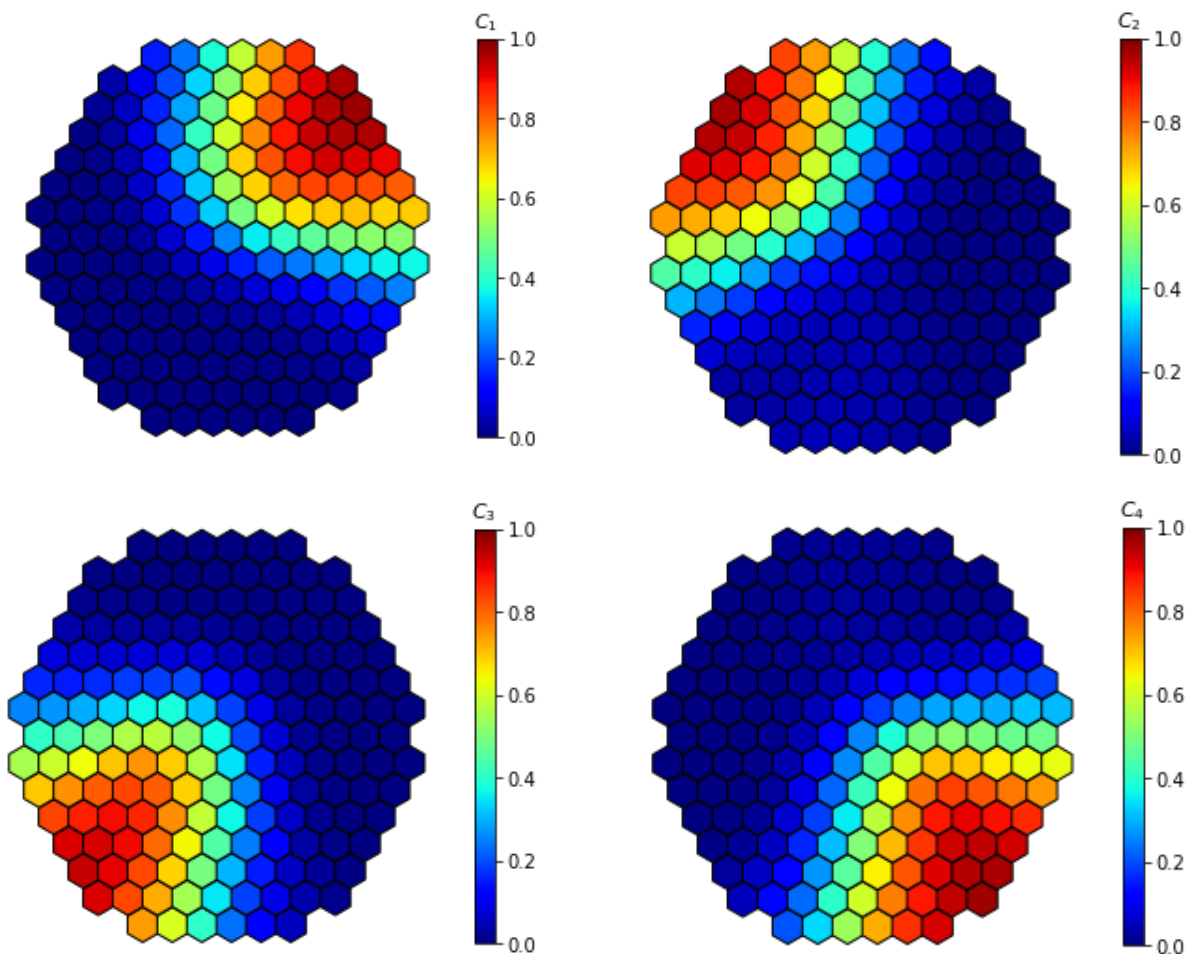


Figure 48 : Mean value of the mixing coefficients C_1 , C_2 , C_3 and C_4

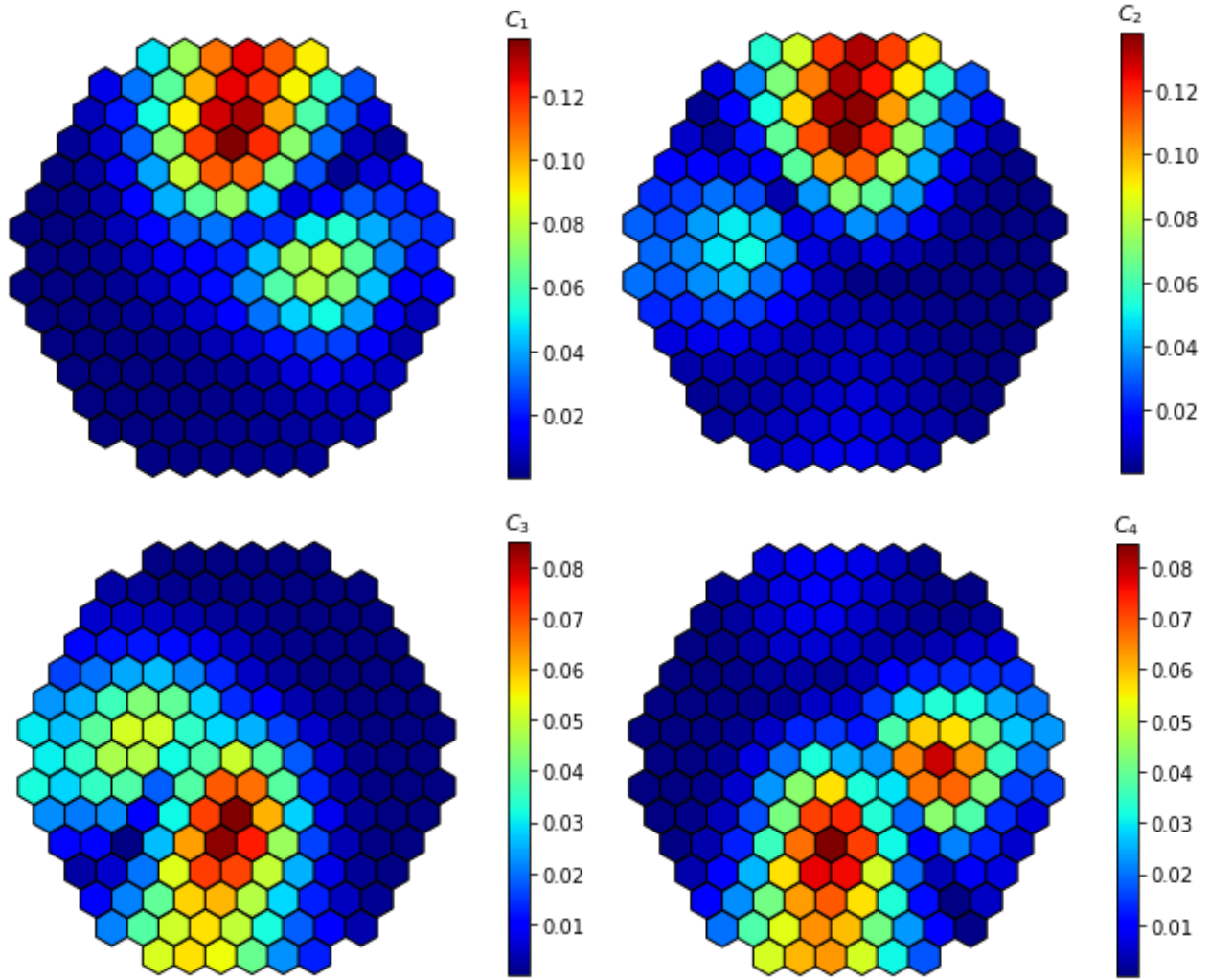


Figure 49 : Standard deviation of the mixing coefficients C_1 , C_2 , C_3 and C_4

b. FA temperature average

The mean value and standard deviation of the average temperature evaluated on each FA is given Figure 50.

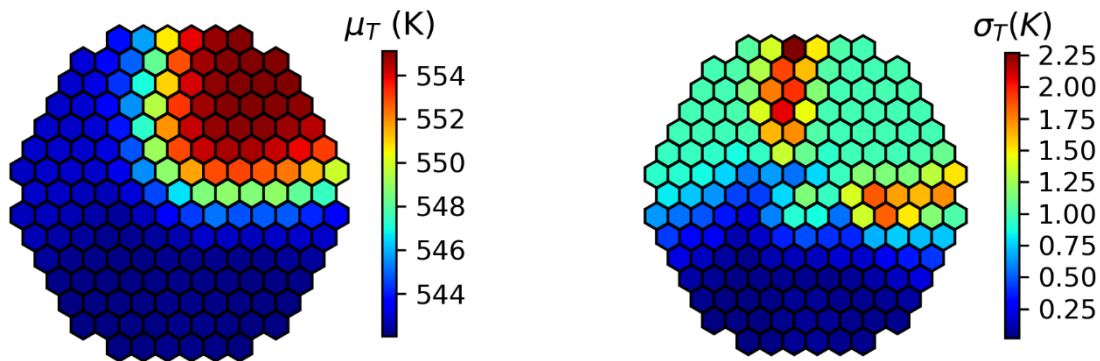


Figure 50 : Mean value and standard deviation of the FA temperature evaluated with GHM ensemble for CEA computations

The POD is applied to the 9 snapshots of the FA temperature. The RIC number is given as a function of the number of POD modes on Figure 51 while the four first modes are given Figure 52.

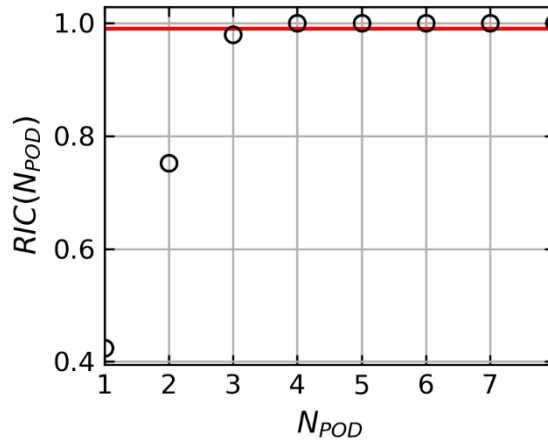


Figure 51 : RIC as a function of the number of modes for the POD applied to the snapshots of the different ensembles evaluated by CEA with GHM ensemble.

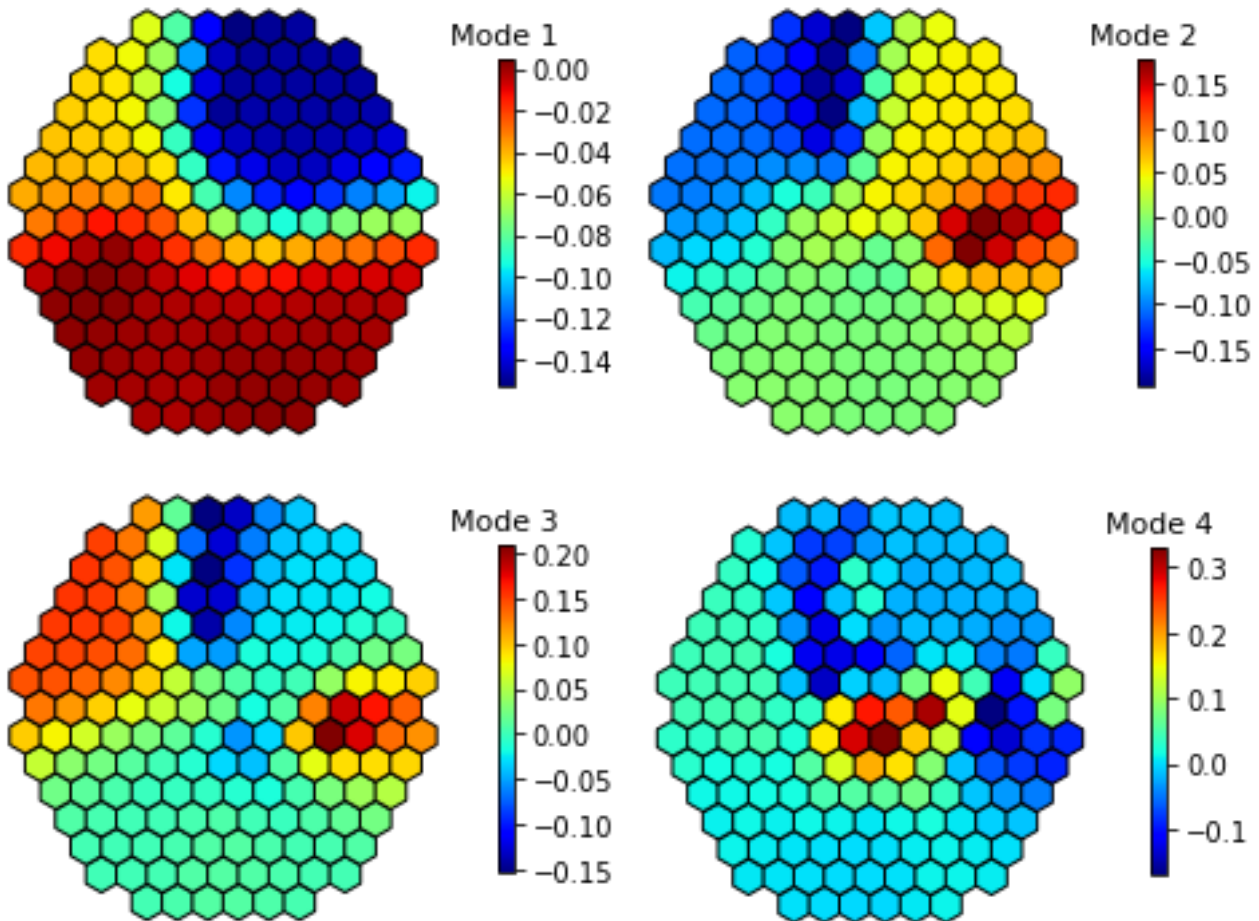


Figure 52 : 4 first modes calculated from the snapshots of ensemble Σ_{GHM} .

The sensitivity of this quantity to the inputs is similar to the other partners:

- The cold leg temperature 1 and 2 variations induce variations in the top side of the core with an amplitude of approximatively 1°C.
- Higher amplitudes are found at the junction between mixing zones 1 and 2. In this zone, the standard deviation reaches 2°C.
- The standard deviation on the lower side of the core is much lower with values around 0.25°C.
- In contrast to the other partners models, the lobes that were visible due to the core power variations are not seen for these computations which seems logical. In fact, for these calculations of CEA model, the power variations were not implemented.

c. Hot leg 1 temperature $T_{HL,1}$

The core power is not implemented in this calculation which induces much lower temperature than the other partners.

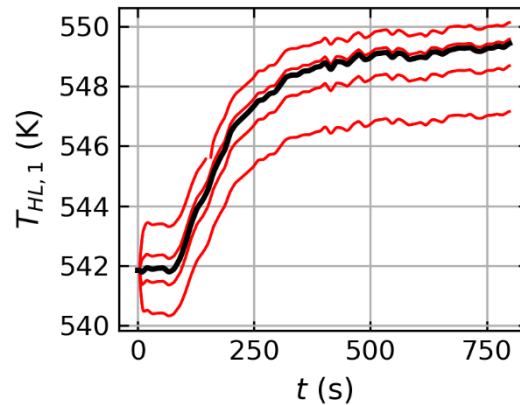


Figure 53: increase of temperature in hot leg 1 $T_{HL,1}$ for the different inputs scanned.

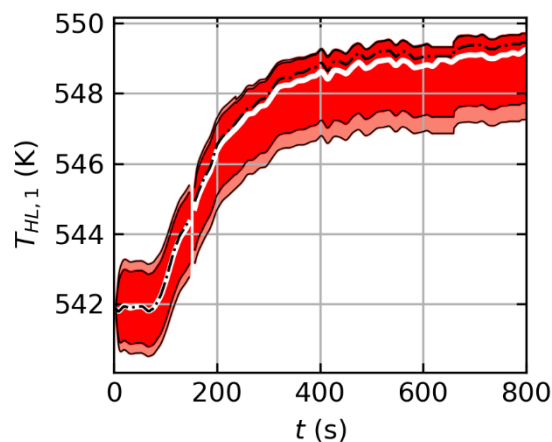


Figure 54: Time evolution of $T_{HL,1}$ – Mean value (dotted black), median value (solid white), $Q_{5\%}$, $Q_{95\%}$ (filled red), $Q_{2.5\%}$, $Q_{97.5\%}$ (filled salmon)